The Application of Particle Image Velocimetry in a Small Scale Wind Tunnel

by

Bryan Sperandei

A thesis
presented to the University of Waterloo
in fulfilment of the
thesis requirement for the degree of
Master of Applied Science
in
Mechanical Engineering

Waterloo, Ontario, November 2002

I hereby declare that I am the sole author of this thesis. This is a true copy of the thesis, including any required final revisions, as accepted by my examiners.

I understand that my thesis may be made electronically available to the public.

Acknowledgments

The amount of work that went into this thesis could not have been possible without the help and support of many.

I would like to thank Dr. David Johnson for creating this unique opportunity for me at the University of Waterloo. I am very thankful for his guidance and support over the past two years.

To my friends in Waterloo, John Costa, Paul Deslauriers, Teo Dabov and Rafal Smerd for their companionship during those late FSAE/thesis nights. To Ross Gilbert, who guided me through the whole thing and prevented me from losing what little remains of my sanity. Thanks to all of my boys back home, Laurence Borg, Frank Cardamone, Ryan Pinto, Chris Fernando, Germyn Caylao, Albert Patel, Joe Gignac, Ed Rigonan, Frank Bellomo, Massimo Taraborelli, Mike Pozzobon and more for always saving me a seat; my University cronies, Frank and Sandra Tomassini, Quinton McBlain, Jon Hook, Ivan Luke, and crew for throwing the meanest parties that I've ever experienced. A special thanks to Paola Milio for her friendship over the past two and a half years. To my close friend, Shervin Shaffie, I credit you with truly showing me the value of self-confidence.

To my parents, whose support has been neverending and unconditional, you have given me much of the motivation needed to complete this degree.

To my best friend in the world, my big brother, William: it is very easy for me to say that a brother better than you simply does not exist on this planet, as I've got the best one. You've always been there during my darkest times, and celebrated with me in the most joyous of times. You have opened my eyes and made me see just how much there is in this life.

This thesis is dedicated to Joe, Liviana, William, Norina, and Julien Sperandei who are the centre of my life.

Abstract

This study investigated the applicability of Particle Image Velocimetry (PIV) as a velocity measurement technique for use in wind tunnel flows. To carry out the investigation, a small scale wind tunnel was designed and built to be used specifically with PIV. The tunnel employed a novel contraction geometry which was compared to six other contraction designs using a computational fluid dynamics (CFD) software package. The wind tunnel configuration allowed for full optical access in the test section to allow for PIV measurements in three dimensions.

The calibration and characterization of the flow quality within the wind tunnel were performed using PIV. Velocity measurements were obtained in the empty test section to assess the degree of uniformity, alignment, and turbulence at various test speeds. The longitudinal velocities were found to deviate by an average of 1.8% along any given velocity profile. The flow was found to be well aligned with the test section walls, deviating by no more than $\pm 0.20^o$ in most cases. As well, the turbulence levels in the test section were found to be low, with average intensities of 2.0% and 0.5% in the longitudinal and transverse directions, respectively.

Following the characterization of the flow in the empty wind tunnel, a square cylinder was placed in the test section and PIV measurements were performed at a Reynolds number of 21400. Mean velocities and turbulence intensities measured around the square cylinder were found to compare well with previous works conducted at similar Reynolds numbers in water flows.

As a final validation of the wind tunnel/PIV system, measurements were made of the flow over a 1:18 scale Formula One racecar model at a free stream velocity of 40 m/s. The PIV system collected a large quantity of velocity information around the model, providing insight into the aerodynamic aspects of racecars such as downforce devices and vehicle draughting.

The experiments performed in this study led to the conclusion that PIV is indeed a measurement technique with high potential for use in small wind tunnels, providing more spatially resolved velocity data than any other known measurement technique. The advancement of digital camera technology will make PIV a more practical measurement technique for use in larger wind tunnels as well.

Contents

List of Tables

List of Figures

Chapter 1

Introduction

1.1 Wind Tunnels and Measurement Techniques

The wind tunnel has come to be recognized as a fundamental research and design tool in the field of aerodynamics since its conception in the early 1900s. The amount of information gained from wind tunnel experiments has always been limited by the nature of the measurement techniques employed. Flow visualization techniques such as string tufts, dye and smoke injection have been limited to strictly qualitative observations. Techniques such as pitot probes, hot-wire anemometry, and laser Doppler velocimetry (LDV) have only been capable of providing quantitative results in a very small area of the total flow field at any one time. The desire for a more complete characterization of a given flow field led to the development of a new measurement technique known as PIV.

1.2 Particle Image Velocimetry (PIV)

Particle Image Velocimetry (PIV) is a relatively new measurement technique capable of providing quantitative velocity information using the basic principle of flow visualization. With PIV, two pictures of a flow field are captured within a very short time. If points in the flow field can be

traced from the first picture to the second, its displacement can be recorded and then divided by the time separation, giving a velocity. The major advantage of PIV is the ability to quickly measure these velocities over a relatively large area in a non-intrusive manner.

1.3 Thesis Objectives

This study focused on the union of the two systems introduced above: the application of Particle Image Velocimetry in a purpose-built wind tunnel. While a small number of wind tunnel experiments have been conducted using PIV, it remains a largely unexplored measurement technique in wind tunnel flows. The wind tunnel in this study was designed and built to be used specifically with PIV, and its initial flow characterization and validation were performed using PIV.

In undertaking this project, four main objectives were formulated.

1. Wind Tunnel Contraction Design - The wind tunnel used for this study employed a novel contraction geometry which was designed and tested using a computational fluid dynamics (CFD) software package. The contraction is an important section of any wind tunnel, responsible for accelerating the air flow to test speeds. The first objective therefore was to determine the optimal contraction design through simulation, and to put the design into practice by incorporating it into the purpose-built tunnel.

2. Compatibility of the PIV Measurement Technique in the Wind Tunnel - Once fabricated, the wind tunnel was used in combination with the PIV measurement technique. The second objective of this study was to explore the compatibility of the two elements by performing PIV velocity measurements in the wind tunnel. The conclusions drawn here would indicate the feasibility of PIV as a reliable and user friendly measurement technique in the wind tunnel.

3. Performance of the Wind Tunnel/PIV Combination - Assuming PIV to be a feasible measurement technique in the tunnel, it would then be necessary to determine whether the

PIV/wind tunnel combination could provide accurate flow fields and velocity measurements. Therefore, the third objective involved the reproduction of a well-studied flow field for comparison and validation of the system used here.

4. Versatility of the Wind Tunnel/PIV Combination - The final objective in this study was to test the versatility of the wind tunnel/PIV system by performing measurements over a complex geometry. The degree of success realized in this experiment would determine the level of flexibilty of the wind tunnel/PIV combination when faced with more difficult flow conditions.

1.4 Thesis Outline

Chapter 2 discusses in detail the design of the small scale wind tunnel used in this study, including the CFD design study of the contraction section. The following chapter briefly reviews the fabrication of the wind tunnel, highlighting any unique manufacturing solutions specific to this study. Chapter 4 describes PIV in more detail, while reviewing relevant literature on the topic of PIV and wind tunnels. As well, the PIV system and components used for all the experiments in this study are described. In Chapter 5, the flow characterization of the wind tunnel is documented. This includes the description of each experiment, its setup, and results. Chapter 6 presents the measurements of the flow over a square cylinder for comparison with previous experimental work. In Chapter 7, flow measurements were performed over the aero body of an open wheeled racecar. Finally, a set of conclusions and recommendations are presented in Chapter 8.

Chapter 2

Wind Tunnel Design

2.1 Introduction

In order to design a useful wind tunnel, there are many design criteria which must be followed. The tunnel should be properly sized to accommodate the types of models to be tested. In addition, the wind tunnel must also provide a controlled flow of high uniformity and low turbulence to produce meaningful aerodynamic measurements. When designed properly, a wind tunnel will achieve these goals in an efficient manner with minimal energy losses and acoustic noise.

This chapter describes in detail the design procedure followed to create the wind tunnel for this study. The final design is presented below and briefly described in order to provide groundwork for understanding each subsequent design section.

The wind tunnel used for this study was of the closed circuit type, utilizing air as its working fluid, and attaining a maximum test section speed of 45 m/s. Beginning with the fan (Figure 2.1), the air flows counter-clockwise into a circular to square transition (transition 2) before entering corners 1 and 2. In these corners, the flow is turned 180° to enter the settling chamber. Here, the flow is straightened and conditioned with the use of honeycomb and screen sections. After the settling chamber, the flow is accelerated through the contraction in order to reach the

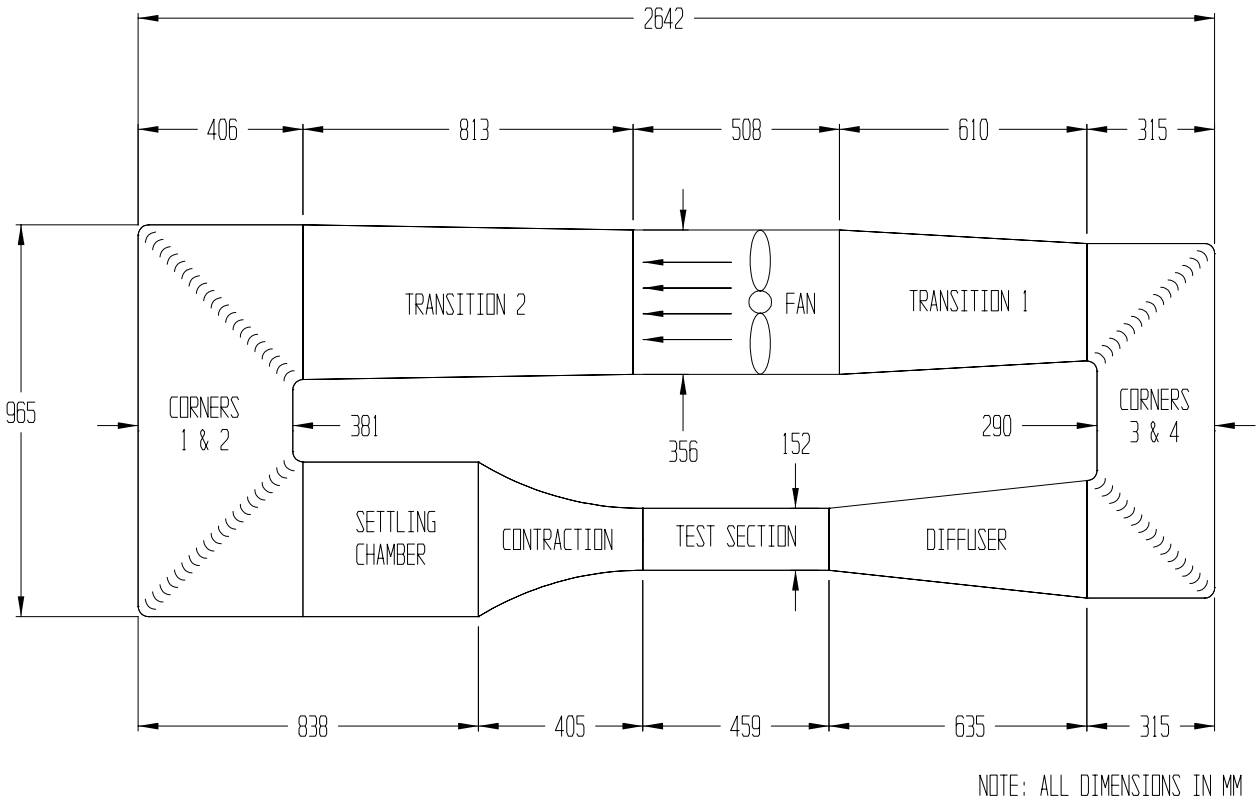

Figure 2.1: Wind tunnel components and dimensions (plan view)

desired speed entering the test section. In the test section, the flow is at its highest speed, and all aerodynamic measurements are performed here. The wind speed decreases in the diffuser before being redirected once again by corners 3 and 4. Finally, transition 1 progresses from a square to circular cross section in order to mate with the fan inlet, completing the circuit.

2.2 Types of Wind Tunnels

Reviews of wind tunnel designs and basic information can be found in [1, 2, 3]. A wide range of wind tunnels are used by researchers, extending from meteorological applications (environmental tunnels), aerospace (free-flight tunnels, spin tunnels, stability tunnels), to automotive applications. Despite this vast array of applications, almost all wind tunnels can be classified into one of two categories: open and closed circuit.

The first category is the open circuit wind tunnel. This is the simplest form of a wind tunnel, as the air is drawn by a fan through a contraction, test section, and diffuser all in a straight line. Conversely, the second category is the closed circuit wind tunnel. In this case, the air re-circulates through a closed loop system and therefore requires many changes in direction. Clearly, an open circuit tunnel is cheaper to manufacture than a closed circuit tunnel due to the presence of fewer parts. However, the advantages of a closed circuit tunnel are significant. The main advantage is the ability to control the flow quality in a closed circuit by corner turning vanes and screens. As well, a closed circuit tunnel requires less energy to operate than a similarly-sized, open circuit tunnel and creates less operating noise.

For this particular study, a closed circuit design was selected. Apart from superior flow quality control, the main factor in selecting a closed circuit arose from a requirement specific to PIV. Since this measurement technique requires the injection of seeding particles into the flow, it is desirable to contain these particles within an enclosed environment. It would be extremely difficult and wasteful to seed an open circuit tunnel as the seeding particles are continuously released to the atmosphere and therefore irrecoverable. Once the volume within a closed circuit tunnel is fully seeded, it will re-circulate without the need for continuous replenishment.

Once the decision for either an open or closed circuit has been made, the process of wind tunnel design begins with the test section [1].

2.3 Test Section Design

Before determining its shape and size, it must be decided whether the test section will be open (to the atmosphere) or closed. Although many closed circuit wind tunnels can be modified to operate with either configuration, an open test section may encounter large flow fluctuations, requiring extensive troubleshooting. For this reason, as well as the issue of seeding mentioned in the previous section, a closed test section was selected for the wind tunnel in this study.

The most common test section shape is rectangular or square in cross section. A square test section was chosen here for several reasons:

1. Ease of fabrication as opposed to a circular or complex curve cross section;
2. Mounting and changing of models will be less complicated on a flat surface; and,
3. PIV requires optical access within the test section, and there is no distortion from a flat window. Collecting images through a curved window would give skewed images, requiring intensive post-processing.

The size of the test section was the next important parameter, as it dictated the overall size of the wind tunnel. Three main design criteria were fulfilled with the test section determination. Space limitations within the facility have always been a major factor in wind tunnel size, as it is generally desirable to have as large a test section as possible. In the Turbulent Flow Laboratory at the University of Waterloo, the largest area of available floor space amounted to approximately $4m$ x $2.5m$. Based on preliminary design iterations, and the need for extra space around the tunnel for PIV hardware *etc.* it was determined that the maximum feasible test section size should be no more than $152.4mm$ x $152.4mm$ (approximately 6 in. x 6 in.).

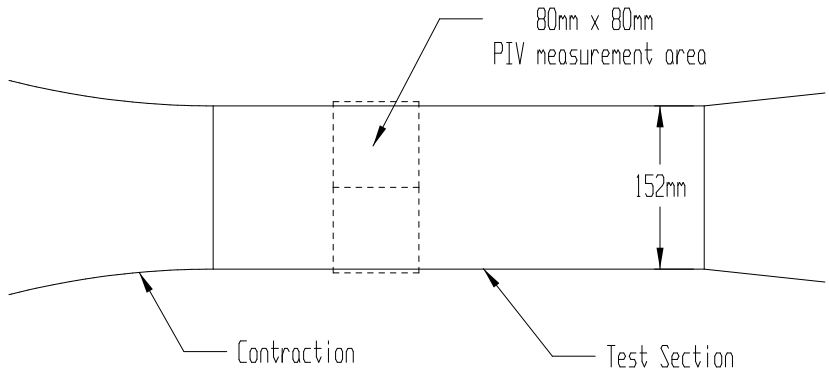

Figure 2.2: Selecting a test section height suitable for two PIV measurement windows

Since the distinguishing feature of this particular wind tunnel is its compatibility with a PIV system, it is only natural that the test section should be sized to accommodate a typical PIV measurement area. It was decided from the onset that in order to keep the quantity of PIV measurements to a reasonable number, the entire width or height of the test section should be viewed fully in no more than two measurement areas. The term *measurement area* as shown in Figure 2.2 refers to the two dimensional area within which velocities can be measured by the PIV system in one experimental setup. It is one of the requirements for accurate PIV measurements that the seeding particles captured in each image fall within a certain size. Therefore, based on particles having an image size of $0.25mm$, a reasonable viewing window for PIV was found to be approximately $80mm$ x $80mm$ [4]. With an $80mm$ square viewing area, a test section with sides of $160mm$ or less could be covered in two PIV windows.

As a third design criteria for its sizing, it was decided that the test section should be able to accommodate a 1:18 scale automobile. According to Pope *et al.* [2], a general rule of thumb is to keep the model span below 0.8 times the test section width. With a $152.4mm$ square test section, the largest model span would be limited to $122mm$. At a scale of 1:18, this translated to a maximum full size vehicle track width of $2.19m$, which covers the range of almost all automobiles and racecars. For these reasons, a final test section was chosen to be $152.4mm$ x $152.4mm$ in cross section. Its length ($405mm$) was chosen to be approximately 3 times the test section height. This would allow for multiple vehicle models to be tested simultaneously (*i.e.* one vehicle model

with another directly behind it) for aerodynamic slipstream studies.

From the test section, it is accepted practice to move downstream along the wind tunnel when designing each component. This led to the diffuser section, responsible for decelerating the flow and recovering pressure before corners 3 and 4.

2.4 Diffuser Design

In designing the diffuser, which acts as a diverging duct, it was necessary to follow guidelines pertaining to the cone angle and area ratio to limit the amount of flow separation exiting the test section. The cone angle is the total angle formed by the walls of a circular diverging cone. In the case of a rectangular duct, as was the case in this study, an equivalent cone angle can be used. This is calculated by using an imaginary conical diffuser with the same inlet and outlet areas and length as the square duct in question. The area ratio, AR, is defined universally for both straight-walled diffusers and contractions as the ratio of the largest cross sectional area to the smallest. In the case of a diffuser, AR is the outlet area, b^2 divided by the inlet area, a^2 in Figure 2.3. Diffusers with equivalent cone angles greater than 3.5^o have been shown to experience flow separation and non-uniform velocity profiles without the addition of screens or other boundary layer control devices [5, 6, 7, 8]. In addition, the area ratio should be approximately 2 to 3, while its overall length should be at least 3 to 4 times the test section length. For an area ratio of 3, a diffuser of at least $2.06m$ in length would be needed. Given the space restrictions mentioned in Section 2.3, the entire wind tunnel length was to be limited to well below $3m$. Therefore, a $2m$ diffuser and $0.5m$ test section would leave little room for the rest of the necessary components.

An alternative was to use a wide angle diffuser which is defined as a diffuser in which the cross-sectional area increases so rapidly that separation can be avoided only by using boundary layer control [9]. The use of a wide angle diffuser would allow for a much shorter overall tunnel length, one of the main design parameters as outlined in Section 2.3.

The most common method of addressing separation in a wide angle diffuser is to install one or more wire mesh screens. A properly selected wire mesh screen will reduce the thickness of the

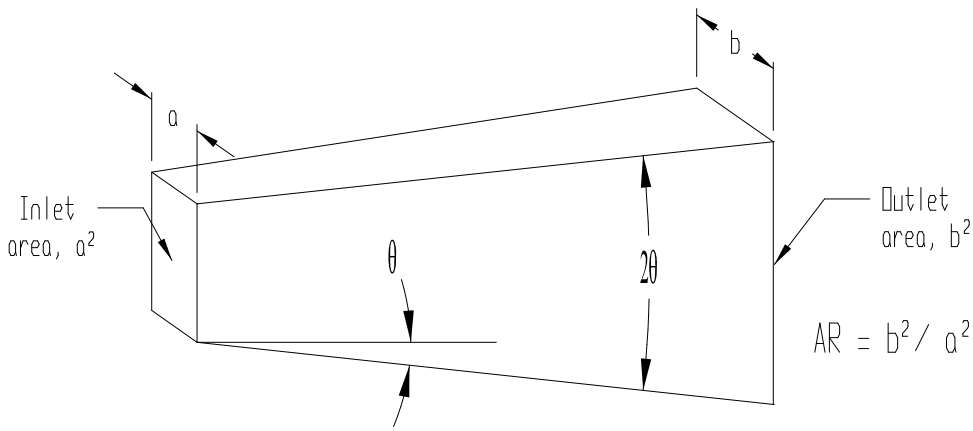

Figure 2.3: Definitions of the area ratio, AR, and the total diffuser angle, 2θ in a diffuser of square cross section

boundary layer, lower the turbulence intensity level, and smooth out the overall velocity profile [9]. Mehta [9] analyzed published data from 56 wind tunnels operating with wide angle diffusers. From each tunnel, he compiled the following diffuser characteristics:

1. The area ratio, AR, of the diffuser (Figure 2.3);
2. Total diffuser angle, 2θ (Figure 2.3);
3. The number of screens used in the diffuser; and,
4. Whether the diffuser performed successfully.

Based on the data from these wind tunnels, Mehta [9] plotted the area ratio versus the total diffuser angle, with lines indicating the number of screens used. These results were later interpreted by Pope *et al.* [2], and presented in similar form, using the screen lines as design boundaries. After several iterations, a short, wide angle diffuser was designed, having a length of only $635mm$ while expanding from $152.4mm$ x $152.4mm$ (test section) to $290mm$ x $290mm$ (outlet). This resulted in an area ratio of 3.62 and a total diffuser angle of 12.2^o (see Figure 2.6). From Figure 2.5, this design point was plotted and found to lie to the left of the zero screen line, indicating

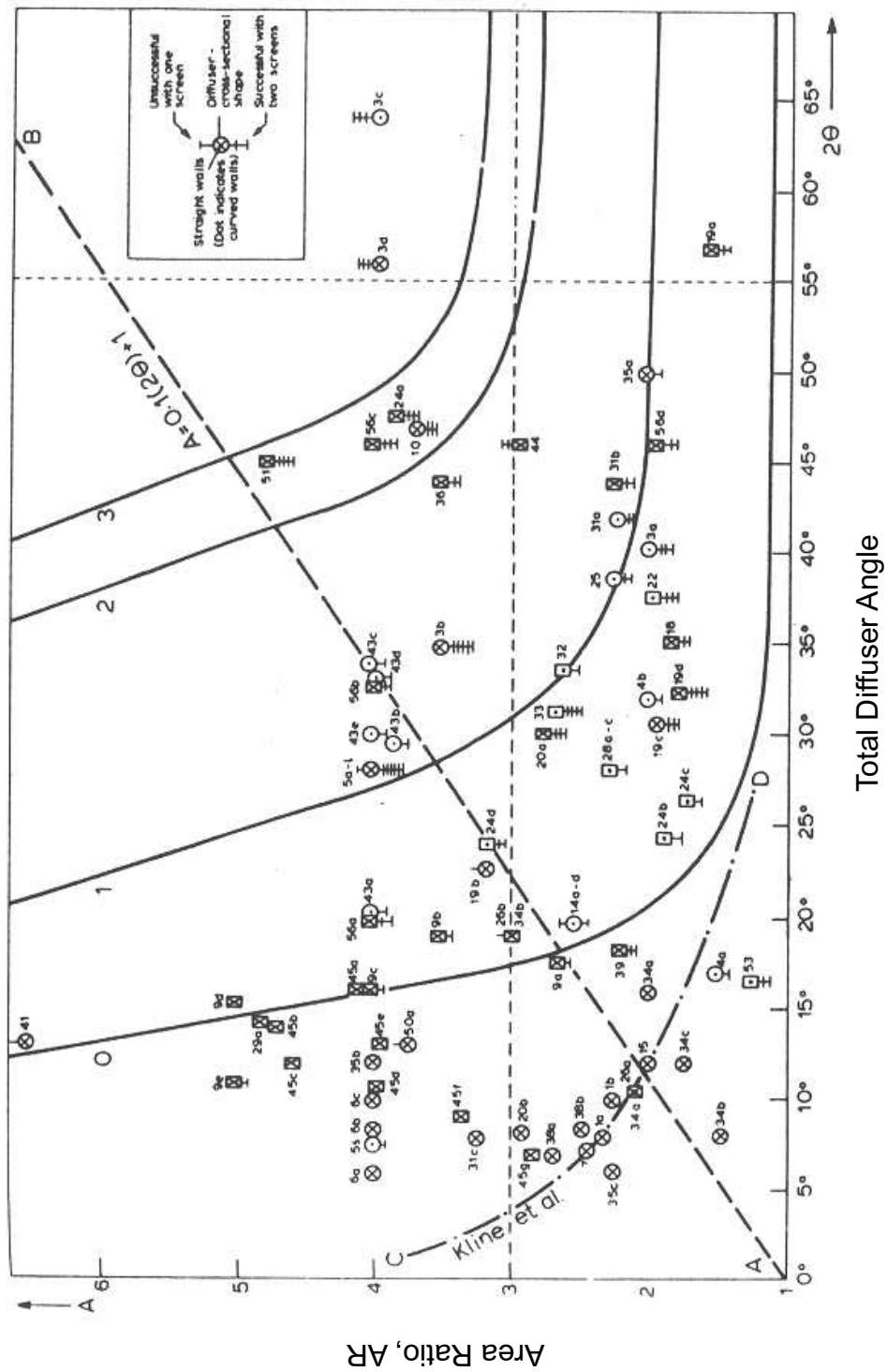

Figure 2.4: Area ratio versus total diffuser angle for various wind tunnel diffusers [9]

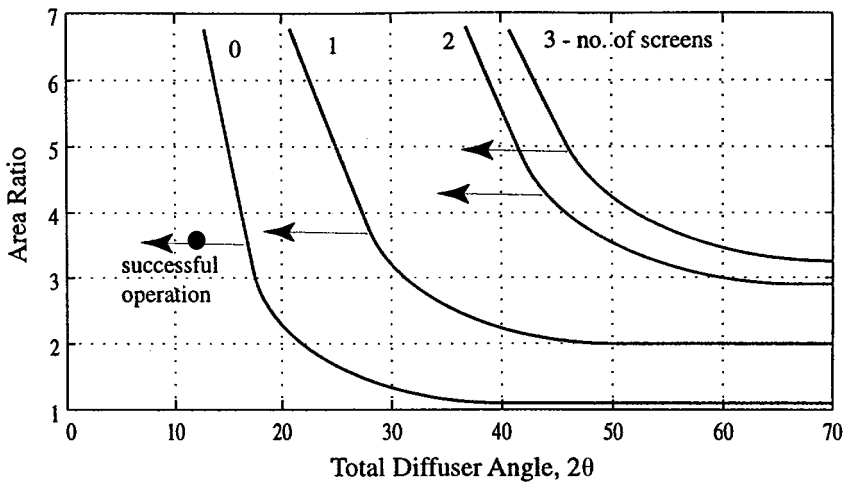

Figure 2.5: Diffuser design chart [2]: •, diffuser in this study

that this particular wide angle diffuser should operate successfully without the use of any screens.

2.5 Corner Design

The four corners of a conventional closed circuit wind tunnel have the task of redirecting the flow by 90° around each corner with minimal losses and flow disturbance. They typically combine to account for approximately 60% of the total losses within the tunnel [2]. It is for this reason that good corner design is essential to the operation of the tunnel. The most critical feature of the corner is the method by which the flow is redirected. An empty 90° corner has been shown to generate a large eddy on its inside wall immediately downstream of the corner [10]. To reduce and/or eliminate this eddy, the use of turning vanes is necessary. The experimental work of Klein *et al.* [10] was the first investigation of the use of various turning vane shapes in a 90° corner. Six different turning vane shapes were utilized and compared, ranging from a square vane to a quarter circular arc, to thick, airfoil-like profiles (Figure 2.7). They determined that the vane shape was not really a very critical factor, in that any reasonably shaped vane, such as shape 3, 4,

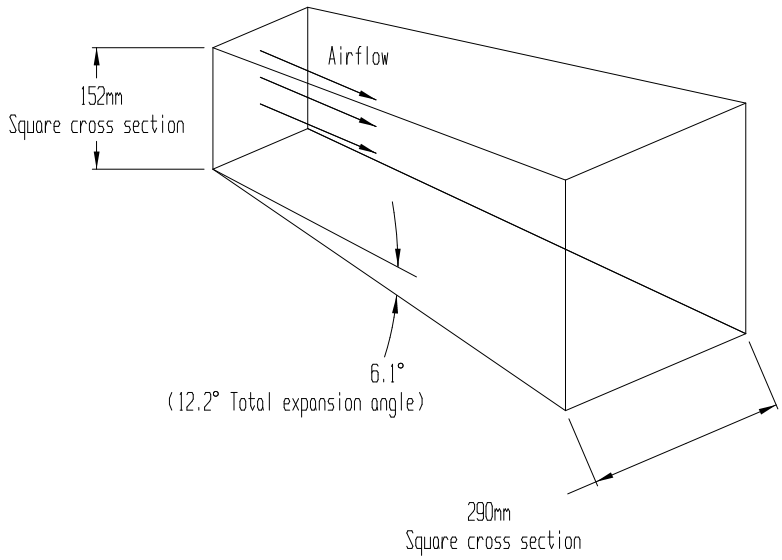

Figure 2.6: CAD model of wind tunnel diffuser

5, or 6, would give good characteristics to the corner [10]. In light of these results, it was decided to utilize quarter circular arc turning vanes for simplicity, ease of manufacture, and effectiveness in turning the flow. The next step in the design of the turning vanes was the determination of the chord length and spacing between each vane.

Due to the availability of a 1 in. radius forming tool, a radius of $25.4mm$ (1 in.) was chosen for all turning vanes. The experiments of Klein *et al.* [10] as well as Lindgren *et al.* [11] compared the pressure drop and pressure loss coefficient, respectively, of corner turning vanes at different pitch values, e, defined as the ratio between the vane spacing and the vane chord length (Figure 2.8). Both sets of authors, although nearly 70 years apart, agreed fairly closely that the minimum pressure loss occurred at a pitch of approximately 0.33 to 0.35 (Figures 2.9 and 2.10). The upper value was chosen, and with a chord value of approximately $36mm$, a turning vane spacing of $12.7mm$ (0.5 in.) was calculated. This resulted in a total of 148 turning vanes (42 in each of corners 1 and 2, and 32 in each of corners 3 and 4).

Moving downstream from corners 3 and 4 (Figure 2.1), transition 1 was designed as a rectangular-

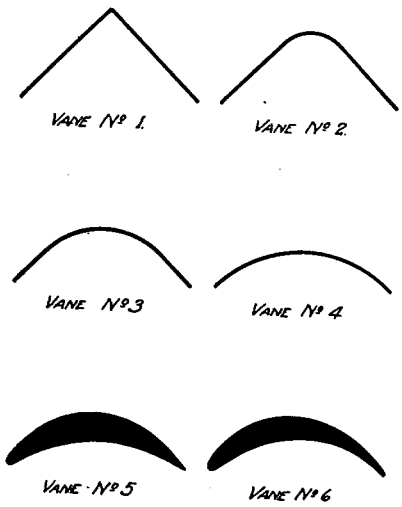

Figure 2.7: Six different turning vane profiles tested by Klein *et al.* [10]

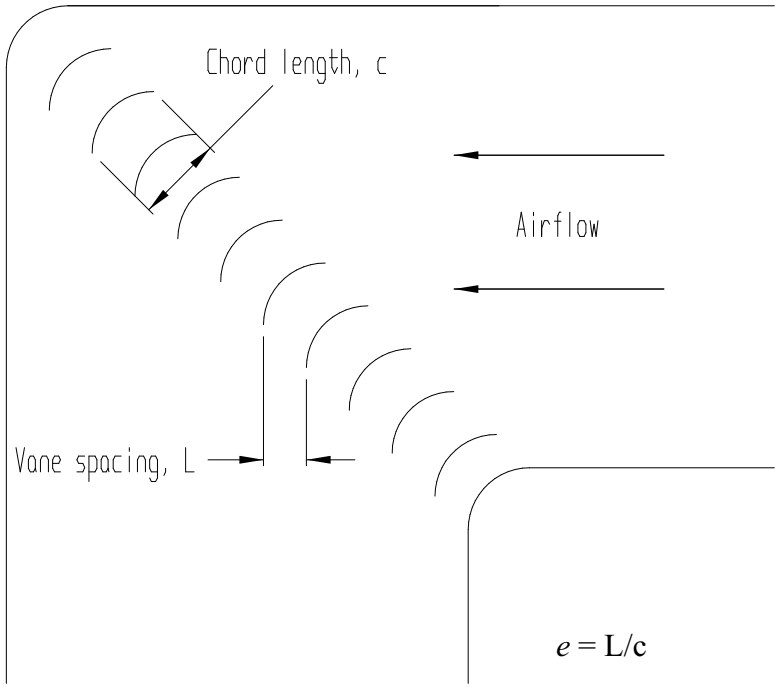

Figure 2.8: Turning vane chord and pitch length definitions

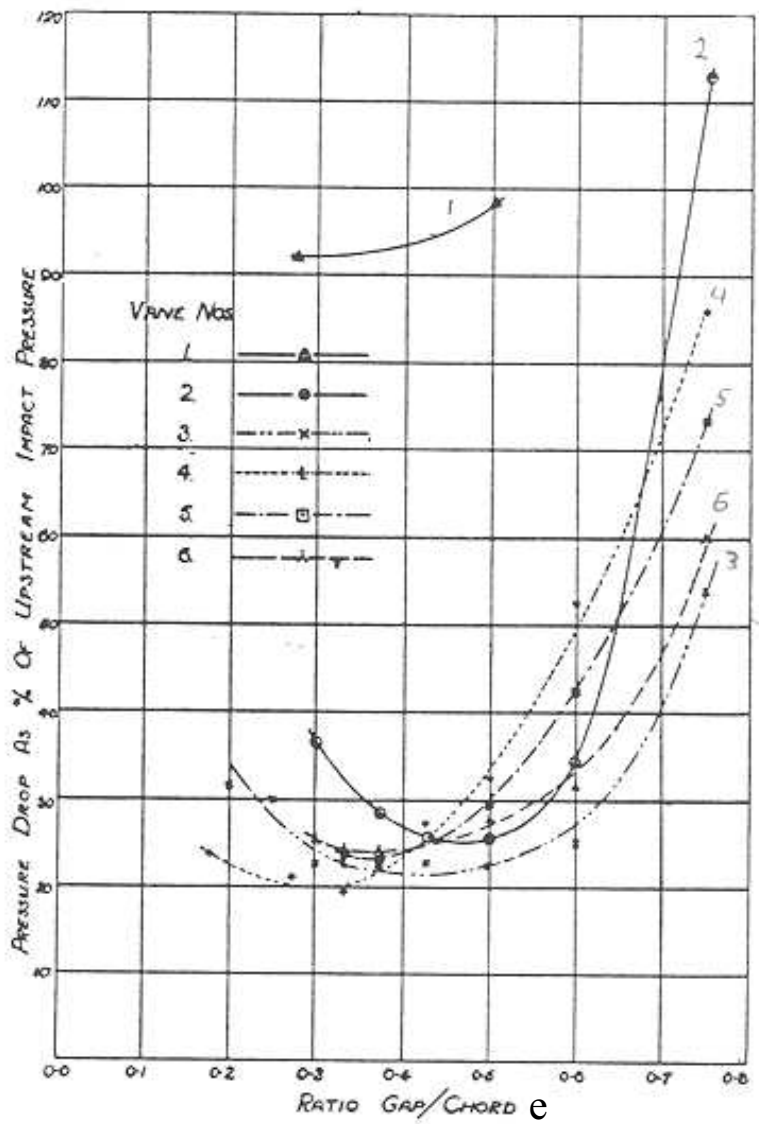

Figure 2.9: Turning vane pressure losses as a function of pitch, e, for the vane profile designs shown in Figure 2.7 [10]

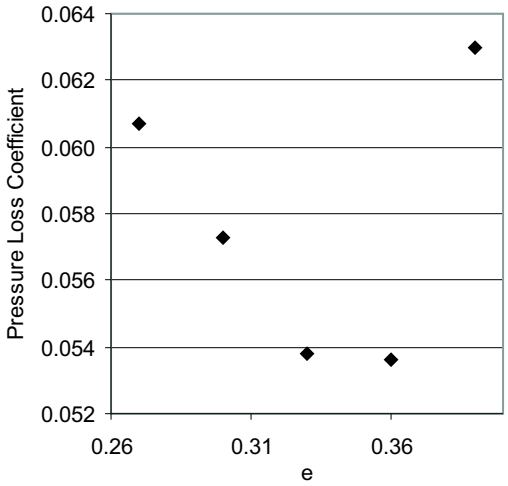

Figure 2.10: Turning vane pressure losses as a function of pitch, e [11]

to-circular duct, expanding in cross sectional size from a $290mm$ x $290mm$ square inlet to a $356mm$ diameter circular outlet to mate with the fan section. Although the fan diameter was chosen early on, the detailed selection of the fan was left until the rest of the wind tunnel components were designed, since an estimation of the total circuit losses was needed in order to determine the required fan power. From the fan outlet ($356mm$ diameter), transition 2 converted the circular cross section back to a square cross section measuring $381mm$ x $381mm$. Downstream of corner 2, a settling chamber was incorporated as a constant cross section ($381mm$ x $381mm$) duct. This served as an area for including flow straighteners or screens to minimize the velocity variations before entering the contraction section. The honeycomb flow straighteners and screens will be described in Section 2.7.

2.6 Contraction Design

The contraction section is one of the most critical components in the wind tunnel. It must accelerate the flow with minimum separation and boundary layer growth, while reducing turbulence

and non-uniformity of its exit velocity. This must be achieved in as short a distance as possible to allow for a longer test section.

This section outlines the three-dimensional design study performed to determine the optimum contraction shape for a set area ratio and contraction length.

2.6.1 Literature Review - Contraction

Based upon numerous previous studies on the design of wind tunnel contractions, Morel [12] established a design procedure that has come to be widely accepted. He carried out an inviscid flow analysis of the maximum wall pressure coefficients at the inlet and exit of a contraction. For the analysis, Morel [12] assumed a family of wall shapes made up of two blended cubic arcs, essentially a one-parameter wall definition. The work of Mikhail [13] involved an inviscid flow analysis on axisymmetric contraction shapes made up of two arcs as well. The location of the point of inflection between the two arcs was varied as well as the overall contraction length. Mikhail [13] found that by optimizing duct wall curvature distribution, it was possible to reduce contraction length so that a contraction with an 8:1 area ratio can be as short as one inlet radius. The area ratio, AR, of a contraction section was defined as the ratio of the inlet area to the outlet area. Downie *et al.* [14] compared results from a finite difference numerical method with experimental results of contractions with rectangular cross-section. They found that pairs of matched elliptical arcs proved to be a simple way of achieving satisfactory profiles. Tulapurkara and Bhalla [15] used Morel's contraction design method [12] to fabricate and test two contractions with area ratios of 12 and 3.464. They found that the measured values of boundary layer thickness and velocity non-uniformity were smaller than the values predicted in Morel's [12] work. Su [16] performed a numerical analysis of three-dimensional contractions with a one-parameter wall definition (two blended arcs). Fang [17] extended the work of Morel [12] to three-dimensional cases and proposed a five step design method based on avoiding separation for a given level of exit flow quality. Callan and Marusic [18] performed an experimental study of the flow quality in four contractions designed using Morel's [12] and Su's [16] one-parameter wall definition. Chmielewski [19] used an inviscid flow analysis but included boundary-layer considerations in his analysis of axisymmetric contractions designed with two blended arcs. Batill *et al.* [20] published a numerical study of

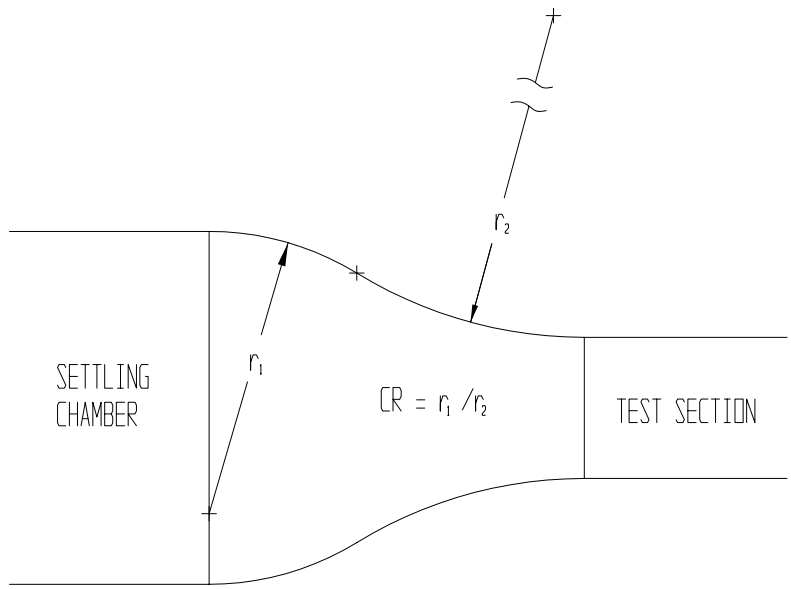

Figure 2.11: Definition of the curvature ratio, CR

three-dimensional wind tunnel contractions, again defined with a single parameter, matched cubic profile. It was evident in the publications outlined above that most of the work on contraction design followed Morel's [12] initial assumption of a two-arc wall definition.

2.6.2 Design Study - Contraction

At the onset of this design study, two geometry parameters were set based on the overall dimensions of the wind tunnel. The area ratio, AR, was set at 6.25 based on the already chosen test section and settling chamber dimensions. The length of the contraction was chosen as $405mm$ ($\approx$16 in.), only slightly longer than its inlet dimension, based upon Mikhail [13] who stated that a well designed contraction section could be as short as one inlet dimension. With these two parameters fixed, seven contraction designs were considered, differing only in wall curvature.

The wall shape was defined by the blending of two circular arcs. The various shapes could be differentiated with one parameter, the curvature ratio, (CR), defined as the ratio of the inlet side

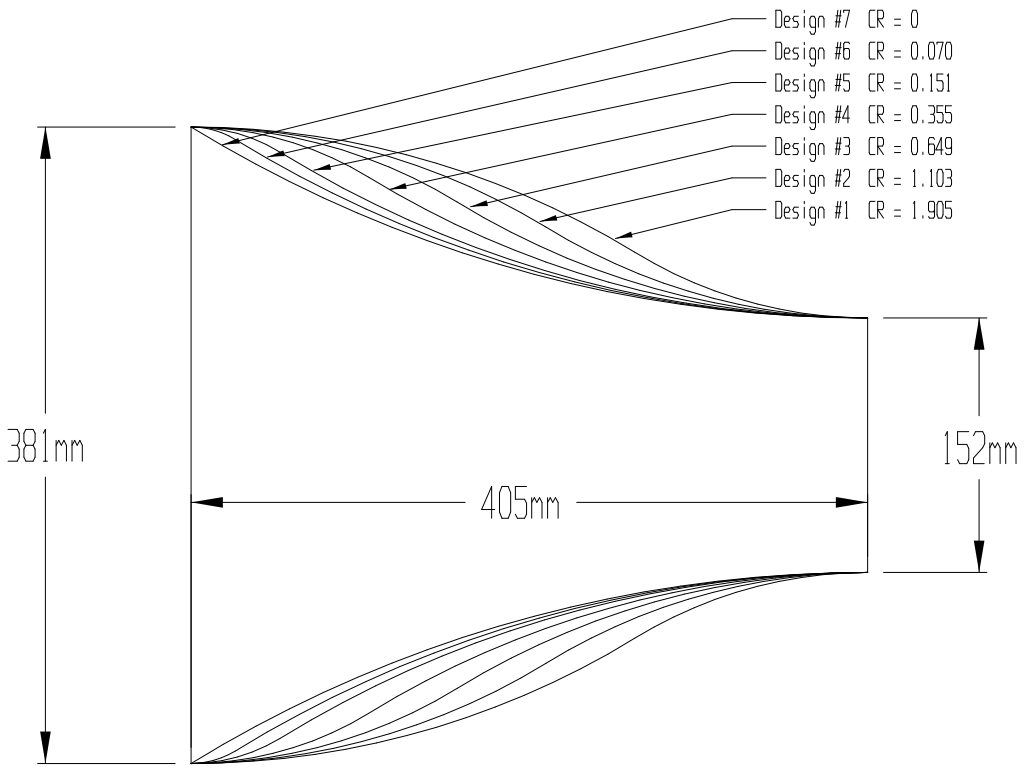

Figure 2.12: Seven different contraction shapes used in study (2-D view)

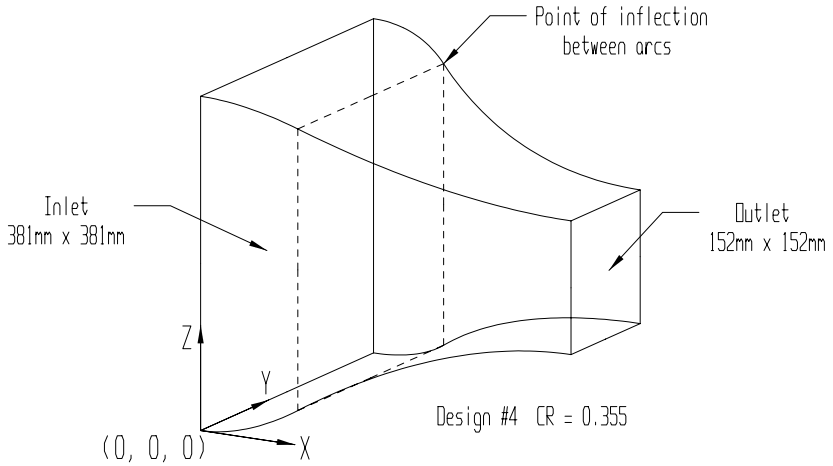

Figure 2.13: CAD model of contraction design #4

radius (r_1) to the outlet side radius (r_2) (Figure 2.11). Figure 2.12 shows the seven different shapes, in the range of $0 \leq \text{CR} \leq 1.905$, superimposed over the common inlet, outlet, and length. Design #7 was included as a novel geometry which eliminated completely the inlet side arc and utilized only one circular arc. These seven designs were then modeled using CFX-TASCflow (AEA Technology, Waterloo, ON), a computational fluid dynamics (CFD) software package available at the University of Waterloo.

Modeling and Meshing

The three-dimensional contraction models were generated and meshed using CFX-Build 4.3 (AEA Technology, Waterloo, ON), and all simulations were performed using CFX-TASCflow. Figure 2.13 shows the solid CAD model of one of the contraction designs (design #4). The existence of two symmetry planes along the contraction centreline was assumed, and the computational domain therefore utilized only one-quarter of the full geometry. The origin of each model was placed in the lower left corner of the inlet plane (Figure 2.13)

To ensure a fully-developed velocity profile entering the contraction, a long duct was placed upstream of the contraction inlet. The downstream test section velocity for this simulation was

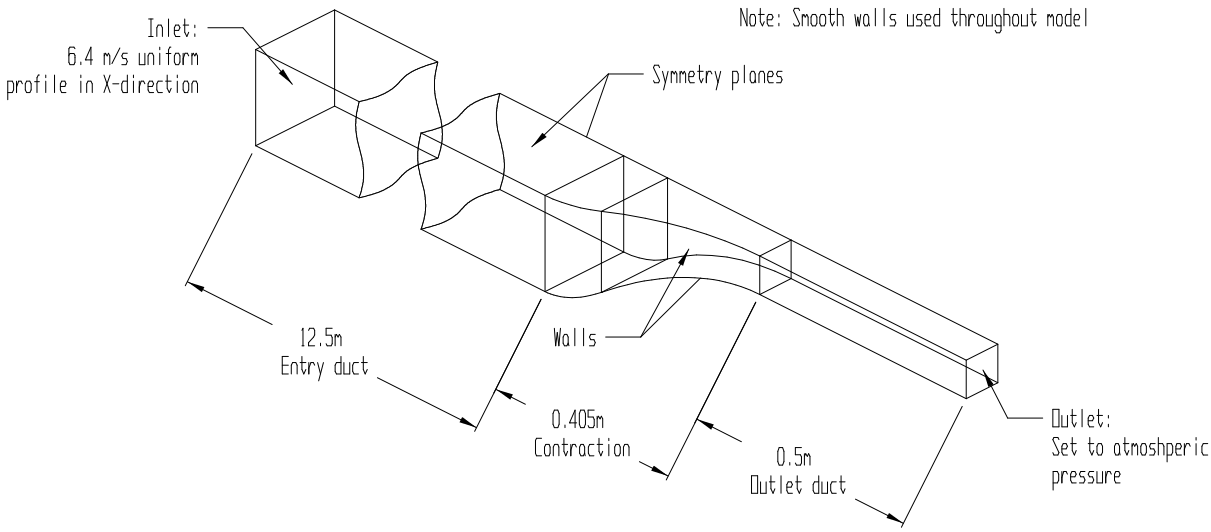

Figure 2.14: CFD model used in CFX TASCflow (plan view)

chosen as 40 m/s, and with an area ratio of 6.25, this translated into an upstream flow velocity of 6.4 m/s. To determine the required length of the upstream duct for fully-developed flow, the Reynolds number was calculated as:

$$Re = \frac{\rho V D_h}{\mu} \tag{2.1}$$

where, D_h is the hydraulic diameter defined as 4 times the cross sectional area, A, divided by the wetted perimeter, P.

$$D_h = \frac{4A}{P} \tag{2.2}$$

The working fluid was air at 25°C, ($\rho = 1.184 kg/m^3$, $\mu = 1.85 \times 10^{-5} Ns/m^2$ [21]) giving a Reynolds number of 156058. The required turbulent entry length could then be calculated from Munson *et al.* [21]:

$$\frac{l_e}{D_h} = 4.4(Re)^{1/6} \tag{2.3}$$

The entry length for the numerical model, l_e, was found to be $1230mm$ and hence a hypothetical $12.5m$ long duct was placed ahead of the contraction. To simulate the test section, a $0.5m$ long duct was placed downstream of the contraction.

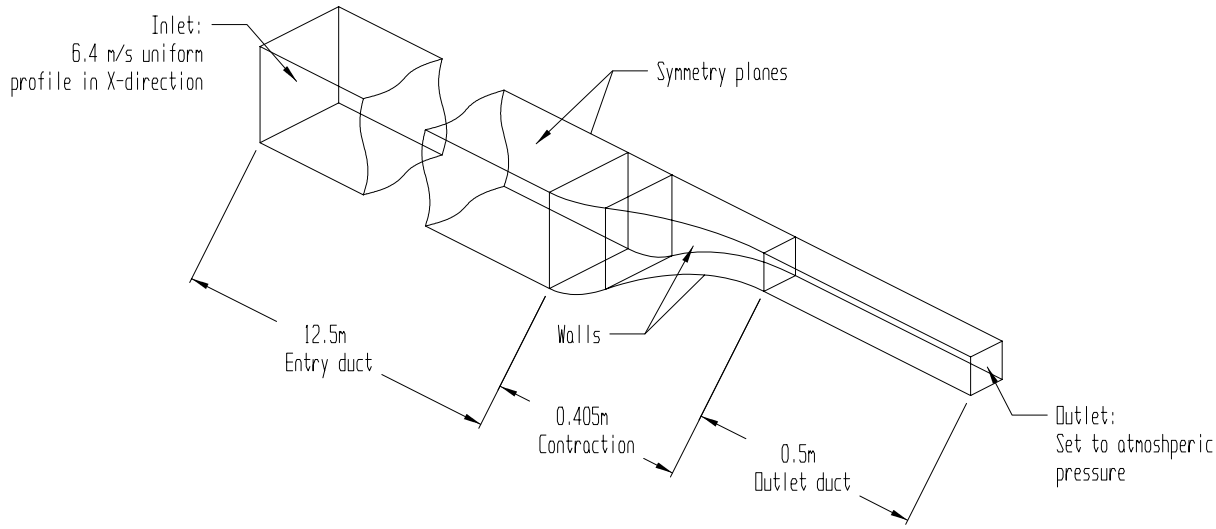

Figure 2.15: Boundary conditions used in CFX TASCflow

In order to minimize the number of grid elements in the CFX model, a coarse mesh was used in the upstream and downstream sections of the model (15 and 10 mesh seeds in the X-direction, respectively). For the contraction, a total of 60 X-direction mesh seeds were allocated. These 60 seeds were distributed differently for each design so as to keep the overall spacing uniform. A one-way bias was used when meshing in the Y and Z directions, with smaller elements placed near the wall. The bias was chosen such that the element nearest the wall was 1/10 the size of the element nearest the model centreline (Figure 2.14).

The boundary conditions chosen are shown in Figure 2.15. A uniform flow in the X-direction of 6.4 m/s was placed at the inlet plane. The outlet plane was set to atmospheric pressure (simulating an open-ended duct) and maintained that pressure throughout the entire simulation. Smooth walls were chosen for all models, and an initial time step of 2.11s was used. Table 2.1 shows the number of iterations required for each model to converge upon a solution.

All seven simulations were solved using the k-ϵ turbulence model with an upwind difference scheme, and the simulations were run until the maximum normalized residual was less than 1×10^{-3}. Further details about the TASCflow code can be found in [22] and [23].

Design#	CR	# elements	# iterations for convergence
1	1.905	14,701	32
2	1.103	14,701	31
3	0.649	14,701	28
4	0.356	14,701	25
5	0.151	14,701	50
6	0.070	14,701	35
7	0	13,801	50

Table 2.1: Number of iterations required for each contraction model to converge

As a check of the modelling accuracy, the locations of the first 10 nodes from the wall were verifed in terms of their locations relative to the wall boundary layer. The main objective was to ensure that at least one node was located within the boundary layer to allow for its proper modelling. To accomplish this, the simulation results were needed in order to calculate the following turbulence properties. The shear stress at the wall, τ_w was calculated using [24]:

$$\tau_w = \mu \frac{du}{dy} \tag{2.4}$$

and found to be 0.52 N/m^2 just downstream of the contraction exit, in the outlet duct. In Eq. 2.4, μ is the dynamic viscosity of air, and du/dy is the rate of change of the X-direction velocity (U) with respect to Y. From this value, the wall friction velocity [24], $\nu*$ was calculated as:

$$\nu* = \sqrt{\frac{\tau_w}{\rho}} \tag{2.5}$$

and found to be 0.66 m/s. With these two values, the Y-locations of the first 10 nodes were converted into "universal" coordinates [24]:

$$y^+ = \frac{y\nu*}{\nu} \tag{2.6}$$

where ν is the kinematic viscosity in m^2/s^2. Table 2.2 shows the y^+ locations of the first 10 nodes. The rightmost column shows where the node was located relative to the various regions within the turbulent boundary layer [24]. Documentation for CFX-TASCflow [23] suggests that for turbulent flows, the node nearest the wall should be in the range of $20 < y^+ < 100$. The mesh used in this study satisfied this requirement, with the first node being located at $y^+ = 27.09$ (see

Node	Node Location (distance from wall) [mm]	y+	Region
0	0	0	Wall
1	0.64	27.09	Overlap region
2	1.33	56.38	Overlap region
3	2.09	88.11	Overlap region
4	2.90	122.51	Outer region
5	3.78	159.70	Outer region
6	4.73	199.98	Outer region
7	5.76	243.59	Outer region
8	6.88	290.80	Outside boundary layer
9	8.09	341.93	Outside boundary layer
10	9.40	397.25	Outside boundary layer

Table 2.2: "Universal" [24] locations of the first 10 nodes used for the CFD modelling of the contraction

Table 2.2). With the close mesh spacing near the wall, the first 7 nodes were found to be located within the wall boundary layer.

Results

Figures 2.16 and 2.17 are vector maps of the flow velocities along one plane of symmetry in each of the seven contraction designs. In all cases, a uniform velocity profile of 6.4 m/s was applied to the inlet, and was accelerated to nearly 40 m/s at the exit of the contraction. From Figures 2.16 and 2.17, the general path of the bulk flow observed in each design did not reveal a distinct advantage in any particular one of them. In order to quantitatively compare each contraction, a set of performance parameters were defined to assess the results of the CFD simulation:

1. Average velocity exiting the contraction - this would show which design most successfully accelerated the incoming flow;

2. Average turbulent kinetic energy (K_t) - the lowest level of turbulent kinetic energy in the test section was desired, indicating a low level of fluctuation in the flow; and,

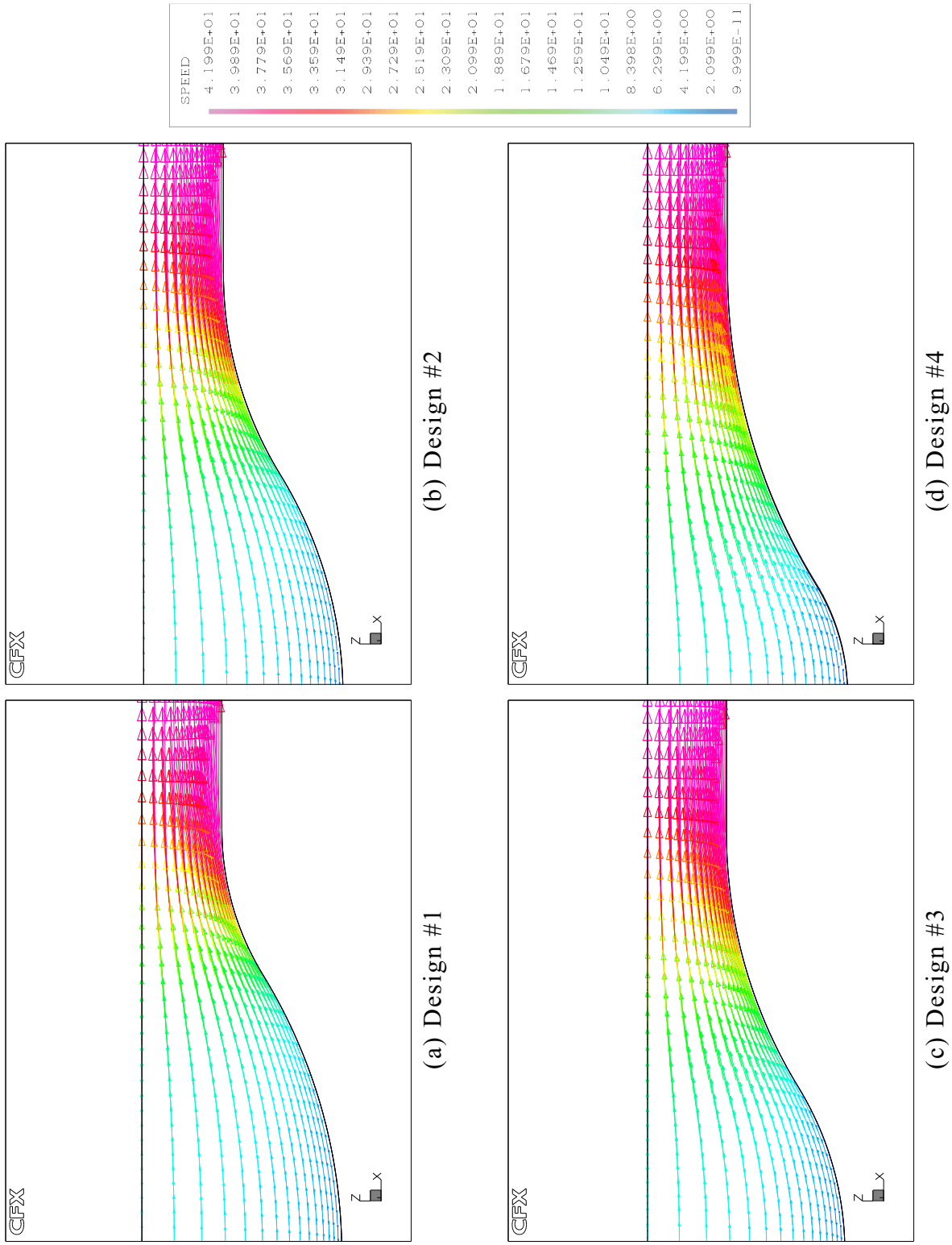

Figure 2.16: Mean velocity plots of designs #1 through #4 (along symmetry plane)

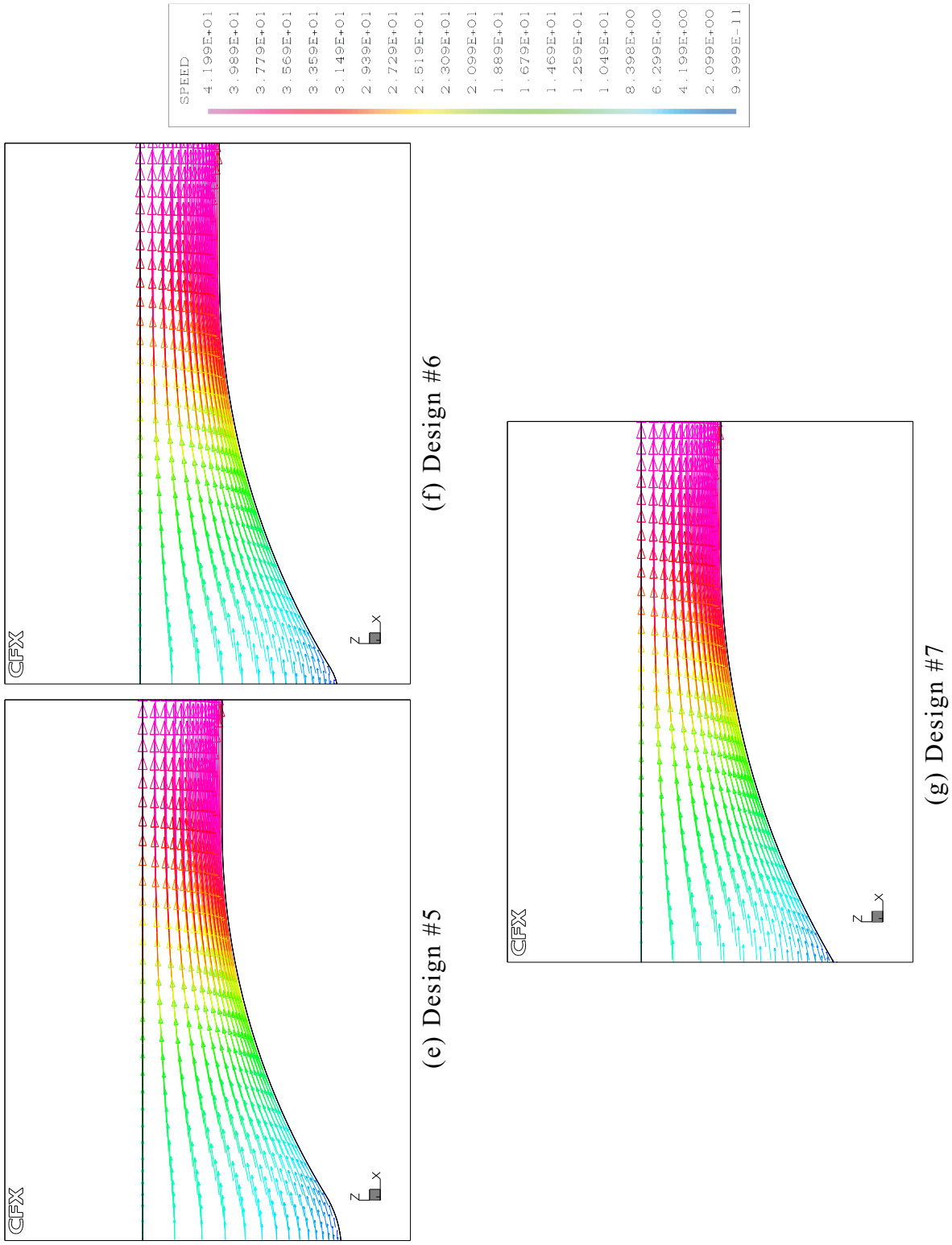

(e) Design #5

(f) Design #6

(g) Design #7

Figure 2.17: Mean velocity plots of designs #5 through #7 (along symmetry plane)

3. Average static pressure - comparing the average static pressure at the exit of the contraction would reveal which design imposed the least amount of resistance to the flow.

The flow uniformity was not sensitive to the curvature ratio, CR, and was therefore not included as one of the performance parameters. The three performance parameters above were compared over the entire Y-Z plane at x = 0.405m (the exit plane of the contraction). Due to the biasing of the mesh (*i.e.* uneven spacing), the values were numerically integrated over the exit plane. A two-dimensional trapezoid method was used to integrate each row of data in the Z-direction, and then those results were integrated along the Y-direction to obtain a single average value.

Average Velocity

Figure 2.18 is a plot of the average exit velocity at the contraction outlet versus its curvature ratio. Even though the largest difference in average velocity between the contractions was only 0.04%, a distinct inverse relationship between the curvature ratio and the average velocity was found. Based on the desire for the highest test section velocity, design #7 (CR = 0) provided the best performance of the seven geometries, although the results are very close.

Average Turbulent Kinetic Energy

In the case of turbulent kinetic energy levels, a more significant relationship with the curvature ratio was revealed (Figure 2.19). From design #1 to design #2 (CR of 1.905 and 1.103, respectively), a 14% decrease in turbulent kinetic energy was achieved. A further 18% decrease was observed in design #3 (CR = 0.649). Turbulent kinetic energy levels continued to fall as the CR dropped, with design #7 (CR = 0) yielding $k = 5.72 m^2/s^2$, nearly 57% lower than that of design #1 (CR = 1.905). Design #7 again displayed superior behaviour in the second of three performance parameters.

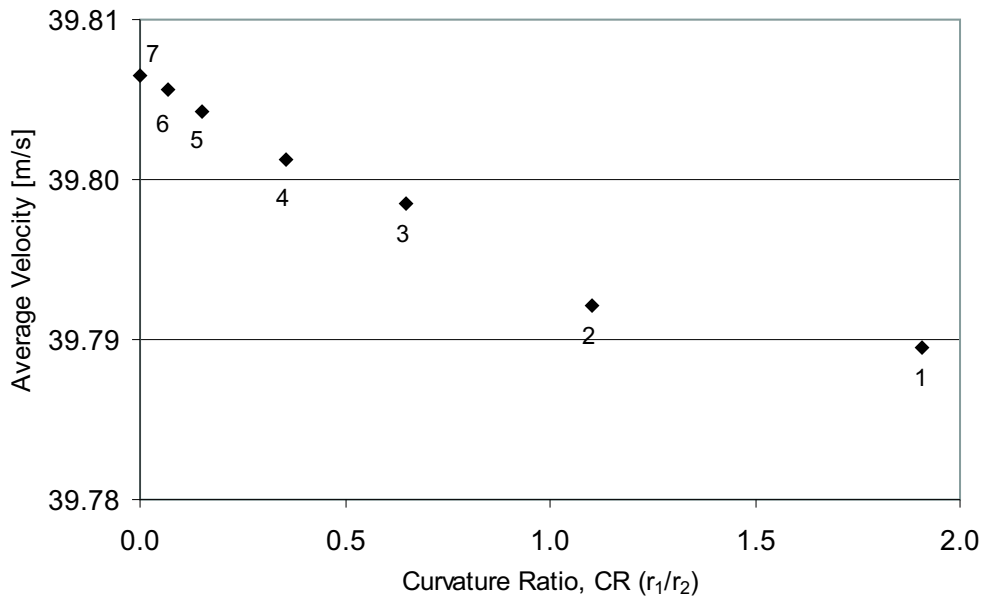

Figure 2.18: Average exit velocity plotted against the curvature ratio (data points labeled with corresponding contraction design number)

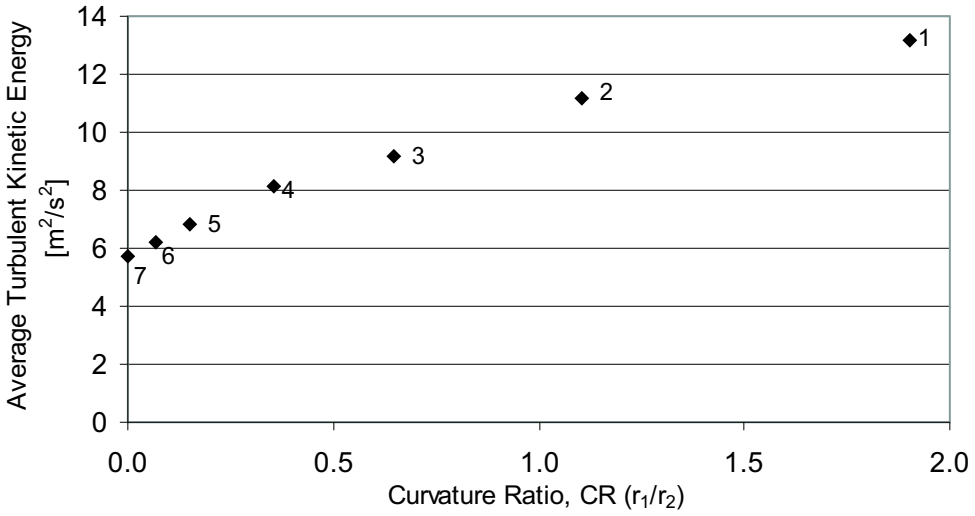

Figure 2.19: Average turbulent kinetic energy plotted against the curvature ratio (data points labeled with corresponding contraction design number)

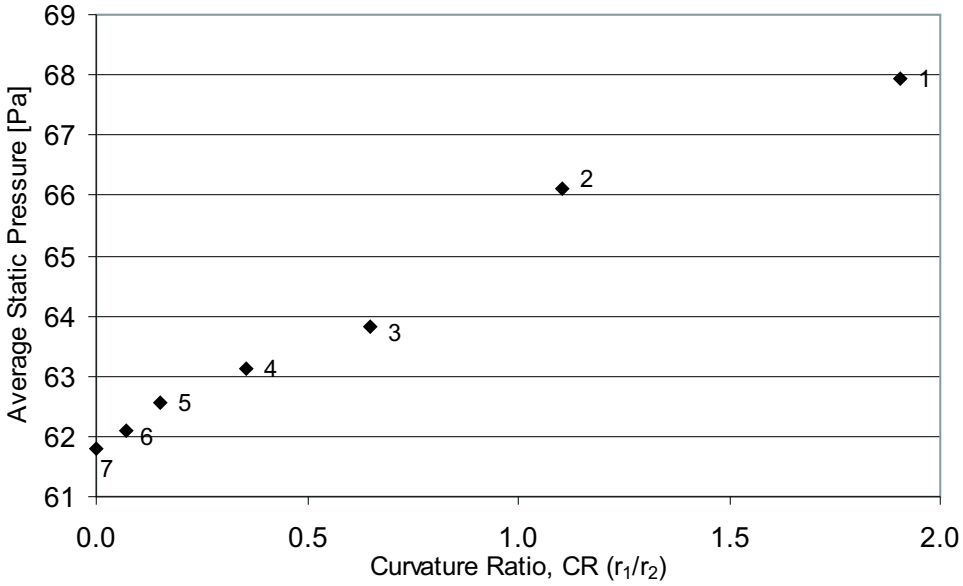

Figure 2.20: Average static pressure plotted against the curvature ratio (data points labeled with corresponding contraction design number)

Average Static Pressure

Figure 2.20 shows the average static pressure at the exit plane of each of the seven contractions. As was the case with turbulent kinetic energy, a nearly linear, direct relationship was observed between the level of static pressure in the flow and the CR. Design #7 had an average static pressure of 61.8 Pa, a 9% decrease from the initial design #1. It was interesting to note that the largest change in the average static pressure occurred between designs #2 and #3 (CR of 1.103 and 0.649, respectively), perhaps indicating the significance of CR = 1 as a transition point where the largest gain in pressure performance would be realized. A contraction with a CR of 1 would be a very balanced geometry, composed of two arcs of identical radius, and its point of inflection located halfway along the contraction length.

2.6.3 Final Design Selection

Seven different contraction designs with curvature ratios ranging from 0 to 1.905 were modeled for an upstream velocity of 6.4 m/s using CFX TASCflow. In order to compare the performance of each design, three parameters were tabulated at the exit plane of each contraction. The 7th design, with a curvature ratio of 0, displayed the highest average exit velocity, the lowest average turbulent kinetic energy, and the lowest average static pressure, making it the optimum design choice based on all three performance parameters.

The chosen contraction was of a novel design since it removed the need for the inlet side arc altogether, by utilizing only one circular arc to define its shape ($r_2 = 775mm$). At the time of writing, this particular contraction shape had not been encountered in any wind tunnel publication.

2.7 Selection of Honeycomb and Screens

In order to minimize the amount of turbulence and flow misalignment in the wind tunnel, it was necessary to introduce flow straighteners and screens within the tunnel circuit. The fan rotor is a major source of flow misalignment in a tunnel. As it rotats, it imparts a swirling (tangential) motion on the exiting flow, causing the air to rotate (about the axis of rotation of the rotor) as it movs downstream through the tunnel. In order to minimze this swirl, two sections of honeycomb were inserted, one section at the exit of transition 2 (before corner 1, Figure 2.1), and the second just upstream of the contraction in the settling chamber. The first section would act as a flow straightener immediately after the fan, removing a large portion of the swirl, while the second section would remove any remaining swirl as well as any transverse flow incurred through corners 1 and 2. In order to effectively reduce transverse velocities, the honeycomb length or depth is recommended to be a minimum of 6 to 8 times the cell size [1]. The honeycomb selected for this wind tunnel was made of $0.14mm$ thick aluminum, and was $76mm$ long with hexagonal cells measuring $9mm$ across flats. This gave a length to cell size ratio of 8.4.

One stainless-steel wire mesh screen was inserted into the wind tunnel just downstream of the honeycomb section in the settling chamber. An estimation of the turbulence reduction achieved

by the screen was carried out using the combined analyses of DeVahl [25], Prandtl [26], and Dryden and Schubauer [27].

The screen in question was first characterized by its porosity, β, defined as the ratio of the total projected open area to the total screen area:

$$\beta = \left(1 - \frac{d_w}{M}\right)^2, \tag{2.7}$$

where d_w is the wire diameter and M is the cell size. With a wire diameter of $0.5mm$ and a mesh size of $1.4mm$, the porosity, β was found to be 0.538. From DeVahl [25], the pressure loss coefficient, K was approximated by:

$$K = K_o + \frac{55.2}{R_{d_w}}, \tag{2.8}$$

where,

$$K_o = \left(\frac{1 - 0.95\beta}{0.95\beta}\right)^2 \tag{2.9}$$

and R_{d_w} was the Reynolds number based on the wire diameter, d_w. The Reynolds number was calculated to be 234, leading to a K of 1.15. Using the pressure loss coefficient, K, Prandtl [26] gave an expression for the estimation of the axial turbulence reduction factor, while Dryden and Schubauer [27] gave one for the lateral component of turbulence (denoted by the subscripts u and v, respectively):

$$f_u = \frac{1}{1+K} \quad , \quad f_v = \frac{1}{\sqrt{1+K}} \tag{2.10}$$

The turbulence reduction factors were found to be 0.47 and 0.68 in the axial and lateral directions, respectively. The turbulence level exiting the screen section was therefore expected to be reduced by 53% in the axial component, and by 32% in the lateral component.

2.8 Fan Selection and Energy Considerations

In order to properly select a fan which could propel the flow to the desired speed, it was necessary to first estimate the flow losses present in the wind tunnel circuit. This was done by estimating the energy ratio of the wind tunnel. The energy ratio is an important measure of the efficiency

of a wind tunnel, and is typically defined as the ratio of the power in the test section flow to the rate of flow losses around the circuit [2]. It is not uncommon to form alternative versions of the energy ratio. For example, the electrical power input or mechanical shaft power can also be chosen as the denominator in defining the energy ratio. For this analysis, the energy ratio was defined using the flow losses throughout the entire circuit:

$$ER = \frac{P_t}{P_c} \tag{2.11}$$

The power in the test section flow, P_t, was expressed as:

$$P_t = \frac{1}{2}\rho A V^3 \tag{2.12}$$

where, ρ is the fluid density, A is the cross sectional area of the test section, and V is the test section flow velocity. At a test section speed of 45 m/s, the power, P_t, was calculated to be 1253 W, or 1.68 Hp. In order to estimate the denominator of Eq. 2.11, the loss coefficient of each section in the wind tunnel must be summed. The remainder of this section summarizes the derivation of an expression for the energy ratio in terms of the circuit losses by using the methodology of Pope *et al.* [2].

The individual loss coefficient for each section can be expressed in the form of the energy equation with a pressure loss term, ΔH:

$$K_l = \frac{\Delta H_l}{(1/2)\rho_l V_l^2} = \frac{\Delta H_l}{q_l} \tag{2.13}$$

The subscript l denotes *local* section properties. The energy loss rate can then be expressed in terms of the local loss coefficient, K_l, and the volume flow rate through the section, or:

$$\Delta E_l = K_l(\frac{1}{2}\dot{m}V_l^2) \tag{2.14}$$

Since the energy ratio is defined with respect to the test section power, the local loss coefficients must be referenced to the test section dynamic pressure:

$$K_{lt} = K_l\frac{q_l}{q_t} \tag{2.15}$$

The expression of P_t (Eq. 2.12) can also be referenced to the test section:

$$\Delta E_l = K_{lt}(\frac{1}{2}\dot{m}V_t^2) = K_{lt}P_t \tag{2.16}$$

The total circuit loss, P_c, can be found by summing the rate of loss in each section:

$$P_c = \sum_l \Delta E_l = \sum_l K_{lt} P_t \tag{2.17}$$

and Eq. 2.11 can thus be expressed in terms of these section loss coefficients:

$$ER = \frac{1}{\Sigma_l K_{lt}} \tag{2.18}$$

At this point, the individual K_l coefficients for each section were estimated.

2.8.1 Constant Area Sections

For areas of constant cross section, a simple pipe flow analysis was adopted. Therefore, the loss coefficient could be expressed in terms of the friction factor, f, the section length, L, and the hydraulic diameter, D_h:

$$K_l = f\frac{L}{D_h} \tag{2.19}$$

From the Prandtl universal law of friction, the Colebrook equation gives an iterative expression for the friction factor of a smooth-walled pipe [28]:

$$\frac{1}{\sqrt{f}} = 2log_{10}(R_e\sqrt{f}) - 0.8 \tag{2.20}$$

where R_e is the Reynolds number based on the section mean speed and the hydraulic diameter. There were four such constant area sections in the circuit under investigation, the test section, the settling chamber, and the sections between corners 1 & 2, and 3 & 4. The results for the associated loss coefficients are given in Table 2.3.

2.8.2 Diffusers

For a diverging duct, the associated loss coefficient was commonly broken up into two components; the friction loss coefficient and expansion loss coefficient [2].

$$K_l = K_f + K_{ex} \tag{2.21}$$

	Dimensions [mm]	D_h [mm]	V [m/s]	R_e	f	L [mm]	K_l
Test Section	152 x 152	0.152	45.00	438,912	0.01348	450	0.0404
Settling Chamber	290 x 290	0.290	12.47	231,006	0.01520	432	0.0182
Duct Between Corners 1&2	381 x 381	0.356	8.27	188,105	0.01583	152	0.0064
Duct Between Corners 3&4	290 x 290	0.381	7.20	175,565	0.01605	244	0.0128

Table 2.3: Loss coefficients for constant area sections

The friction loss coefficient, K_f, was estimated as:

$$K_f = \left(1 - \frac{1}{AR^2}\right)\frac{f}{8sin\theta} \tag{2.22}$$

where AR is the area ratio, f is the friction factor calculated as in the case of a constant area section, and θ is calculated using the inlet and outlet hydraulic diameters, and the diffuser length, L:

$$\theta = arctan\left(\frac{D_{H,outlet} - D_{H,inlet}}{2L}\right) \tag{2.23}$$

The experimental data from Eckert *et al.* [29] was used in estimating the expansion loss coefficients:

$$K_{ex} = K_e\left(\frac{AR-1}{AR}\right)^2 \tag{2.24}$$

where,

$$K_e = \begin{cases} 0.09623 - 0.004152\theta & \text{for } 0 < \theta < 1.5^o \\ 0.1222 - 0.0459\theta + 0.02203\theta^2 ... + 0.00002337\theta^6 & \text{for } 1.5^o < \theta < 5^o \\ -0.01322 + 0.05866\theta & \text{for } 5^o < \theta \end{cases} \tag{2.25}$$

The losses for the diffuser, transition 1, and transition 2 were calculated using this method, and are tabulated in Table 2.4. Even though transitions 1 and 2 did not remain constant in cross section, this analysis was considered reasonable since both transitions typically only account for a combined 1.5% of the total circuit losses [1].

	AR	Re	f	L [mm]	θ [deg]	K_f	K_{ex}	K_l
Diffuser	3.61	438,912	0.0135	635	6.16	0.0145	0.1821	0.1966
Transition 1	1.51	231,006	0.0152	610	3.10	0.0197	0.0278	0.0475
Transition 2	1.15	188,105	0.0158	813	0.90	0.0305	0.0015	0.0321

Table 2.4: Loss coefficients for diffuser and transition sections

	Vane Chord [mm]	Local Cross Section [mm]	Local Velocity [m/s]	Re_c	K_l
Corners 1 & 2	36	381 x 381	7.20	16,589	0.2109
Corners 3 & 4	36	290 x 290	12.47	28,719	0.1962

Table 2.5: Loss coefficients for the corner turning vanes

2.8.3 Corners

The losses occurring in the corner turning vanes were split into two coefficients, the skin friction coefficient, K_f, and the loss coefficient due to the flow rotation, K_r. The experimental work of Wattendorf [30] concluded that the vortices generated by the turning of the flow accounted for two-thirds of the losses, while the skin friction accounted for the rest. He formed an expression for the total corner loss coefficient which combined the two components to give:

$$K_c = 0.10 + \frac{4.55}{(log_{10}Re_c)^{2.58}} \tag{2.26}$$

where Re_c was the Reynolds number based on the turning vane chord length and the local velocity.

The loss coefficient calculations are tabulated in Table 2.5.

2.8.4 Screens and Honeycomb Sections

The loss coefficient for the wire screen was approximated by using an expression from Pope *et al.* [2]:

$$K_l = K_{mesh} K_{Rn} \sigma_s + \frac{\sigma_s^2}{\beta_s^2} \tag{2.27}$$

D_h [mm]	ε	Re_Δ	β	L_h [mm]	λ_h	K_l
9.00	0.00015	0.6912	0.972	76.00	0.0120	0.1461

Table 2.6: Loss coefficients for the honeycomb sections

where β_s is the screen porosity (see section 2.7) and σ_s is the screen solidity, $\sigma_s = 1 - \beta_s$. The mesh factor, K_{mesh}, was estimated by Idel'chik [31] as 1.0 for new metal wire, and K_{Rn} is given by Eckert *et al.* [29] using the Reynolds number based on the wire diameter.

$$K_{Rn} = \left[0.785\left(1 - \frac{R_d}{354}\right) + 1.01\right] \tag{2.28}$$

With a porosity of 0.538 and a Reynolds number of 234, the loss coefficient for the screen was calculated to be $K_l = 1.23$.

The losses associated with the honeycomb sections described in section 2.7 were given by Eckert *et al.* [29] as:

$$K_l = \lambda\left(\frac{L}{D_H} + 3\right)\left(\frac{1}{\beta}\right)^2 + \left(\frac{1}{\beta} - 1\right)^2 \tag{2.29}$$

where

$$\lambda = \begin{cases} 0.375\left(\frac{\varepsilon}{D_H}\right)^{0.4} R_{e\varepsilon}^{-0.1} & \text{for } R_{e\varepsilon}^{-0.1} \leq 275 \\ 0.214\left(\frac{\varepsilon}{D_H}\right)^{0.4} & \text{for } R_{e\varepsilon}^{-0.1} > 275 \end{cases} \tag{2.30}$$

In Eq. 2.29, β is the porosity as defined in Section 2.7, D_H is the hydraulic diameter of the hexagonal honeycomb cell, and L is the thickness of the honeycomb in the flow direction. In Eq. 2.30, ε is the honeycomb material roughness, and $R_{e\varepsilon}$ is the Reynolds number based on the material roughness and the incoming velocity. For the honeycomb used in this study, the parameters mentioned above were calculated and tabulated in Table 2.6.

2.8.5 Contraction

The losses incurred in the contraction section were assumed to account for a small percentage of the total circuit loss, and was hence treated in a rudimentary fashion [2]. It was assumed that

the pressure loss was due to friction only, according to the standard law of pipe friction:

$$\Delta p = \int_0^{L_N} f \frac{\rho}{2} \frac{V^2}{D_H} dx \tag{2.31}$$

The results of the integral were found by Wattendorf [30] to be largely independent of the contraction shape, and he therefore formulated an approximation for the loss coefficient as:

$$K_l = 0.32 f_{av} \frac{L_n}{D_H} \tag{2.32}$$

where L_n is the contraction length, D_H is the hydraulic diameter of the test section, and f_{av} is taken as the average value of the friction factor between the contraction inlet and outlet (using the average velocity between the inlet and outlet). Based on this analysis, the loss coefficient of the contraction used in this study was 0.0126.

2.8.6 Total Circuit Losses

The loss coefficients associated with each wind tunnel component are summarized in Table 2.7. The K_l column contains the loss coefficient values from the previous sections, and K_{lt} are the same coefficients when referenced to the test section using the average velocity through the component and the dynamic pressure (Eq. 2.15). The rightmost column gives an idea of which components account for most of the losses within the tunnel. In this particular tunnel, the diffuser was the component with the highest loss for the circuit. Pope *et al.* [2] suggested that the diffuser, as well as the corners, typically account for more than half of the circuit losses. The main discrepancy from this reference was the high loss calculated for the test section (Table 2.7). This was to be expected since this particular test section was three times longer than typical test sections (its length was approximtely three times its side dimension). The friction losses were compounded here since the velocity is always highest in the test section.

The sum of the K_{lt} values in Table 2.7 gave a total circuit loss value of 0.21. When entered into Eq. 2.18, an energy ratio of 4.77 was calculated. The circuit power loss was then calculated from Eq. 2.11 to be 263 W (0.35 Hp). Therefore, the total power that was to be required from the fan was $P_t + P_c = 1516$ W (2.03 Hp). Based on a velocity of 45 m/s in the test section, the

Section	K_l	V_{avg} [m/s]	q_l	K_{lt}	% of Total Loss
Test Section	0.0404	45.00	1198.8	0.0404	19.29
Settling Chamber	0.0182	7.20	30.7	0.0006	0.30
Duct Between Corners 1 & 2	0.0064	7.20	30.7	0.0002	0.08
Duct Between Corners 3 & 4	0.0128	12.47	92.0	0.0010	0.47
Diffuser	0.1966	28.73	488.7	0.0801	38.23
Transition 1	0.0475	10.37	63.6	0.0025	1.20
Transition 2	0.0321	7.73	35.4	0.0009	0.45
Corners 1 & 2	0.4217	7.20	30.7	0.0108	5.15
Corners 3 & 4	0.3924	12.47	92.0	0.0301	14.36
Contraction	0.0126	26.10	403.3	0.0042	2.01
Screen	1.2253	7.20	30.7	0.0314	14.96
Honeycomb	0.2921	7.20	30.7	0.0075	3.57
				0.2096	100%

Table 2.7: Summation of wind tunnel loss coefficients

required volumetric flowrate was calculated to be 1.045 m^3/s. When selecting the fan however, this flowrate value was increased to 1.4 m^3/s in order to account for the decrease in flow at high static pressures. Details of the fan and drive system are given in Chapter 3.

To summarize, the design procedure outlined in this chapter resulted in the final wind tunnel geometry shown in Figure 2.1. Its fabrication is outlined in the following chapter .

Chapter 3

Wind Tunnel Construction

3.1 Introduction

As with most engineering projects, the potential of any design can only be realized if it is fabricated accurately according to the original design drawings. The case of a wind tunnel is no exception, since the length, shape, and surface finish of each section is critical to the end result - a uniform and adjustable airflow with low turbulence.

This chapter outlines the fabrication process as well as the materials used for the wind tunnel in this study. The fabrication of those components which presented unique challenges are described in more detail, while the simple, more conventional components are only briefly mentioned.

3.2 Test Section

The test section, as mentioned in Section 2.1, was where all aerodynamic measurements were to be performed. Since the tunnel was designed to be used with the optical measurement technique of PIV, it was logical to allow for the maximum optical access possible in the test section. For this reason, the test section was fabricated using transparent acrylic panels for all four walls.

Figure 3.1: Acrylic test section ($152.4mm$ x $152.4mm$ x $450mm$)

This would allow access for the laser and camera at any point around the test section, resulting in more convenient equipment setups. The four panels were fastened together using hex socket cap screws as opposed to adhesives in order to allow for access to the inside of the test section without moving any of the wind tunnel components.

3.3 Corner Turning Vanes

The fabrication of the corner turning vanes created a unique challenge due to the complex shape and structural demands imposed on them. Each turning vane needed to be as thin as possible to minimize flow blockage, and could only be fastened to the wind tunnel at the top and bottom of the vane. Several options were evaluated for their fabrication. One such option was to obtain lengths of thin-walled metal or plastic tubing, and slit the tubes longitudinally into four, quarter-circular sections. These could then be cut into individual turning vanes ready for installation. However, this would have required approximately 18 m of tubing and 70 m of cutting. As well, cutting tubes longitudinally and ensuring a straight cut along their entire lengths would be a very difficult task. This method was discarded for these reasons.

The alternative method was to form each turning vane from sheet metal blanks. Using Aluminum sheet of $0.635mm$ (0.025 in.) thickness, each vane was cut to the appropriate length and width

Figure 3.2: Turning vane fabricating tools

using a table shear. The use of the table shear gave smooth, straight cuts, and eliminated the need for any deburring of edges. Once the turning vanes were cut to the proper length and width, they could be formed from flat blanks into quarter circles. This was done with the use of a male and female half-circular die (Figure 3.2). Each piece of sheet aluminum was placed between the male and female die and pressed together using a hand press. The dies were chosen with a radius of $19mm$ (0.75 in.) to allow for springback in the metal, resulting in a $25.4mm$ (1 in.) radius in each turning vane. In Figure 3.2, the leftmost stack shows the turning vane blanks before forming, the dies are shown at the right, while the two middle stacks are completed turning vanes.

In order to securely hold and locate each turning vane, top and bottom rails were fabricated from acrylic. The rails were cut from $6.35mm$ (0.25 in.) thick acrylic, and measured $38.1mm$ (1.5 in.) in width. The lengths were determined by the diagonal dimension in each of the four corners: $539mm$ for corners 1 & 2, and $410mm$ for corners 3 & 4.

To locate each turning vane, circular grooves were machined along the length of each rail at $12.7mm$ increments. With these grooves, each turning vane could be inserted into one groove in both the top and bottom rails (Figure 3.3(a)). Once all the turning vanes were inserted, small drops of epoxy were placed in each groove, securing the turning vanes in place while still allowing the edges of the vanes to be manipulated and adjusted.

Figure 3.4 shows the method by which the turning vane assemblies were inserted and located in

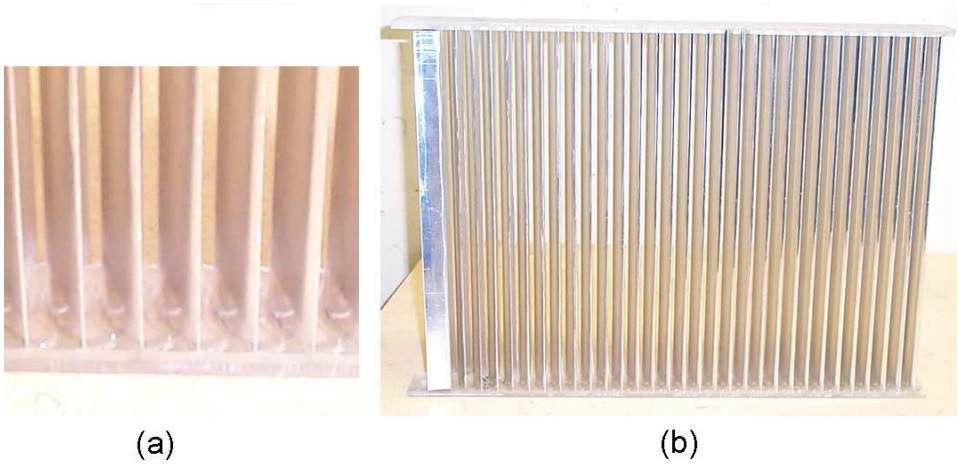

Figure 3.3: Turning vane and rail assembly: (a) locating rails (b) final turning vane assembly

a 38.1mm wide groove cut into the top and bottom of each corner along the diagonal so that the entire turning vane assembly would slide into the corner. Each groove was 6.35mm deep so that the top and bottom rails of each assembly would be flush with the floor and roof of the wind tunnel.

3.4 Transitions

In the cases of transitions 1 and 2, a conversion from a square to a circular cross section was required in order to blend smoothly with the fan section. These parts are usually made with sheet metal, formed to the appropriate transition shape and then welded along a seam to seal the duct. In an effort to maintain consistent use of one material in as many components as possible, an alternate technique was developed.

For this study, both transition pieces were fabricated using medium density fiberboard (MDF) panels fastened together. Their cross sections therefore remained square, and the transition to a circular cross section was performed with styrofoam filler sections. Blocks of high density insulation styrofoam were cut using a hot wire cutter to form a shape with a 178mm radius at

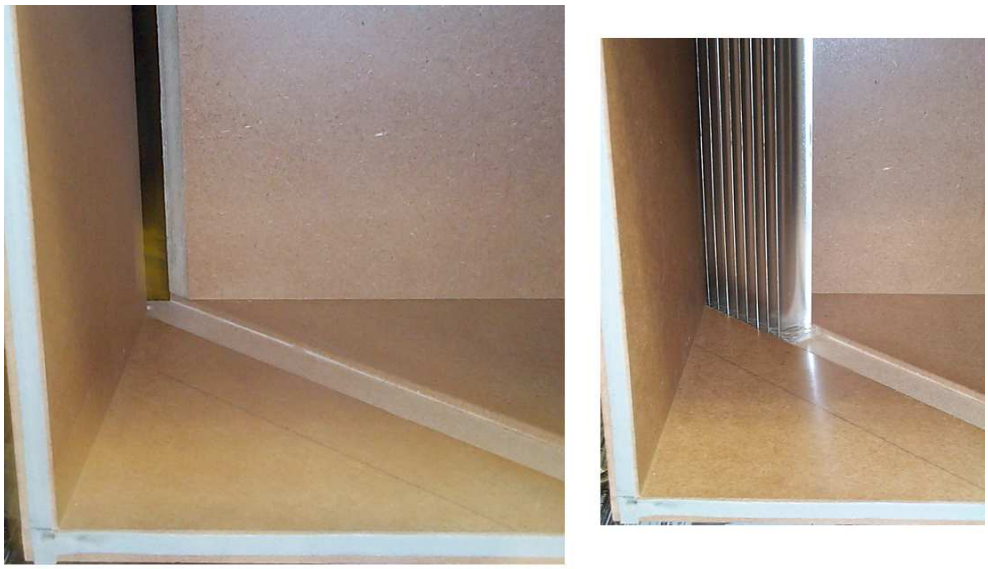

(a) (b)

Figure 3.4: (a) Locating groove for turning vane assembly in corner 3 (b) insertion of turning vanes into corner 3

Figure 3.5: Transition 1 with styrofoam filler sections

one end (to mate with the fan), and decreasing to a point ($0mm$ radius) at the other end (see Figure 3.5). These sections were coated with epoxy resin which sealed and hardened over the soft styrofoam surface. They were then fastened and glued into the transition corners and the transitions were completed with a wooden flange with fastening holes for the fan section.

3.5 Contraction

The contraction section was another component which presented a unique fabricating challenge. Its curvature did not allow for the use of wood panels as with the other straight sections. The fabrication of the contraction required, above all, the accurate forming of the radius which made up each of the four walls. It was decided that this shape could most easily be made from reinforced epoxy resin formed over a male mold of the contraction shape.

The male mold for the contraction was fabricated from high density insulation styrofoam, and was cut using a hot wire cutter. Figure 3.6 shows the apparatus used to swing the hot wire along

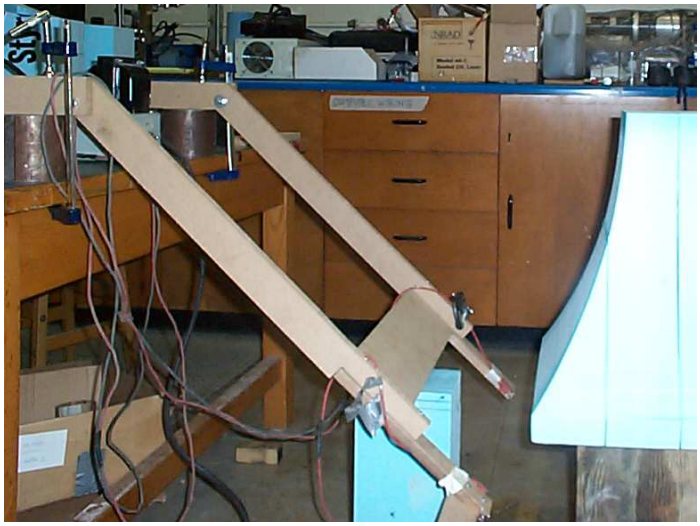

Figure 3.6: Hot wire cutter used to form the male contraction mold

a $775mm$ radius (as per the design outlined in Section 2.6). The block of styrofoam was located and held in place while the hot wire was allowed to swing down, cutting an arc of constant radius into the block. This was repeated until all four sides were cut.

The mold was then sanded and filled to remove any surface imperfections, and a flat styrofoam panel was glued to the top and bottom to form fastening flanges for the contraction (Figure 3.7). The mold was then wrapped in packing tape which acted as a mold release layer as well as a control surface for the final part. The contraction section was made using a wet layup technique with glass fibre reinforced epoxy. Sections of Nomex honeycomb were inserted between the glass fibre layers to increase the stiffness of the four walls. The styrofoam mold was then removed from the part, leaving a smooth surface finish from the packing tape.

3.6 Fan and Speed Controller

The main characteristics of the fan, such as the size, flowrate, and required power were determined in section 2.8. Based on these criteria, a tube axial fan (Type AID-143) was purchased from

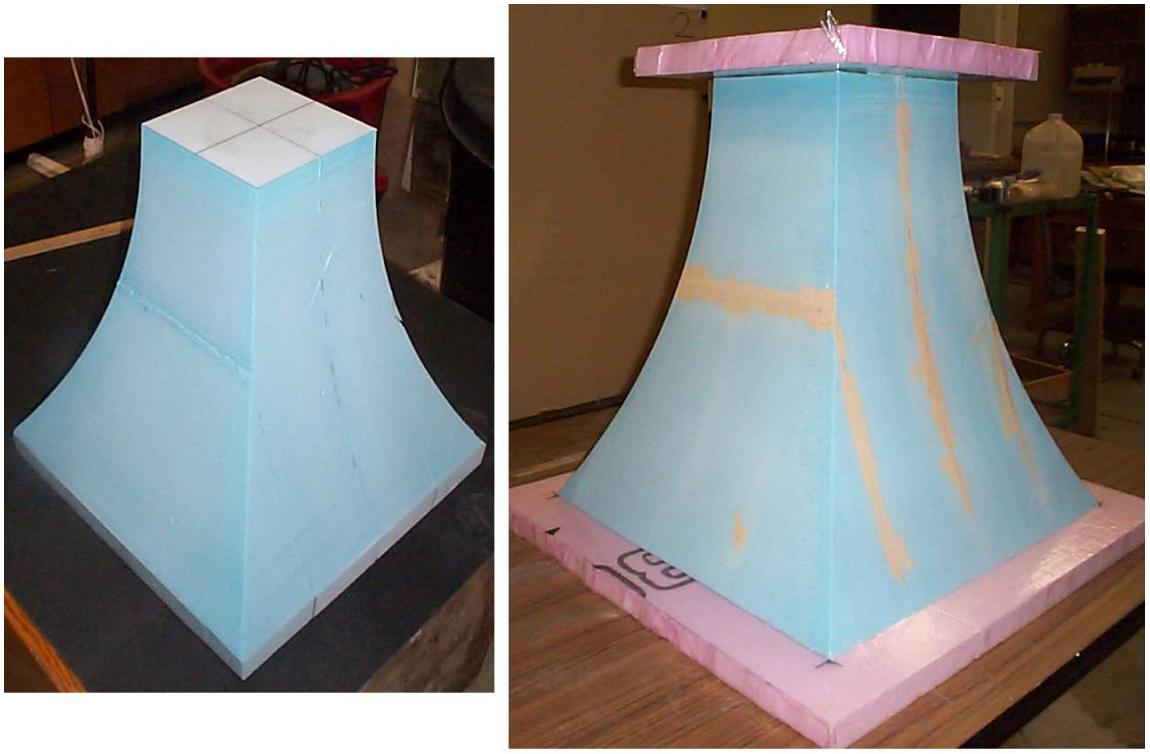

(a) (b)

Figure 3.7: Contraction mold a) after hot wire cutting, b) after filling and sanding with flanges added

Enviro-Tech HVAC Products (Ancaster, Ontario). The fan casing was $508mm$ (20 in.) long with a diameter of $356mm$ (14 in.). The impeller consisted of five cast aluminum blades, and was directly driven by a 1500 W (2 Hp), 208 VAC motor. At 3450 rpm, the fan was capable of a flowrate of approximately 1.4 m^3/s (3000 ft^3/min). Fan performance curves have been included in Appendix A.

A variable frequency drive (Teco Speecon 7210M) was purchased from MDI systems (Salt Lake City, Utah) in order to vary the motor rotational speed. The unit took a 208 VAC, 3 phase input and varied the output frequency from 0 to 60 Hz. With the variable frequency drive, the fan exit velocity was continuously adjustable from nearly 0 m/s up to 10 m/s (60 Hz). The control unit was fastened to the outside wall of transition 2 (Figure 3.8).

3.7 Remaining Components

All remaining wind tunnel components (excluding the test section, contraction, and fan section) were fabricated using $16mm$ thick medium density fiberboard (MDF). The panels were fastened using wood screws as well as carpenter's glue in order to seal each component. Before assembly, a layer of clear coat paint was applied to the inside of each component. This was done to protect the wood from oil which collects on the tunnel walls due to the condensation of the smoke used for PIV measurements.

The wind tunnel was placed on a table top, raising it nearly 1 m from the ground. This created a more convenient setup for inserting test models, running experiments, and modifying the tunnel. The completed tunnel is shown in Figures 3.8 and 3.9.

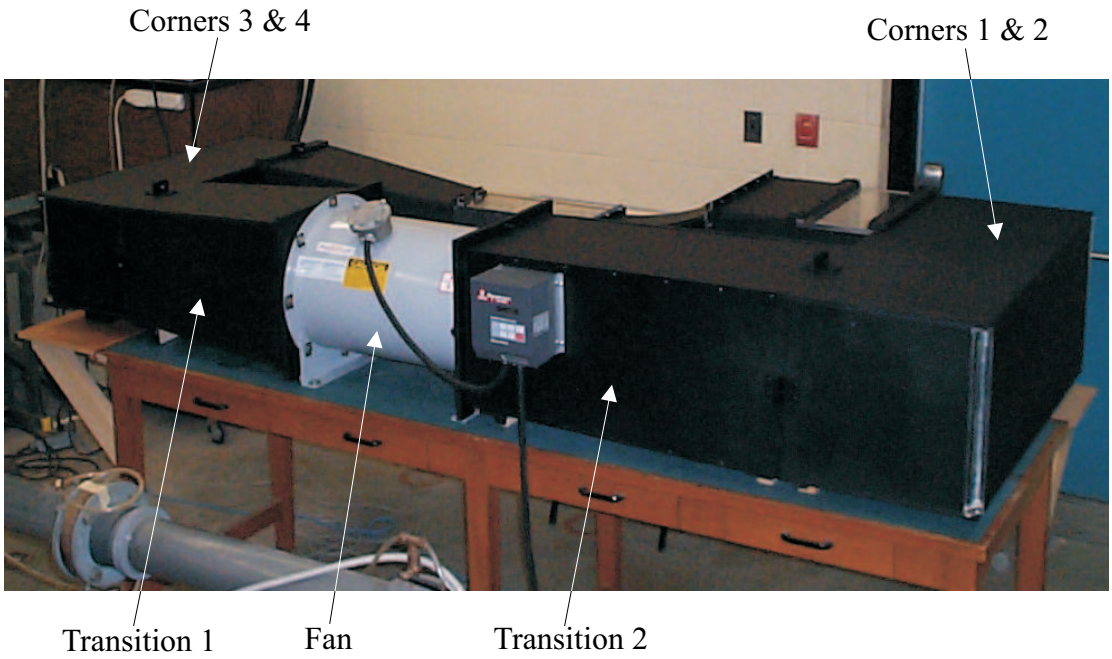

Figure 3.8: Fan side view of the completed wind tunnel

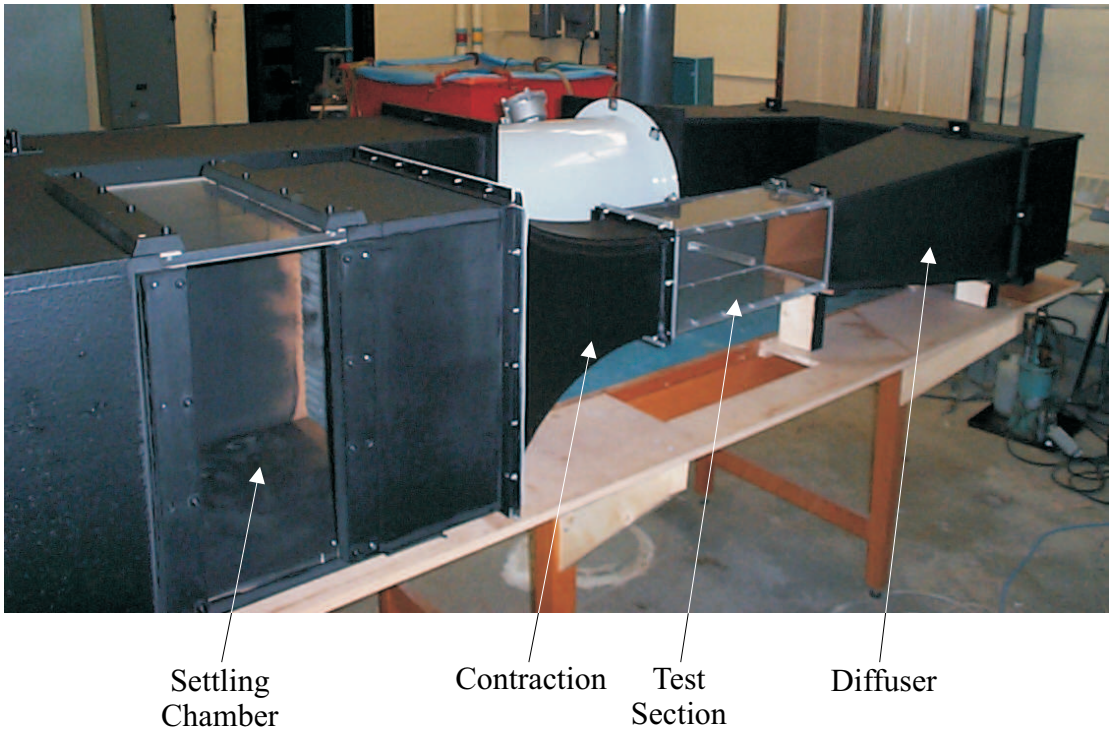

Figure 3.9: Test section side view of the completed wind tunnel

Chapter 4

Particle Image Velocimetry in the Wind Tunnel

4.1 Introduction

In this chapter, a literature review is provided which outlines the main types of measurement techniques available for use in wind tunnel flows. This is followed by an overview of the theory behind particle image velocimetry (PIV). Afterwards, a brief literature review is included, examining previous works involving both wind tunnels and the PIV measurement technique. The chapter closes with a description of the experimental setup and hardware used to obtain the measurements in this study.

4.2 Literature Review - Measurement Techniques for Wind Tunnel Flows

The classic type of measurement in the wind tunnel is pressure measurement in order to calculate velocity. Perhaps the oldest method for measuring pressure is the manometer, where a pressure

differential can be calculated by measuring the vertical displacement between two conjoined columns of fluid. The manometer remains one of the oldest methods of measuring pressure in a wind tunnel [32]. A more modern method of pressure measurement is the pressure transducer, which can be loosely defined as a device which takes a change in pressure and returns an electrical signal [2]. The various types of pressure transducers are described by Benedict [32] and Soloukhin [33]. In comparison to manometers, pressure transducers provide higher accuracy, sensitivity, and the potential for connection to a data acquisition system. Both manometers and pressure transducers are typically connected to a pressure measurement probe which is inserted into the flow. The types of probes used for the measurement of pressure are discussed by Pope *et al.* [2].

For the measurement of velocity, flow visualization techniques are gaining popularity due to their non-intrusive characteristics. Velocities are measured optically, usually through a window so that no instrumentation is needed in the actual flow field. Early methods of flow visualization were comprised mainly of tufts, or streamers attached to the surface of a model [2]. These short, light pieces of string (or other suitable material) would align themselves with the surrounding flow, revealing qualitative flow patterns near the model surface. In order to investigate the flow further away from the model surface, smoke or dye visualization is typically used. For air flows (as in this study), smoke is injected into the flow and is either watched, photographed, or filmed. The numerous options available for smoke generation, injection, and image recording are discussed in detail by Smits and Lim [34].

The non-intrusive methods introduced thus far are only capable of providing qualitative observations in a flow field. However, it is often desirable to obtain a more comprehensive characterization of the flow in question. One such non-intrusive, but quantitative measurement technique is Laser Doppler Velocimetry (LDV). In general terms, LDV uses a measurement area formed by the intersection of two laser beams. These beams intersect to form an interfernce pattern, and particles passing through this area will create a signal which can be retrieved by a photodetector and converted into a velocity. LDV can be used in high speed air flows, and can perform velocity measurements at high frequencies with a high level of accuracy [2]. Its main disadvantage in the case of wind tunnel flows is that it is a point measurement technique. LDV can therefore only determine velocities at a single point in the flow for each setup. In order to measure an entire test section flow, the LDV system would typically be mounted on a traversing assembly to avoid

unnecessary setup time.

The natural progression of non-intrusive measurement methods has led to a technique which is capable of high accuracy velocity measurements over a larger space to give more complete coverage of a flow field. The development of PIV has made such full-field measurements possible.

4.3 Particle Image Velocimetry

4.3.1 Seeding

As briefly described in Section 1.2, particle image velocimetry (PIV) operates by capturing two snapshots of a flow field separated by a short time interval. PIV actually measures the displacement of seeding particles injected into the flow, and not the flow itself. These particles are needed because individual fluid particles, such as air or water molecules, cannot be distinguished by a camera. Instead, the camera photographs seeding particles which reflect light and can be located in each successive image. For this reason, seeding particles must be chosen very carefully so that they follow the flow closely. A seeding particle that is too heavy will not be carried by the flow as easily and will be slow to react to changes in velocity. A particle that is too light may be dominated by buoyancy forces, also resulting in inaccurate flow tracking. In addition, the particle size must be large enough to scatter enough light to be seen by the camera. In the ideal case, the chosen seeding particle should have the same density as the fluid, making it neutrally buoyant with respect to the flow [35]. Basset [36] and Hinze [37] showed that a neutrally buoyant particle could be found by balancing the accelerating force with the sum of the drag due to both vicous and unsteady motion, the pressure gradient force, and the fluid resistance to the accelerating particle. A full description of various seeding particles and their selection can be found in Melling [38], Grant [39] and the Dantec User's Guide [35].

In this particular study, the fluid under investigation was air. Melling [38] suggested several seeding particle choices for gas flows including TiO_2 (titanium dioxide), Al_2O_3 (dialuminum trioxide), and several types of vapourized oils. Vapourized mineral oil was chosen as the seeding

particle for all the PIV measurements conducted in this study. This was chosen for several reasons:

1. Its vapour density is close to that of air, $\rho_{vap} \approx 6.76 kg/m^3$ (this value was estimated from other seeding particles with known vapour densities);
2. One litre of mineral oil can produce large amounts of smoke (enough for over 100 hours of PIV measurements in this case), making it an economical seeding particle;
3. It could be easily vapourized and injected into the wind tunnel;
4. Smoke could be easily removed from the wind tunnel at the conclusion of an experiment by venting it out from any opening in the tunnel; and,
5. It has low toxicity levels.

Prior to all PIV measurements, small amounts of mineral oil were poured into a smoke generator at regular intervals. The smoke generator acted simply as a hot plate, vapourizing droplets of mineral oil as they came into contact with it. With small bursts of compressed air, the smoke could then be pushed out of the generator and directly into the wind tunnel. The smoke was injected just upstream of the fan section, through a hole in the wall of transition 1. The location of smoke injection was not critical since the flow in the wind tunnel recirculated several times a second, resulting in very rapid mixing.

At the conclusion of an experiment, the smoke was vented from the tunnel by removing an acrylic section in the settling chamber and running the fan at low speed, allowing the smoke to escape into the surroundings. By doing this immediately following PIV measurements, most of the smoke was removed from the tunnel before it could condense back into mineral oil and deposit in critical areas such as the motor internal windings.

4.3.2 Capturing of PIV Images

Figure 4.1 shows a typical PIV setup, composed of a two-dimensional laser light sheet and a camera oriented perpendicular to it. Once the camera has been focused on the light sheet, PIV

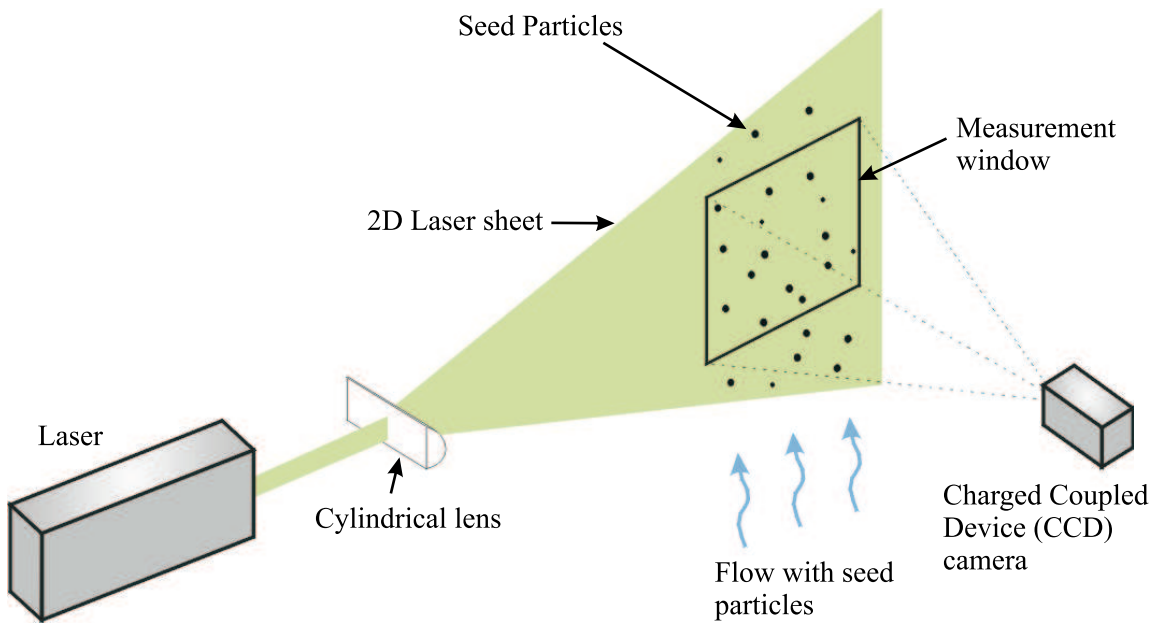

Figure 4.1: PIV overview [40]

images are ready to be captured. Since the laser must emit a light sheet of very high intensity over a small time interval, it is critical that the camera is synchronized with each laser burst. This is done with a central processor, which synchronizes the laser and camera, and ensures that each image is taken at the set time separation. The time separation between the two images in an image pair is set by the user and must be selected based on the predicted velocities and the size of the interrogation areas used for cross correlation. The process of cross correlation will be discussed in the following section.

The high speed camera utilizes a charged coupled device (CCD) to temporarily store each image before it is uploaded to a computer. The images must contain a black background in order to provide enough contrast so that the illuminated seeding particles can be distinguished. Figure 4.2 shows a typical PIV image collected in an air flow. The specks of light represent the seeding particles passing through the two dimensional light sheet. Each image collected is stored as an array of pixel values ranging from 0 to 255, with 0 being the darkest and 255 being the brightest

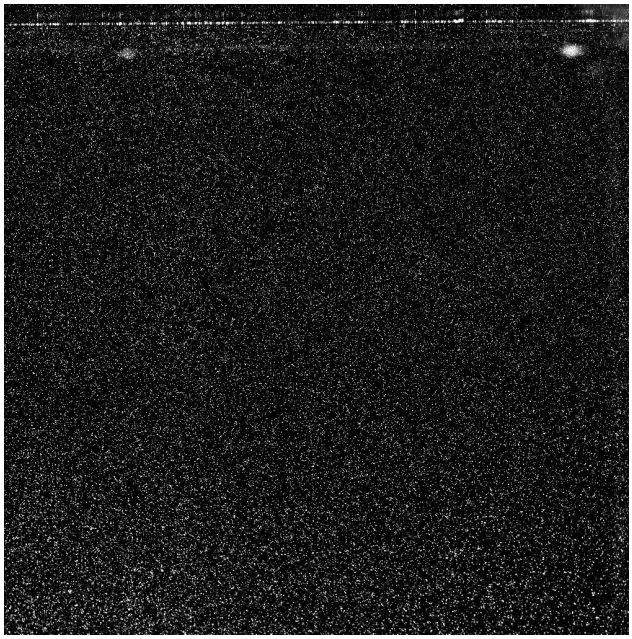

Figure 4.2: Typical PIV image captured in an air flow (approximate size, $85mm$ x $85mm$)

light intensity. Once two of these images are collected, the process of cross correlation can be performed to obtain velocity information.

4.3.3 Cross Correlation

Each cross correlation takes place between a single pair of images, image A, and image B captured a short time after. The images are broken up into smaller areas, called interrogation areas (Figure 4.3). The size of the interrogation area, N (in pixels), should be chosen so that the particle displacements within the area do not exceed $N/4$ [41]. Even with this criteria satisfied, it is still possible that particles near the edge of an interrogation area will move into the adjacent interrogation area by the time image B is captured. This is demonstrated in Figure 4.3, where particle (b) moves into the next interrogation area (solid line) in image B. This can result in erroneous displacement data near the edge of the interrogation area due to the "loss" of that

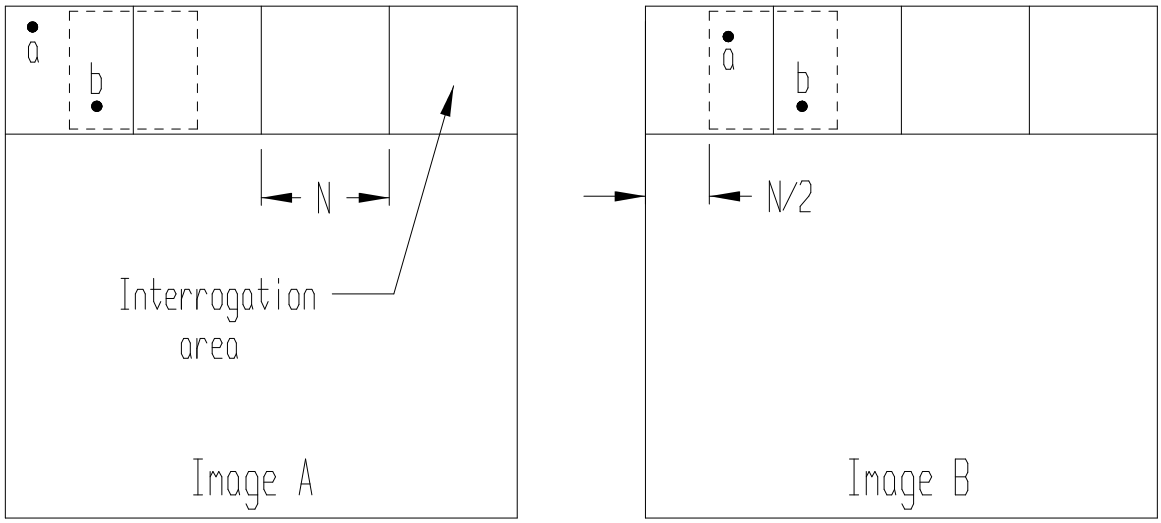

Figure 4.3: PIV image broken up into smaller interrogation areas

pair. To reduce this error, interrogation areas can be overlapped. For example, if an overlap of 50% is used, there will be a new interrogation area every $N/2$ pixels. The areas in broken lines in Figure 4.3 represent the location of the second interrogation area if 50% overlap was used. With this overlap used, particle (b) would be retrieved in the cross correlation of the second interrogation area (broken lines). Therefore, the two main user inputs required for cross correlation are the interrogation area size in pixels and the amount of overlap used.

Once these two parameters are determined, cross correlation can begin between each corresponding interrogation area in image A and B. The cross correlation algorithm used for all PIV measurements in this study utilized the fast Fourier transform (FFT) to determine the particle displacements in each interrogation area. Details of the FFT-based cross correlation technique can be found in [41, 42, 43, 44, 35]. The end result of the cross correlation is a displacement for each pair of interrogation areas in the image pair, which represents the mean particle motion within the interrogation area. The displacement has two components, Δx and Δy, and is given in pixels. In order to obtain actual particle velocities from these measured displacements, two other pieces of information are needed. First, the time separation, Δt, between the capturing of image A and B is needed so that the displacement can be converted into a velocity of pixels per second. To

then convert that velocity into a physical value such as meters per second, a magnification factor, M, is needed which relates the number of pixels in the image to a physical dimension in the flow. The velocities in the x and y directions, u and v, can therefore be calculated as:

$$u = M\frac{\Delta x}{\Delta t} \quad , \quad v = M\frac{\Delta y}{\Delta t} \tag{4.1}$$

The two velocities determined are then located at the center of the interrogation area from which they were determined.

4.3.4 Sources of Error in PIV

In this section, the various sources of error associated with PIV are briefly described. With PIV being a relatively new measurement technique (its widespread use did not begin until the 1990's), many of the error sources have been identified but not quantified accurately. This is due to the fact that many PIV errors depend greatly on the physical measurement environment such as the nature of the flow (*i.e.* acceleration present in the flow), and the exact size and shape of the seeding particles. For this reason, the errors listed in this section will be outlined qualitatively, although a quantifiable percentage error will be quoted wherever possible. The various errors described below are generally classified as either random errors or bias errors [45].

Random Errors

Random errors are classified here as any error which can result in either the overestimation or underestimation of the true answer. Since these errors cause the measurement to fall above and below the true value with equal probability, random errors can be reduced with averaging if the sample size is large.

1. Image Recording

   Errors originating from the image capturing process have been attributed to noise in the recording device by Pickering and Haliwell [46]. The level of resolution in the recording device can also effect the amount of error in the results [47, 48, 49].

2. Contrast in the Recorded Images

   As mentioned in Section 4.3.2, it is important that the images captured with PIV have an adequate level of contrast between the bright particles and the dark background. If the ratio of the brightness of the particles to the brightness of the background (referred to as the signal-to-noise-ratio, SNR) is too low, it will become increasingly difficult to distinguish the seeding particles from the rest of the background. This will adversely effect the accuracy of the predicted displacements. Guezennec and Kiritsis [50] suggested that the amount of error was insensitive to the SNR as long as it was kept above a certain critical value of approximately 100 counts of contrast. In this context, contrast refers to the difference between the particle intensity and the background intensity, and a count is a unit of measurement for intensity.

3. Particle Size

   Errors in the predicted displacement can arise from improper particle sizes in the captured image. For example, if a seeding particle takes up less than one pixel in a recorded image, there is no way to determine its exact location because one pixel can only hold one intensity value. Consequently, if that particle happened to be located in the upper left hand corner of the pixel, there would be no way to resolve this location. It is therefore important that the camera be adjusted such that the seeding particles (as captured in the camera images) are at least 2 pixels in diameter. Figure 4.4 shows a prediction of the relationship between the error (in pixels) and the particle image diameter (also in pixels) given by Prasad *et al.* [47].

4. Particle Number Density

   The number of particles which appear in each interrogation area can affect the accuracy of the cross correlation. Each interrogation area should contain more than 10 to 20 particles to attain acceptable levels of error [43, 39]. Huang *et al.* [49] suggested a relationship between the random error and the number of particles in an interrogation area which is plotted in Figure 4.5.

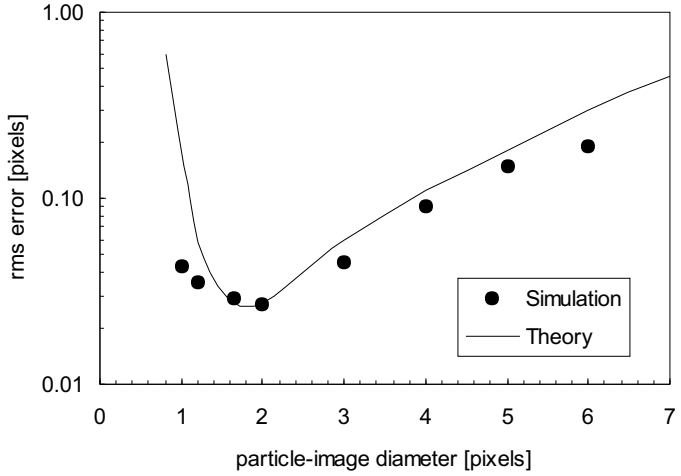

Figure 4.4: Error in determined displacements (in pixels) as a function of the particle image diameter [47]

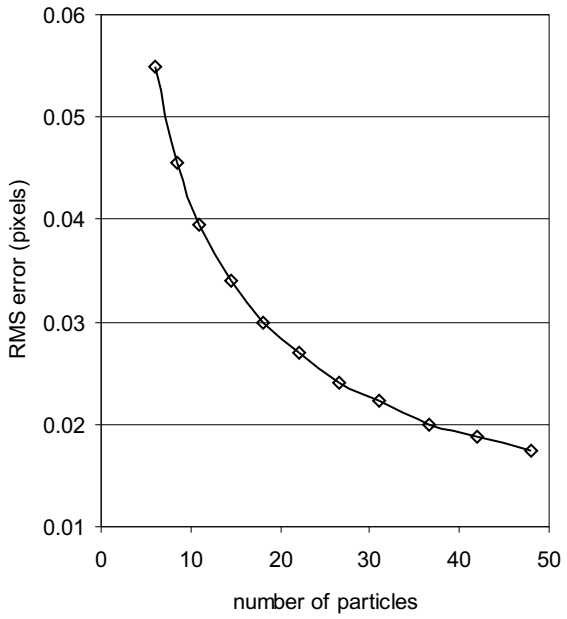

Figure 4.5: Error in determined displacements (in pixels) as a function of the particle density [49]

5. Three-Dimensional Effects

   Even when it is reasonable to assume a purely two-dimensional flow, some degree of out-of-plane motion exists in most physical flow fields. It is possible that any given particle with enough out-of-plane motion could pass through the laser sheet before the second image of an image pair is captured. This would result in a failure to find that matching particle in the second image, causing a reduction in the SNR. To prevent this effect, it was suggested by Adrian [43] that the seeding particles should not travel more than one-quarter of the laser sheet thickness before the second image is captured.

6. Parallax

   As mentioned above, the error due to out-of-plane motion can be minimized with a laser sheet that is at least 4 times thicker than the out-of-plane motion. However, if the laser sheet becomes too thick, the error due to parallax will increase. Parallax error occurs when particle displacement in the out-of-plane direction is interpreted as an in-plane displacement. This error can be quantified if the out-of-plane velocity is known [51], and can be reduced if the distance between the camera lens and the measurement plane is increased.

Bias Errors

In contrast to random errors, bias or fixed errors will cause the measurement to be either consistently above or below the true value.

1. Tracking Error

   Tracking error occurs when the seeding particles do not follow the flow exactly. Since PIV measures the displacement of seeding particles, it is essential that they are chosen so that they are neutrally buoyant in the flow (Section 4.3.1).

2. Acceleration Errors

   In the cross correlation of an image pair, it must be assumed that the velocity remains constant over the time interval since the only three pieces of information available are the

starting and finishing position of the particles, and the elapsed time for this displacement. The path taken by the particle is not known (*i.e.* the particle may follow a curved path, or may change speed along a straight path). Therefore, acceleration cannot be measured with PIV unless more than two images are used in a cross correlation technique [52]. An estimation of the acceleration errors in PIV can be found in Boillet and Prasad [53].

3. Velocity Gradient Errors

   During cross correlation, one velocity vector is calculated for each interrogation area. However, these areas have some finite size (N), so it is possible that different particles within the interrogation area could have different velocities. For this reason, it is wise to use smaller interrogation areas when high velocity gradients are expected. The errors resulting from the assumption that all particles within an interrogation area display uniform motion were investigated by Huang and Fielder [54].

4. Sub Pixel Interpolation

   Sub pixel interpolation errors are similar to the particle size errors described above. Unless the particle displacements within an interrogation area happen to be an exact integer value of pixels, then some sort of interpolation is required. The various functions available for estimating the exact displacements are described by Gilbert [40]. Based on the theoretical and simulation results of Westerweel [55], typical sub pixel interpolation errors are in the range of 0.05 to 0.1 pixels.

For each of the experiments performed in this thesis project, the above error sources were evaluated and quantified wherever possible. The results are reported in each corresponding chapter.

4.4 Literature Review - Particle Image Velocimetry and the Wind Tunnel

This section briefly reviews the existing publications pertaining to the use of PIV in wind tunnels. At present, this topic remains largely unexplored, as is evidenced below by the small number of publications found in this literature search.

The earliest publication found involving the use of PIV in a wind tunnel was from 1989. Hocker and Kompenhans [56] investigated ways to improve the performance of their PIV system for the measurement of low and high speed air flows. Some technical improvements involved replacing photographic film with a CCD camera for digitizing the recorded images, and determining efficient methods for (image) brightness control and seeding concentration. These improvements were made with the purpose of justifying PIV as a feasible measurement technique in the wind tunnel, and are now recognized as standard practices in PIV measurements.

Willert *et al.* [57] investigated various applications of a two dimensional PIV system in the 6×8 m^2 test section of the DNW Large Low Speed Testing facility (German-Dutch wind tunnel). PIV was used to measure: (1) helicopter rotor blade/vortex interactions, (2) flow in the wake of an aircraft in landing configuration, and (3) the flow between the slats of a high-lift airfoil. Willert *et al.* concluded that in light of these successful experiments, PIV should be considered a very promising technique for wind tunnel measurements [57].

Willert [58] later explored the application of stereoscopic PIV in the wind tunnel. Stereoscopic PIV uses two cameras to record image pairs simultaneously in order to capture the third (out-of-plane) velocity component. A detailed description of stereoscopic PIV was given by Willert [58] as well as in [59, 60, 61, 62, 63]. Willert [58] tested the three dimensional PIV system by performing measurements of an unsteady vortex ring. He concluded that an extension from two to three dimensional PIV would be possible in most wind tunnel applications [58].

Arik and Carr [64] investigated the use of a PIV system for real-time measurements in the wind tunnel. The main difference with this system was the ability to quickly adjust parameters such as the time separation between images, the image quality, and the cross correlation parameters such as the size of the interrogation areas and the overlap. These capabilities are now common in the majority of commercial PIV systems. Arik and Carr [64] used this system to perform measurements of the flow along the fuselage and behind the wing flaps of a transport aircraft. It was interesting to note that Arik and Carr [64] attempted to inject the seeding particles just upstream of the model (local seeding). They reported this method to be unsuccessful due to the intermittency of the smoke stream in the collected images. Instead, it was decided to seed the entire tunnel by running the smoke generators and the tunnel for one hour before collecting

images. Despite this, Arik and Carr [64] also reported a successful application of PIV in a wind tunnel flow.

A recent application of PIV in the automotive industry was performed by Cogotti and De Gregorio [65], where a full scale automobile was tested in an open section research tunnel. PIV measurements were made immediately downstream of the side view mirrors and the front wheels with a two dimensional PIV system. Vapourized olive oil was chosen as the seeding particle, and was injected into the flow at the contraction inlet with a traversing seeding rake. For comparison, the same areas were investigated using both LDV and a 14-hole pressure probe and found to give good agreement with the PIV results. The authors concluded that PIV showed a great deal of potential for use in automotive wind tunnels [65].

4.5 PIV Hardware Setup

This section describes the PIV hardware components used to obtain the flow measurements in this study (Figure 4.6). Since the same equipment was used for all the experiments in Chapters 5, 6, and 7, this description has been included here for convenience.

4.5.1 Laser

The laser unit used in this study was a New Wave Gemini 15Hz dual cavity Nd-YAG laser (the 15Hz reported here refers to the frequency at which pairs of laser pulses can be emitted). This unit actually contained two lasers, allowing for very small time separations (Δt) between pulses since it was not necessary to wait for a single laser to recharge before emitting a second light burst. The New Wave Gemini was capable of producing two $500mJ/5ns$ laser pulses at a wavelength of $532nm$. Along with the time separation between laser bursts, the user could also vary the intensity of the laser beam. This was generally kept in the range of 75% of full power, as this was usually enough to provide properly illuminated PIV images. The optics which spread the laser beam into a two dimensional sheet could also be adjusted. The main user adjustment of

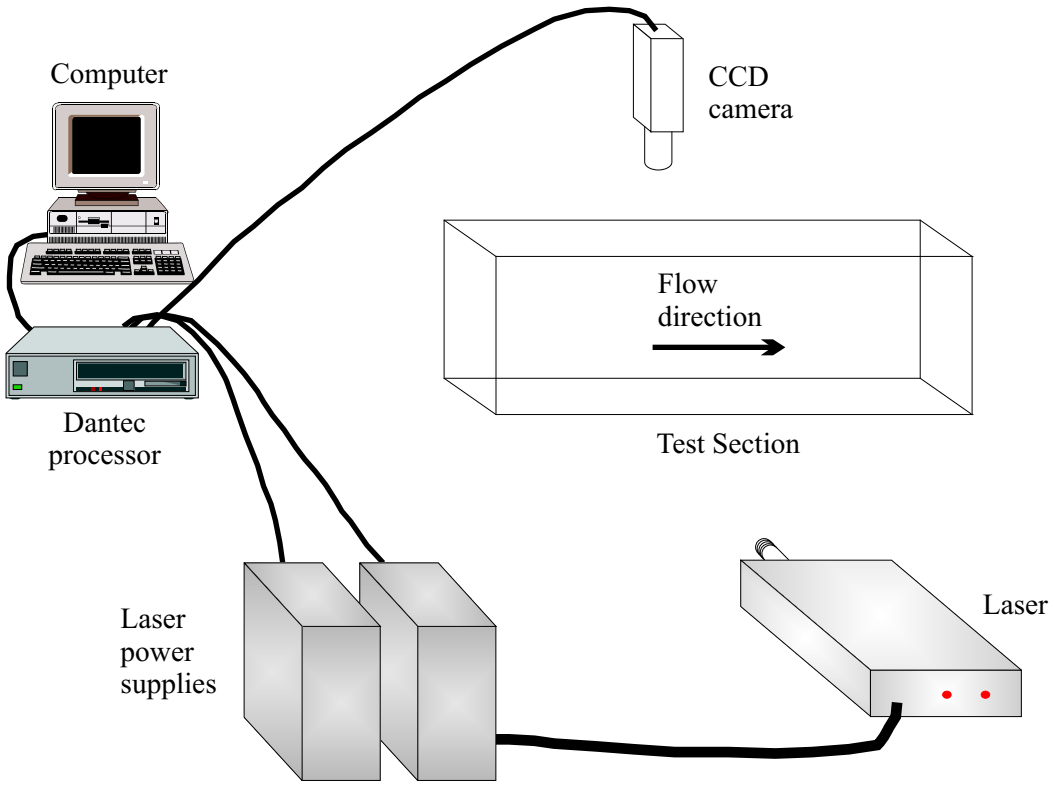

Figure 4.6: PIV Hardware Setup

importance here was the laser sheet thickness. For all experiments, the light sheet thickness was set between 2 and $3mm$.

4.5.2 CCD Camera

The recording device used in the PIV system was a Kodak Megaplus ES1.0 CCD camera with a frame resolution of 1008 by 1018 pixels. The Kodak Megaplus was capable of achieving minimum time separations of $1\mu s$ [35]. The only two user adjustments were the zoom and focus of the lens installed on the camera. The zoom could be adjusted to vary the overall size of the area photographed by the camera, while the focus was used to achieve sharp images of the measurement plane.

4.5.3 Processing Unit

A processing unit was required to synchronize the laser and camera to ensure that the camera captured an image at the same instant that a laser burst was emitted. The processor used in this study was a Dantec 1100 Flow Processor. Through this processor (and its software), the user could adjust all other necessary parameters such as the time separation (Δt), the magnification factor M, and the options for image cross correlation, such as the interrogation area size and overlap.

At this point, the reader should have enough theory and background on both wind tunnels and PIV. The following chapters discuss the flow measurements performed in the wind tunnel using the PIV system described above.

Chapter 5

Wind Tunnel Flow Validation

5.1 Introduction

Previous chapters have reviewed the wind tunnel and measurement technique used in this study. The remaining chapters describe the flow measurements performed in the wind tunnel using particle image velocimetry (PIV).

Before any useful measurements can be made in a new wind tunnel, it is necessary to examine the flow in the empty test section. Parameters such as flow uniformity and turbulence levels in the test section should be kept within reasonable levels to provide meaningful results on test models. The first calibration test performed on the wind tunnel in this study was a wind speed calibration test.

5.2 Mean Wind Speed Calibration

5.2.1 Objective

The main objective of this experiment was to generate a mean wind speed calibration curve in the test section. Since the fan was driven with a variable frequency drive, it was necessary to know

the resulting mean wind speed in the test section at different frequency settings of the controller. The calibration curve generated in this way should only be used as an approximate method for obtaining a desired test speed, due to the fact that the experiment was conducted with no model in the test section. The placement of a model in the test section would typically induce higher local velocities around the model due to the flow obstruction. The base wind speed calibration curve can therefore be used as a starting point, however, the true test speed must be measured and fine tuned in the vicinity of the model.

5.2.2 Experimental Setup

For this particular test, a vertically oriented measurement area was located along the centreline of the test section ($Y = 76.2\ mm$), with its bottom left hand corner located at $(X, Z) = (191.9, 68.3)mm$ (Figure 5.1). The laser was placed beneath the test section while the camera was placed to one side of the test section as shown in Figure 5.1. With a physical image size of $84.4mm$ x $85.3mm$ and a CCD array of 1008 x 1018 pixels, the resulting image resolution was 0.084 mm/pixel.

5.2.3 Sample Sizing

Before collecting PIV measurements, it was necessary to determine how many image pairs would be sufficient in determining the desired parameters such as mean velocity and turbulent kinetic energy. In an initial PIV experiment in the empty section, 500 image pairs were collected, and the average velocity in a small area was plotted against $1/n$, where n was the sample size (number of image pairs) used. In Figure 5.2, sample sizes of 50, 100, 200, 300, 400, and 500 images pairs were used in the determination of the plotted velocities. From 1/n = 0.02 to 0.005 (50 to 200 image pairs, respectively) the average measured velocity differed by 0.11%. However, from 200 to 500 image pairs (0.005 to 0.002 in Figure 5.2), the measured velocities only varied by a maximum of 0.019%. Based on these results, it appeared that a sample size larger than 200 image pairs would provide stabilized velocity measurements, with a variation of less than 0.02%. Average values of

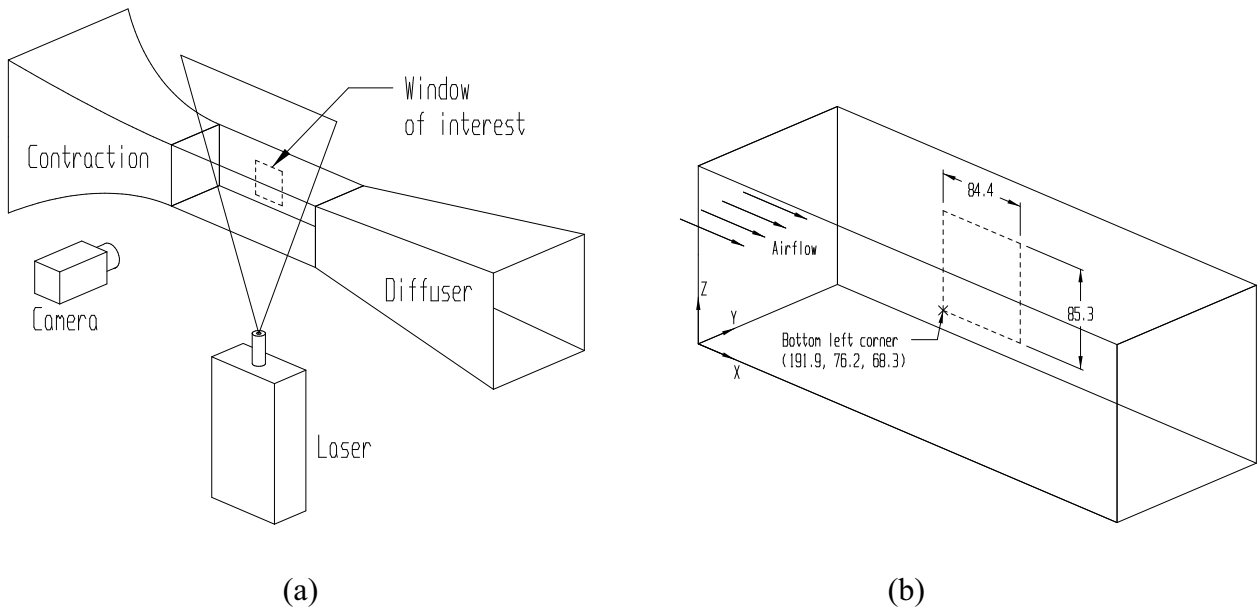

Figure 5.1: Experimental setup and measurement window for wind speed calibration test (all dimensions in mm)

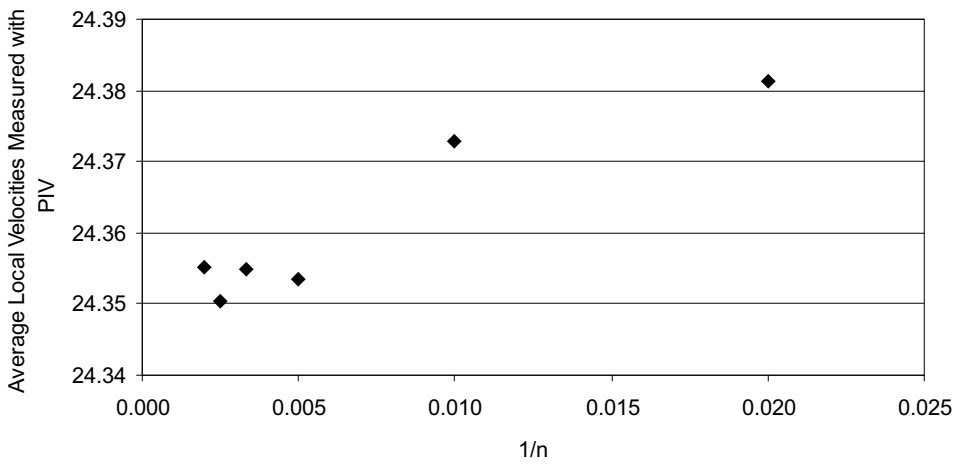

Figure 5.2: Average velocity values as a function of the sample size, n

turbulent kinetic energy followed the same trend, with the variation dropping to less than 2.5% above a sample size of 200 image pairs.

5.2.4 Experimental Uncertainty

In Table 5.1, the various sources of error in PIV (outlined in Section 4.3.4) are estimated based on the velocities measured in this chapter. The basis for each estimation is included in the rightmost column as many error sources were considered negligible.

Based on these estimates, the total error in the measured displacements was $0.008mm$ (given a typical measurement area of $80mm$ x $80mm$). In terms of velocities, the error ranged from 1.5% to 2.3%, depending on the average velocities measured.

Error Source	Error Estimate	Total Error [mm]	Description
Image Recording	Negligible		Amount of electrical noise not known
Contrast	Negligible		Level of contrast was high in all images (above 100 counts of contrast)
Particle Number Density	0.0175 pixels	4.07E-05	Taken as lowest error value from Figure 4.6 of Huang *et al.* [49] since all interrogation areas contained at least 50 particles
Loss of Pairs Due to Out-of-Plane Motion	Negligible		Maximum out-of-plane velocities measured were 0.3 m/s, resulting in a displacment of only 0.003mm compared to a 3mm sheet (factor of 1000)
Parallax	0.00151 pixels	5.37E-06	Calculated from the estimates of Sinha [51] using a 80mm x 80mm measurement area, 0.3 m/s maximum out-of-plane displacement, and a distance of 508mm from the camera lens to the measurement plane
Tracking Error	Negligible		Mineral oil was calculated to have a response time of 0.00000009 (*i.e.* time lag with respect to air)
Acceleration Errors	Negligible		Acceleration unknown but assumed negligible since the empty test section flow was expected to be extremely uniform and steady
Velocity Gradient Error	Negligible		Also assumed negligible here due to the test section being empty
Particle Image Size	Negligible		Negligible since the particles were assumed to be smaller than 1 pixel, resulting in cross correlation of entire smoke particle-clusters
Sub-pixel Interpolation	0.10 pixels	7.95E-03	Based on the theoretical and simulation results of Westerweel [55]

Table 5.1: Estimation of the errors in the PIV measurements collected in the test section

5.2.5 Results

In order to generate a fan/speed calibration curve, 50 PIV image pairs were collected in the measurement area at eleven different values of drive controller frequency ranging from 5.83 Hz to 60 Hz (full load). Based on the results of Section 5.2.3, a sample size of only 50 image pairs could differ by as much as 0.11% from the expected true value. This amount of variation was acceptable in this case however, since the main objective here was only to obtain a rough estimate of the velocities at each controller frequnecy.

Since the test section wind speed changed with every frequency, it was necessary to first determine the appropriate time separation between image pairs in order to ensure proper cross correlation. Table 5.2 shows the eleven frequency values chosen along with the time separation used in each case. These frequencies are converted to a corresponding fan rotational speed in the second column from the left. The average velocities in the rightmost column were calculated by averaging the velocity values in the free stream of the test section (well clear of the wall boundary layer).

The images collected were processed using interrogation areas of 32 x 32 pixels ($2.7mm$ x $2.7mm$),

Controller Frequency [Hz]	Fan Speed [rpm]	Time Separation [μs]	Wind Speed [m/s]
5.83	350	100	3.29
11.67	700	60	7.31
17.50	1050	35	11.75
23.33	1400	30	15.95
29.17	1750	25	19.97
35.00	2100	20	24.67
40.83	2450	18	28.20
46.67	2800	15	32.84
52.50	3150	12	36.04
57.50	3450	8	41.10
60.00	3600	7	42.72

Table 5.2: Controller frequencies used for wind speed calibration

with 50% overlap. This resulted in vector maps containing 3844 velocities (62 x 62) for each speed. Figure 5.3 is a picture of one such seeded image collected in this experiment (at 17.5 Hz).

Figure 5.4 is a plot of the results in Table 5.2. The secondary Y-axis represents the corresponding fan rotational speed and was determined from the controller frequency. The calibration curve was approximated with the following linear relationship:

$$(\text{controller frequency, Hz}) = 1.3805 \times (\text{desired wind speed, m/s}) + 1.4322 \tag{5.1}$$

Although the calibration curve is nearly linear in this case, it cannot always be expected since flow losses may increase with the square or cube of the velocity. Equation 5.1 was used as a starting point in finding the appropriate wind speed for all the remaining measurements in this study.

5.3 Corner Flow Validation

5.3.1 Objective

Apart from the test section, the wind tunnel used for this study was fabricated with one other area of optical access. Two acrylic panels were installed on the top and side wall, just downstream

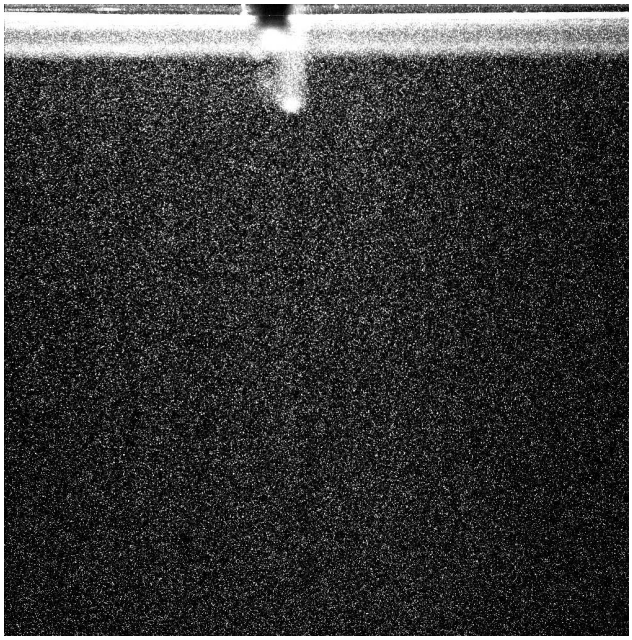

Figure 5.3: Sample PIV image from wind speed calibration measurements (approximate size, $85mm$ x $85mm$, smoke particles in air)

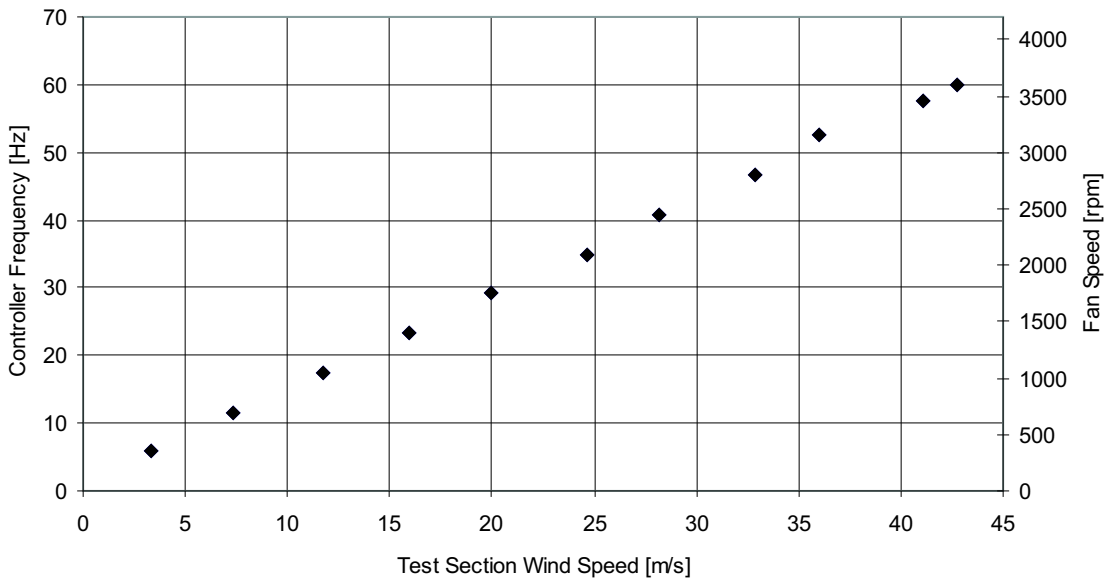

Figure 5.4: Wind speed calibration curve

of corner 2 (settling chamber). This allowed for PIV measurements to be performed on the flow exiting corner 2, upstream of the contraction section.

The objective of this experiment was to investigate the effectiveness of the turning vanes installed in corner 2. The performance of the turning vanes could be evaluated by looking at the uniformity and alignment of the exiting velocity profile. The measurements performed in this area would also define the true inlet conditions for the contraction and test section.

5.3.2 Experimental Setup

For the turning vane measurements, the PIV system was set up to utilize a horizontal light sheet with the camera placed above the wind tunnel, looking down (Figure 5.5). The light sheet was placed at the mid-height of the wind tunnel cross section (190.5mm from both the top and bottom walls). Due to the width of the wind tunnel cross section at that point (381mm), four PIV measurement windows were used. Each window measured 100mm x 101mm, giving a resolution of 0.099 mm/pixel. At a test section speed of 25 m/s, 250 image pairs were collected in each of the four windows spanning the wind tunnel width. The image pairs were processed using interrogation areas of 32 x 32 pixels (3.17mm x 3.17mm) and 50% overlap, resulting in 3,844 (62 x 62) vectors.

The estimated errors in these PIV measurements are tabulated in Table 5.3 and resulted in a total error of 0.01mm (displacement), or 2.3% (velocities).

5.3.3 Results

5.3.4 Mean Velocities

Figure 5.6 is a contour plot of the longitudinal (X-direction) velocities measured in the four PIV measurement windows (given in m/s). A significant amount of variation was observed in the velocity profile, ranging from 1.8 m/s to 4.9 m/s. The highest velocities were located near the inner and outer walls, while the lowest velocities were seen in a region to the left of the

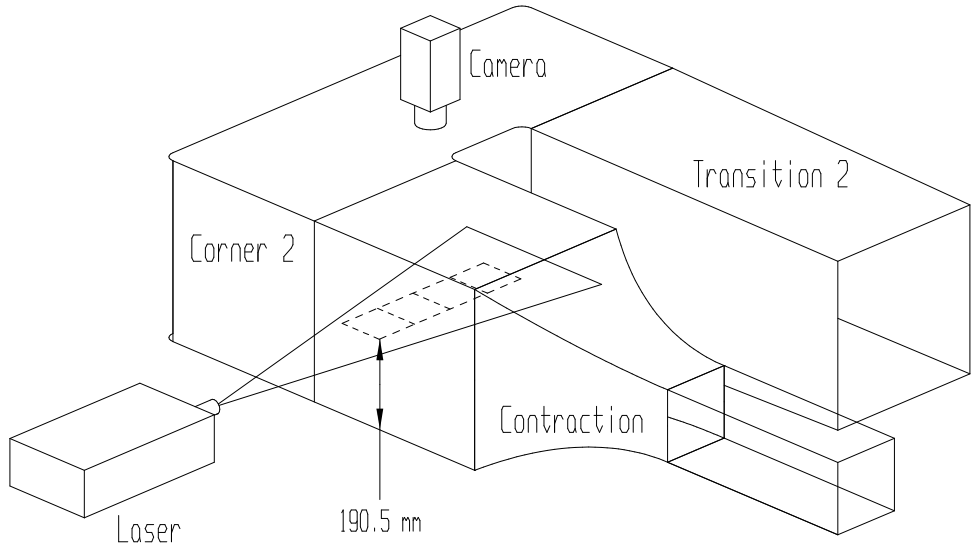

Figure 5.5: Experimental setup used for turning vane measurements

Error Source	Error Estimate	Total Error [mm]	Description
Image Recording	Negligible		Amount of electrical noise not known
Contrast	Negligible		Level of contrast was high in all images (above 100 counts of contrast)
Particle Number Density	0.0175 pixels	7.75E-05	Taken as lowest error value from Figure 4.6 of Huang *et al.* [49] since all interrogation areas contained at least 50 particles
Loss of Pairs Due to Out-of-Plane Motion	Negligible		Maximum out-of-plane velocities measured were 0.175 m/s, resulting in a displacment of only 0.003mm compared to a 3mm sheet (factor of 1000)
Parallax	2.49E-05 pixels	1.11E-07	Calculated from the estimates of Sinha [51] using a 100mm x 100mm measurement area, 0.175 m/s maximum out-of-plane displacement, and a distance of 620mm from the camera lens to the measurement plane
Tracking Error	Negligible		Mineral oil was calculated to have a response time of 0.00000009 (*i.e.* time lag with respect to air)
Acceleration Errors	Negligible		Acceleration unknown but assumed negligible since the empty test section flow was expected to be extremely uniform and steady
Velocity Gradient Error	Negligible		Also assumed negligible here due to the test section being empty
Particle Image Size	Negligible		Negligible since the particles were assumed to be smaller than 1 pixel, resulting in cross correlation of entire smoke particle-clusters
Sub-pixel Interpolation	0.10 pixels	9.90E-03	Based on the theoretical and simulation results of Westerweel [55]

Table 5.3: Estimation of the errors in the PIV measurements collected downstream of the corner 2 turning vanes

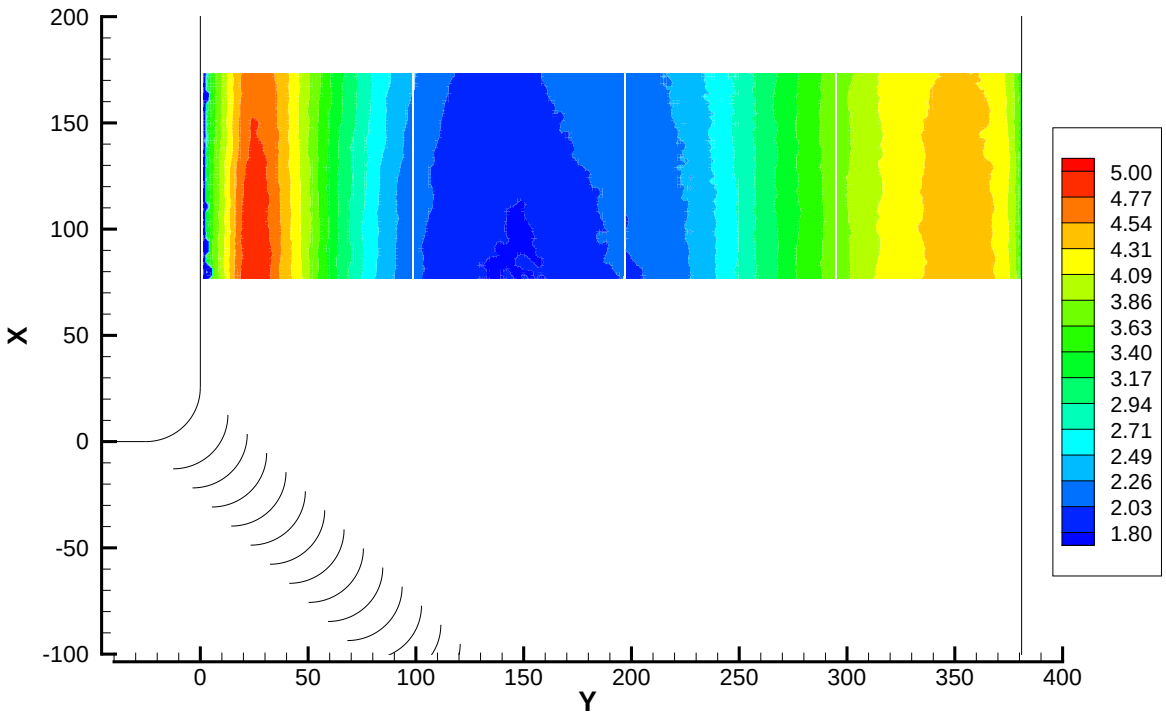

Figure 5.6: Longitudinal velocities measured at the exit of corner 2 (given in m/s) Note: All axis dimensions in mm

centreline ($Y \approx 150mm$). This skewed velocity profile was most likely caused by the fan section. The motor (which directly drove the fan) created a large flow blockage in the fan section, which forced all the air flow to pass through the ring of area between the casing diameter and the outer diameter of the motor. Since the area of measurement (exit of corner 2) was located less than 2 m downstream of the fan, it was reasonable to assume that these fan effects had not been fully dissipated. Although the screen and contraction section largely eliminated this variation in velocity before the test section, further improvements in the flow quality could be acheived with a longer settling chamber and/or individual adjustment of each vane in corners 1 and 2 to direct higher velocity flow towards the centre.

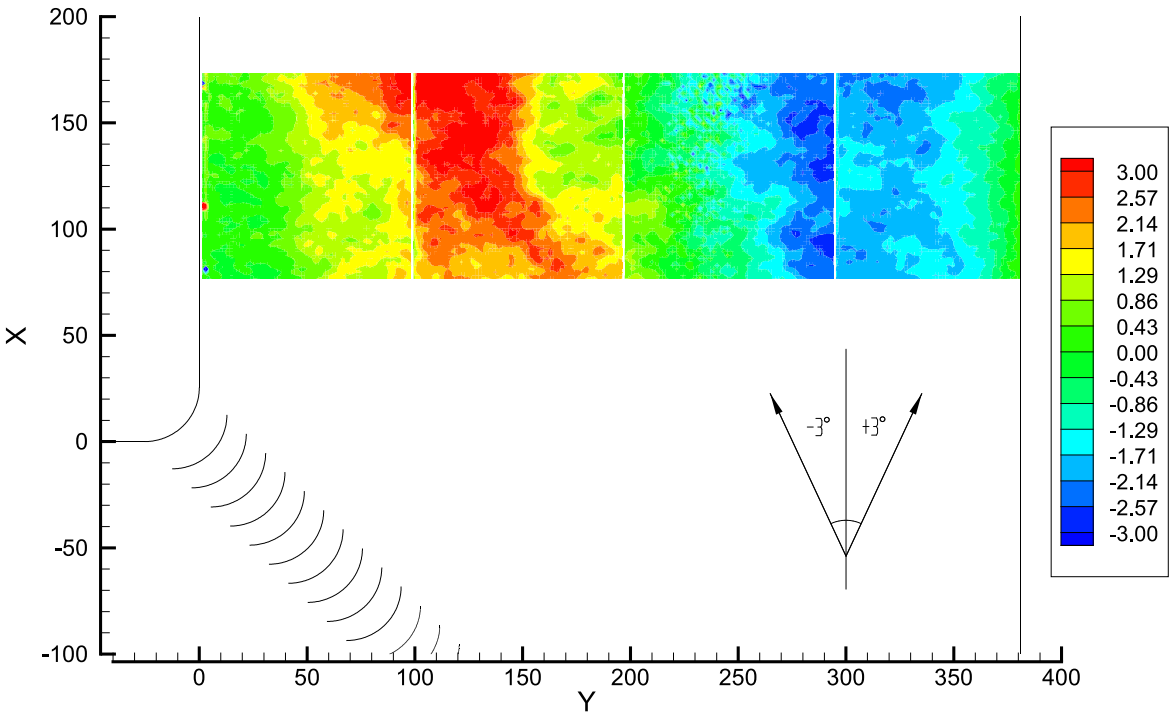

Figure 5.7: Transverse velocities measured at the exit of corner 2 (presented as angles of misalignment in degrees) Note: All axis dimensions in mm

Figure 5.7 is a plot of the mean transverse (Y-direction) velocities in terms of the angle formed with the corresponding X-direction velocity. The degree of misalignment of the flow varied from -3° to 3° with respect to the tunnel walls (Y-axis). Two main streams of flow were observed. The region between $70 < X < 160$ contained a stream of flow directed (to the right) towards the center of the wind tunnel. On the right side, at $275 < X < 340$, a similar stream was seen, also flowing towards the center of the tunnel (to the left). This phenomenon was most likely an effect of the velocity profile seen in Figure 5.6. As the quicker flow along the sides decelerates, it tends to flow towards the center by continuity.

The degree of non-uniformity and misalignment in the flow exiting corner 2 was expected due to

the relatively short settling distance from the fan section and corners 1 and 2. However, it was also expected that the honeycomb section (located downstream of the measurement area) would be successful in reducing the 3° of misalignment to an acceptable level in the test section. In addition, the screen section (located immediately downstream of the honeycomb section) was expected to correct the non-uniformity in the velocity profile seen in Figure 5.6. The characterization of the flow in the test section was necessary to verify this behaviour.

5.4 Test Section Flow Validation - Vertical Plane

5.4.1 Objective

To validate the quality of the air flow in the test section, it was necessary to observe the flow in greater detail, along both vertical and horizontal planes. The objective here was to capture a larger number of images so that statistical properties such as turbulent kinetic energy and turbulence intensity could be quantified using a vertically oriented measurement area. In addition, a full velocity profile (spanning from the bottom to the top wall) was desired so that any non-uniformity in the flow could be addressed.

5.4.2 Experimental Setup

Two PIV measurement areas were required in order to capture a velocity profile spanning the entire height of the test section. The two measurement areas were located at the midpoint ($Y = 76\ mm$) of the test section width (Figure 5.8(b)). Windows A and B both measured $83.1mm$ x $83.9mm$, giving a resolution of 0.082 mm/pixel. The camera and laser were oriented in the same way as for the wind speed calibration measurements (see Figure 5.8(a)).

Flow measurements were performed in windows A and B at three different speeds in order to observe the wind tunnel behaviour near the upper and lower limits of the fan. The three controller frequencies chosen were 15.24, 35.95, and 56.65 Hz, representing approximately 10, 25, and 40 m/s in the test section. Each window was tested at all three speeds before proceeding to the next

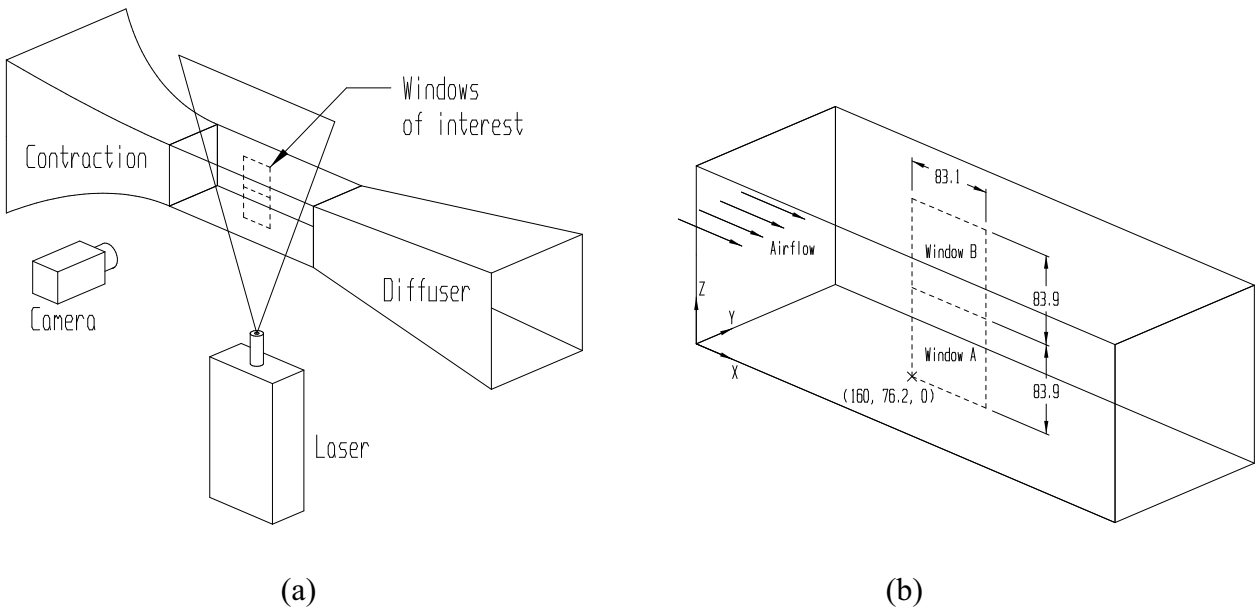

Figure 5.8: (a)Experimental setup for vertical plane measurements in the test section (b)size and location of measurement area (all dimensions in mm)

window since it was much easier to change the wind speed as opposed to changing the camera and laser setup each time. Each measurement window required calibration only once using this method.

Figure 5.9 shows a typical image collected from window A using PIV. It is important to note that even though the camera had been focused correctly on the measurement plane, objects far outside that plane could still be captured. In Figure 5.9, one of the screws used to fasten the test section walls was captured in the PIV images taken at that location. The presence of the screw in the images resulted in erroneous velocity data in that region. One possible solution to this problem was to coat the screw with a non-reflective, flat black paint. However, light would still be reflected from the surface of the threads cut into each screw hole in the acrylic. This problem was judged to be acceptable for two reasons. First, the flow in an empty test section was assumed to be very uniform so that any small area could be substituted with the values around it. Second, it was unlikely that measurements would ever be made near the wall when a model was inserted in the test section.

For both windows A and B, and at each speed, 500 image pairs were collected and averaged. Each image pair was processed using interrogation areas of 32 x 32 pixels ($2.6mm$ x $2.6mm$) with 50% overlap. This gave vector maps containing 3,844 vectors (62 x 62). From the 500 image pairs collected from each of the six tests, mean velocities (in the X and Z directions) and turbulent kinetic energy values were calculated. For simplicity, the results of windows A and B were combined and presented as one area of interest.

Based on the estimates in Table 5.1, errors in the measured velocities were determined to be 2.3%, 1.6%, and 2.0% at 10, 25, and 40 m/s, respectively. Section 4.3.4 gives a description of each error source.

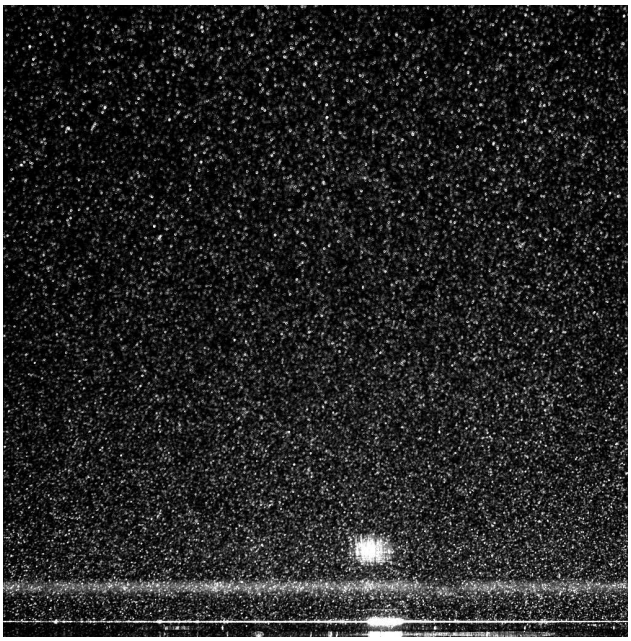

Figure 5.9: Sample PIV image from the test section in the vertical plane (approximate size, $85mm$ x $85mm$, smoke particles in air)

5.4.3 Results

Mean Velocities

Figure 5.10 presents the mean velocities (averaged from 500 image pairs) measured at the three test speeds. For clarity, only a small fraction of the 7,688 vectors collected are shown. As expected, a uniform flow was observed from left to right with a small boundary layer formed near the upper and lower walls. However, more detail was required in order to assess the quality of the flow for experimental purposes. Three flow characteristics were chosen as the best indicators of flow quality:

1. The maximum longitudinal (X-direction) variation in velocity;
2. The transverse (Y and Z direction) variation in velocity (or flow angle variation); and,
3. The levels of turbulent kinetic energy.

Contour plots showing the longitudinal velocities (m/s) at each of the three test speeds are presented in Figure 5.11. At 10 m/s, the maximum variation in longitudinal velocity was within 0.6% of the mean, with the bulk of that variation appearing in a small core near the upper wall. For the two higher speeds, a recurring flow pattern was observed. A core of lower velocities was found at the centre of the test section, increasing steadily towards the upper and lower walls. The maximum variation in velocity was higher, approximately 1.5% and 3.25% at 25 m/s and 40 m/s, respectively. The effect of the fastening screw mentioned in Section 5.4.2 is seen in the plots as an area of erroneous data centred at $(X, Z) = (210, 9)$ (Figure 5.9).

In Figure 5.12, the transverse velocities are plotted in terms of the angle they form with the corresponding U (X-direction) velocity. For example, a contour value of -0.15 indicates that the flow in that area is pointed downwards at an angle of 0.15^o, while a value of 0° is perfectly aligned with the test section wall. Pope *et al.* [2] suggest that this variation should be kept to within $\pm 0.20^o$. For comparison against this criteria, the limits of the contour levels in Figure 5.12 were set to $+0.20^o$ and -0.20^o. Therefore, any areas in blue or red indicate regions where the flow approached 0.20^o of misalignment.

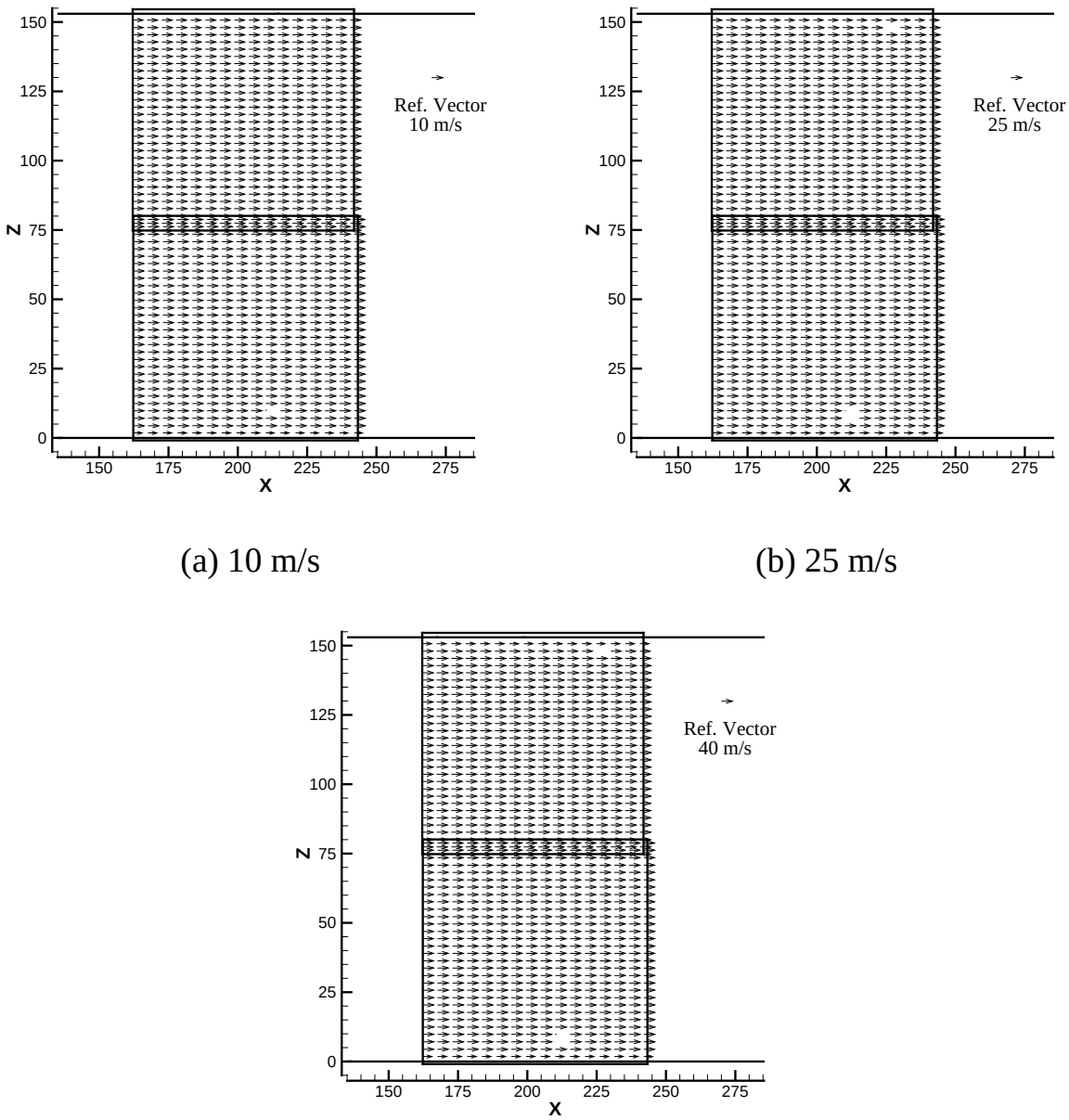

(a) 10 m/s

(b) 25 m/s

(c) 40 m/s

Figure 5.10: Mean velocities in the test section (vertical plane) (a) 10 m/s (b) 25 m/s (c) 40 m/s Note: All axis dimensions in mm

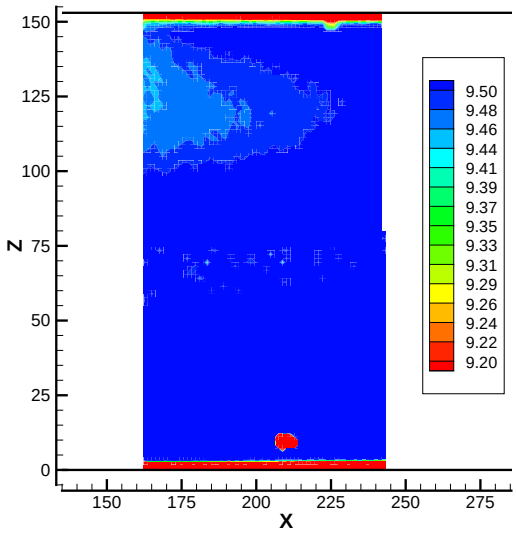

(a) 10 m/s

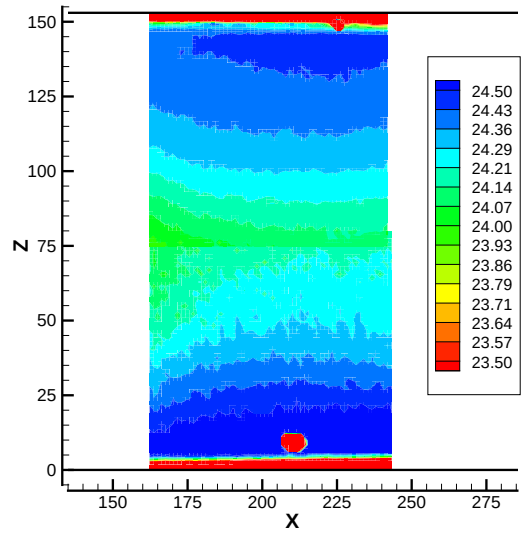

(b) 25 m/s

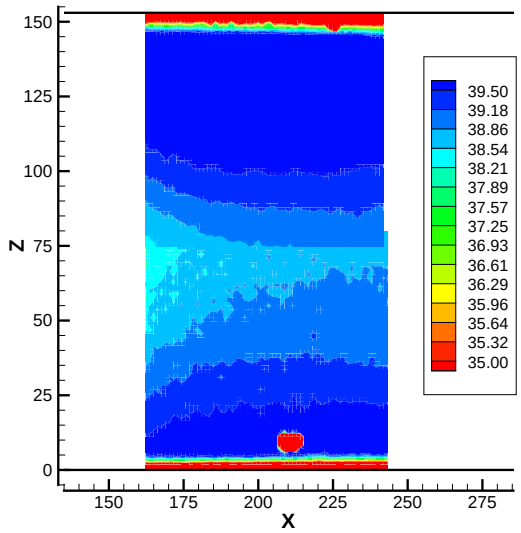

(c) 40 m/s

Figure 5.11: Longitudinal velocities measured in the vertical plane (given in m/s) (a) 10 m/s (b) 25 m/s (c) 40 m/s Note: All axis dimensions in mm

At all three test speeds in the vertical plane, a repeating pattern was observed in the transverse velocities. This trend was observed in the areas near the upper and lower test section walls, where the flow was directed towards the centreline of the test section. For example, at 10 m/s, the flow located between $10 < Y < 40$ was directed upwards at an angle of 0.20^o. Along the top wall, at $120 < Y < 145$, the flow was directed downwards at an angle of -0.20^o. This pattern was also observed at 25 m/s and 40 m/s. Some discontinuity was observed in the plots at the interface between the upper and lower measurement windows. It was important to note in this case that windows A and B were measured at different times, which could have led to some discontinuity when attempting to join the two windows together. Note that the flow angles plotted here represent Y-direction velocities in the range of 0 to 0.05 m/s. Therefore, despite the apparently large difference in contour colour, the actual discrepancy in the velocities was very small.

The variation in flow angle at all three speeds was considered to be satisfactory, since most regions fell within $\pm 0.20^o$ of misalignment. Any regions outside this limit were only misaligned by a further $\pm 0.05^o$ and therefore still considered to be acceptable.

Turbulence Levels

Figure 5.13 shows the levels of two-dimensional turbulent kinetic energy at the three test speeds. The turbulent kinetic energy, K_t, was calculated using the fluctuating components, u' and v', of the U and V velocities:

$$K_t = \frac{\overline{u'^2} + \overline{v'^2}}{2} \tag{5.2}$$

where K_t has the units m^2/s^2. The turbulence intensity was calculated as the ratio of u', v', or w' to the mean velocity, U [3]. According to Pankhurst [3], the dominant velocity (U) should used as the denominator in all three cases (*i.e.* u'/U, v'/U, and w'/U). At 10 m/s, K_t levels were in the range of 0.005 to 0.02 m^2/s^2. The average turbulence intensity level was calculated to be approximately 1.5% in the X-direction, and 0.5% in the Z-direction. At 25 m/s, the pattern observed in Figure 5.11(b) was seen. A core of higher K_t existed along the centre of the test section, dropping off from 0.18 to 0.02 m^2/s^2 towards the wall. Here, average turbulence

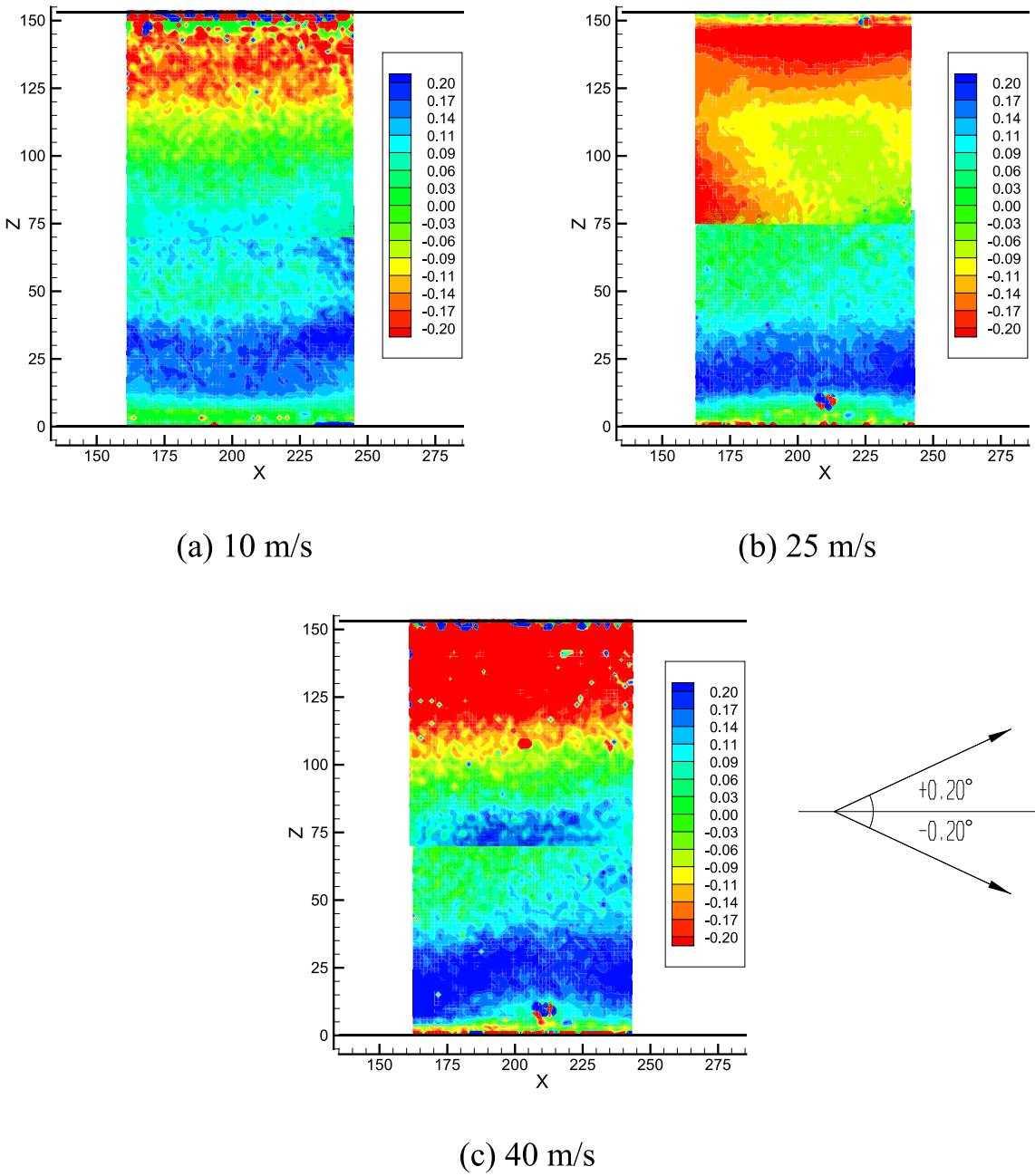

(a) 10 m/s

(b) 25 m/s

(c) 40 m/s

Figure 5.12: Transverse velocities measured in the vertical plane (presented as angles of misalignment in degrees) (a) 10 m/s (b) 25 m/s (c) 40 m/s Note: All axis dimensions in mm

intensities were calculated as 1.3% and 0.4% in the X and Z directions, respectively. A similar but less pronounced pattern was also observed at the third test speed, 40 m/s. K_t levels near the test section centreline were approximately 1.3 m^2/s^2, and fell to 0.25 m^2/s^2 near the upper wall. At this speed, the average turbulence intensity was approximately 2.6% in the X-direction, and 0.6% in the Z-direction.

5.5 Test Section Flow Validation - Horizontal Plane

5.5.1 Objective

After quantifying the flow characteristics of the test section in the vertical plane, it was necessary to evaluate these same characteristics in the horizontal plane to ensure consistent behaviour. The objectives of this experiment were therefore the same as for the vertical plane: to characterize the flow behaviour in the test section by investigating velocity profiles and turbulence levels using a horizontal measurement plane.

5.5.2 Experimental Setup

The experimental setup for this test was exactly the same as for the vertical plane tests, the only difference being that these measurements were taken along a horizontal plane ($X - Y$ plane) in the test section. This involved placing the camera below the test section and orienting the laser alongside of the test section as shown in Figure 5.14(a). Two measurement windows were needed in order to capture an entire velocity profile from the left to the right wall of the test section. The measurement windows A and B were located along the centreline ($Z = 76mm$) of the test section, beginning at $X = 160mm$ (along the test section length) (see Figure 5.14). Windows A and B measured 80.2mm x 81.0mm, giving a resolution of 0.080 mm/pixel.

The measurements were performed in the same way as for the vertical plane measurements. Three test speeds were used (10, 20, and 40 m/s), and 500 image pairs were collected in each case. Cross correlation was performed on the images using interrogation areas of 32 x 32 pixels

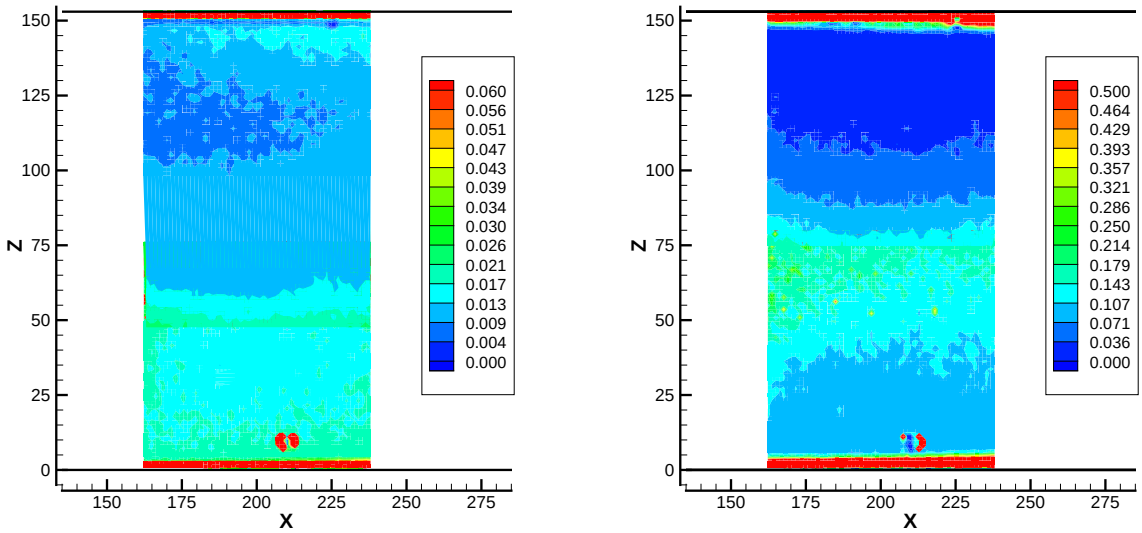

(a) 10 m/s (b) 25 m/s

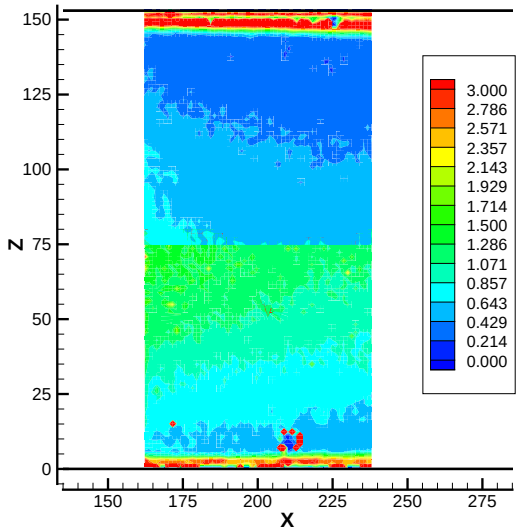

(c) 40 m/s

Figure 5.13: Turbulent kinetic energy levels in the test section (vertical plane) given in m^2/s^2 (a) 10 m/s (b) 25 m/s (c) 40 m/s Note: All axis dimensions in mm

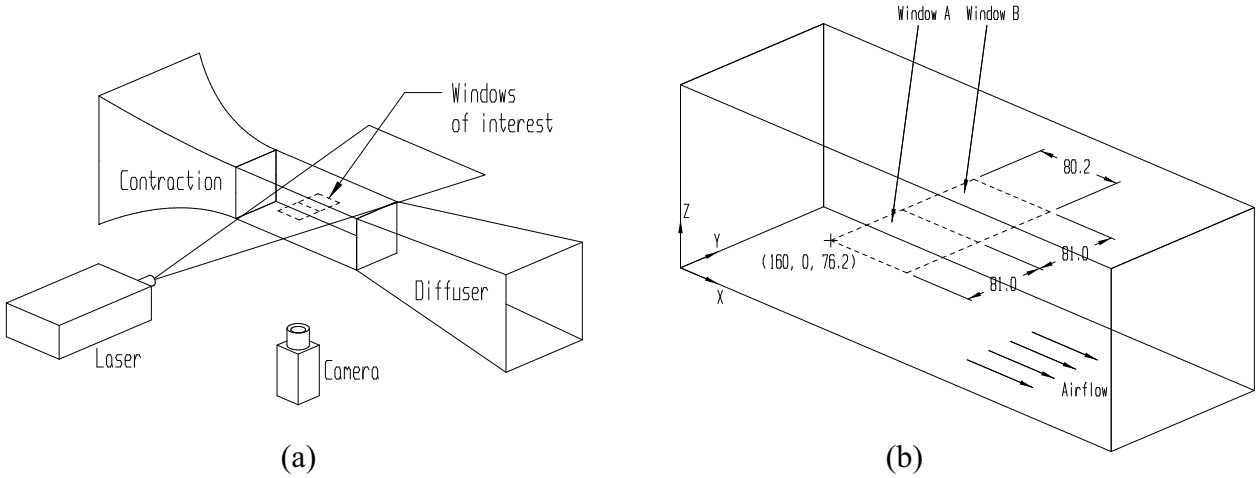

Figure 5.14: (a)Experimental setup for horizontal plane measurements in the test section (b)size and location of measurement area (all dimensions in mm)

and 50% overlap. Figure 5.15 shows a sample image in the horizontal plane captured with PIV. As can be seen, two fasteners were captured in each image, resulting in erroneous data in each of those regions. This was viewed as acceptable given the reasons outlined in Section 5.4.2.

The estimated errors for the PIV measurements in this experiment were the same as those determined for the wind speed calibration and test section vertical plane measurements. Velocity errors of 2.3%, 1.6%, and 2.0% were estimated for the three test speeds, 10, 25, and 40 m/s respectively. A breakdown of these error estimates can be found in Table 5.1.

5.5.3 Results

Mean Velocities

Figure 5.16 shows the mean velocity vectors measured in windows A and B (the full 7,688 vectors have once again not been plotted for clarity). Apart from the four areas of missing data (due to the fasteners captured in each image), the velocity profiles appear to be nearly identical to the

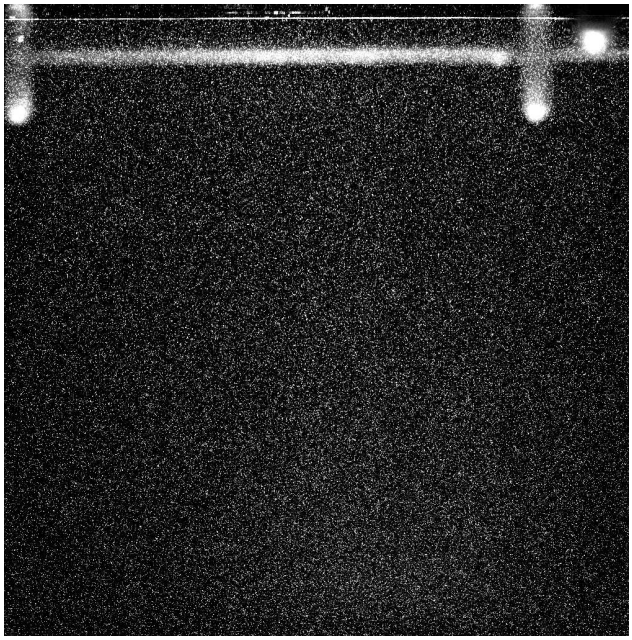

Figure 5.15: Sample PIV image from the test section in the horizontal plane (approximate size, $85mm$ x $85mm$, smoke particles in air)

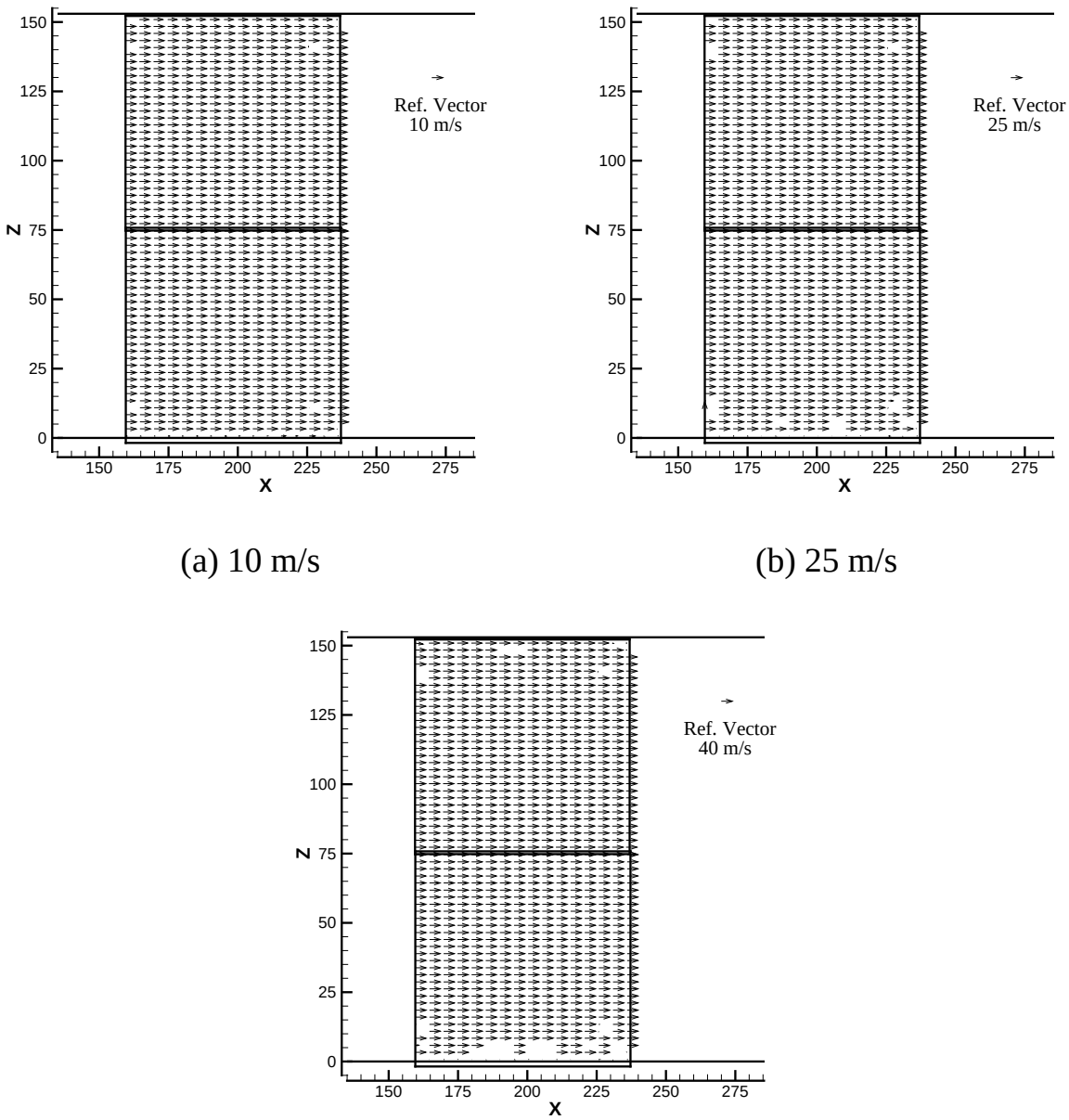

(a) 10 m/s

(b) 25 m/s

(c) 40 m/s

Figure 5.16: Mean velocities in the test section (horizontal plane) (a) 10 m/s (b) 25 m/s (c) 40 m/s Note: All axis dimensions in mm

vertical plane results, as should be the case. Contour plots of the longitudinal (X-direction) and transverse velocities are shown in Figures 5.17 and 5.18. At 10 m/s, the longitudinal velocity exhibited the same pattern as was seen in the vertical plane at 25 and 40 m/s. A core of lower velocities was observed at the centre of the test section while increasing slightly towards the left and right walls (top and bottom walls, respectively, in these figures). A maximum longitudinal velocity variation of 2.1% was observed here. The areas in red which were not within 3-4mm of the walls were considered to be erroneous data due to the light reflections from the fasteners. At 25 m/s, the maximum variation was only 0.6%, with the same flow pattern as 10 m/s. At 40 m/s, the expected flow pattern was observed (although with a slight mis-match between the upper and lower measurement windows) with a maximum longitudinal variation of 2.5%.

In Figure 5.18 the transverse velocities are again plotted as angles of misalignment, with the upper and lower limits of the contours representing $\pm 0.20^o$. At all three test speeds, the flow near the right (bottom) wall was directed towards the centreline of the test section. This pattern however, was not observed at the opposite side (left wall) of the test section. In fact, the results from 25 m/s and 40 m/s contained small regions of flow directed towards the left (top) wall. This was not expected after observing the flow behaviour in the vertical plane tests, but was considered to be satisfactory as the angles of misalignment were again within acceptable levels.

Turbulence Levels

Turbulent kinetic energy (Figure 5.19) and turbulence intensity levels were calculated in the same way as for the vertical plane measurements (Section 5.4.3). At 10 m/s, turbulent kinetic energy levels were in the range of 0.04 to 0.07 m^2/s^2, resulting in average turbulence intensities of 3% and 0.5% in the X and Y directions, respectively. Higher values were observed near the walls, as was also the case at 25 m/s, where turbulent kinetic energy levels reached 0.15 m^2/s^2 near the right wall. Average values of turbulence intensity were calculated to be approximately 1.1% and 0.4% in the X and Y directions. At 40 m/s, the turbulence levels were significantly higher, with values reaching 2.6 m^2/s^2. This resulted in average turbulence intensities of 4.0% and 0.5% in the X and Y directions, respectively.

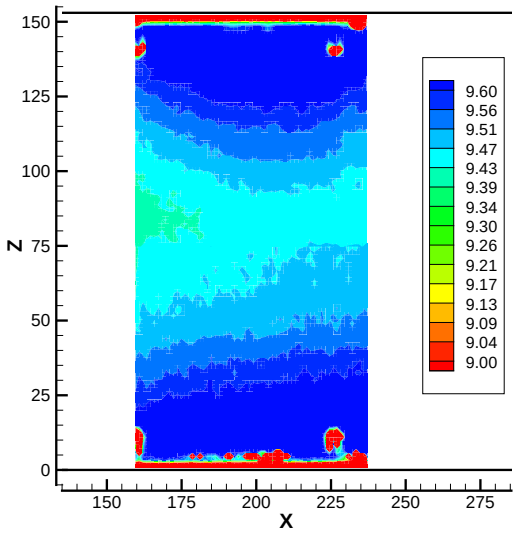

(a) 10 m/s

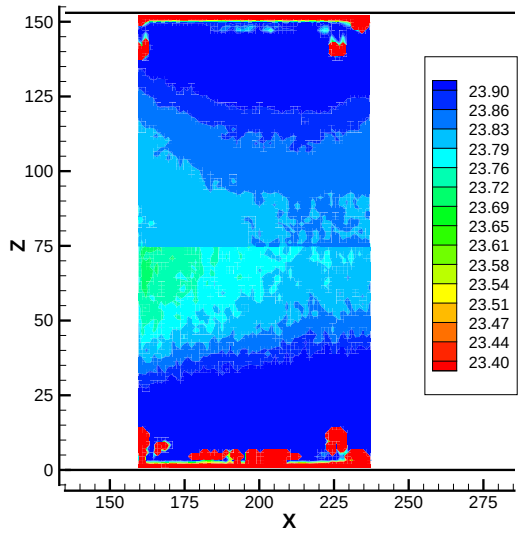

(b) 25 m/s

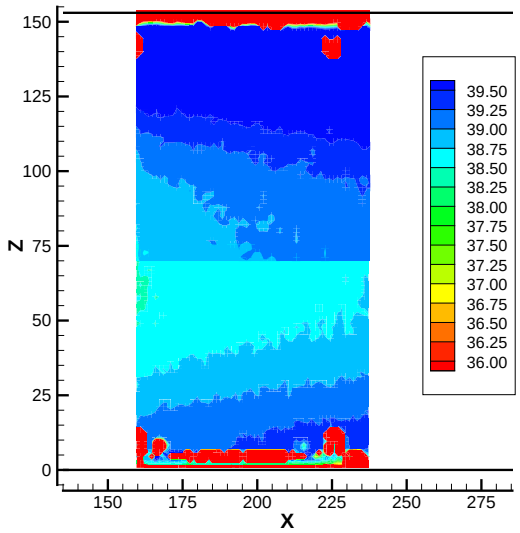

(c) 40 m/s

Figure 5.17: Longitudinal velocities measured in the horizontal plane (given in m/s) (a) 10 m/s (b) 25 m/s (c) 40 m/s Note: All axis dimensions in mm

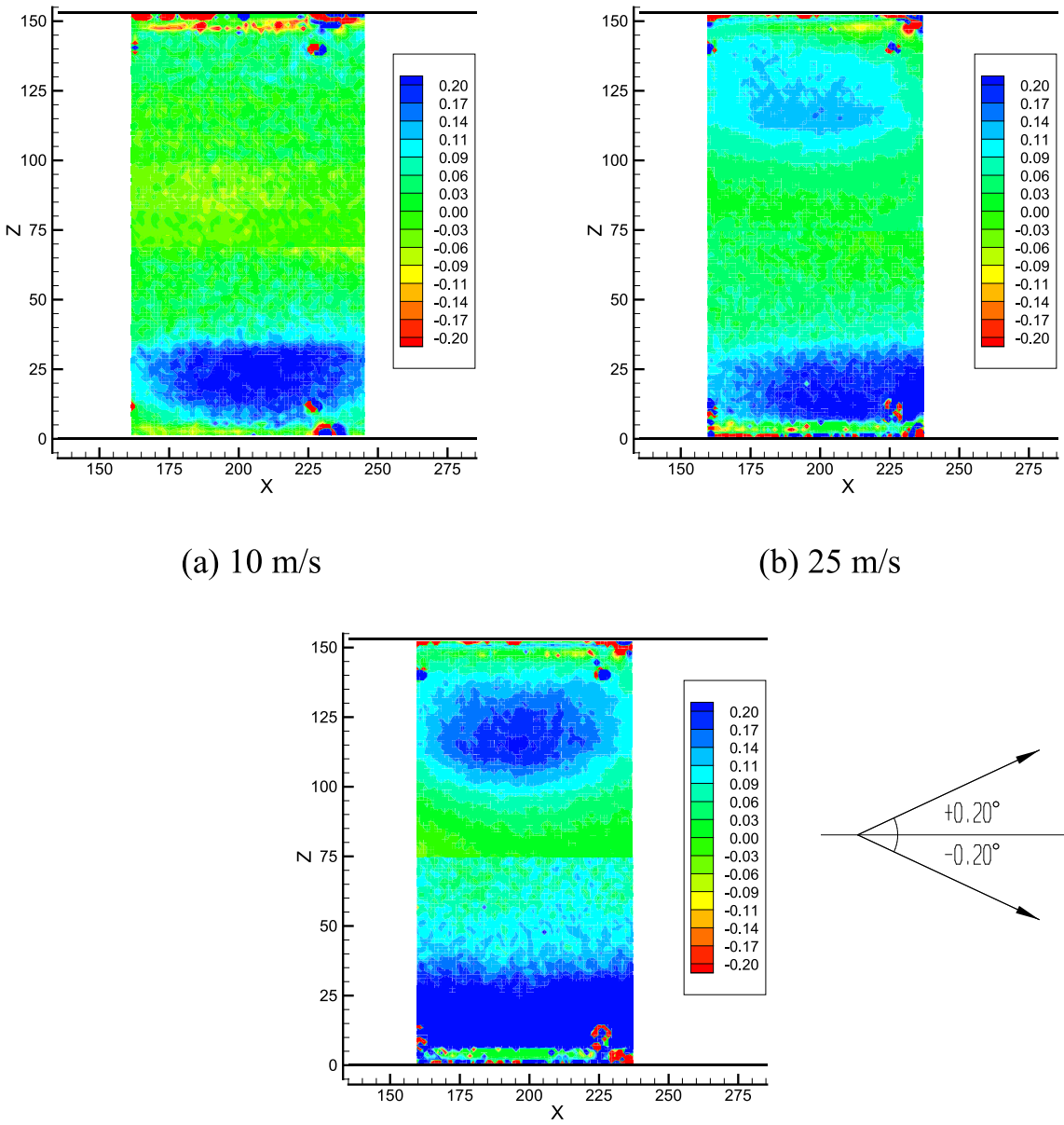

(a) 10 m/s

(b) 25 m/s

(c) 40 m/s

Figure 5.18: Transverse velocities measured in the horizontal plane (presented as angles of misalignment in degrees) (a) 10 m/s (b) 25 m/s (c) 40 m/s Note: All axis dimensions in mm

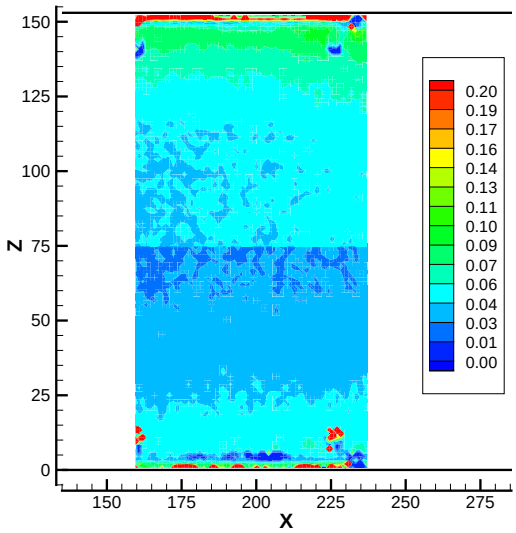

(a) 10 m/s

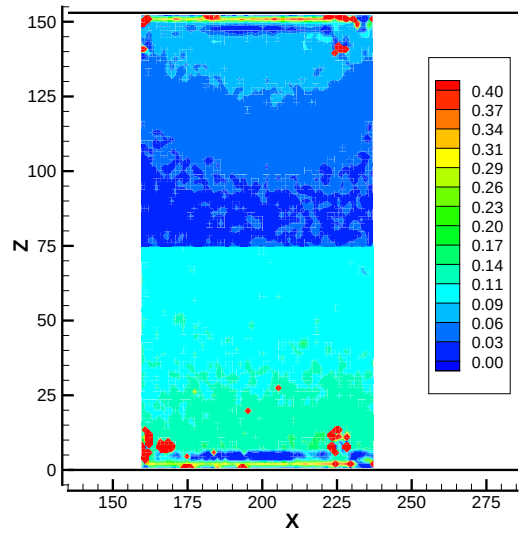

(b) 25 m/s

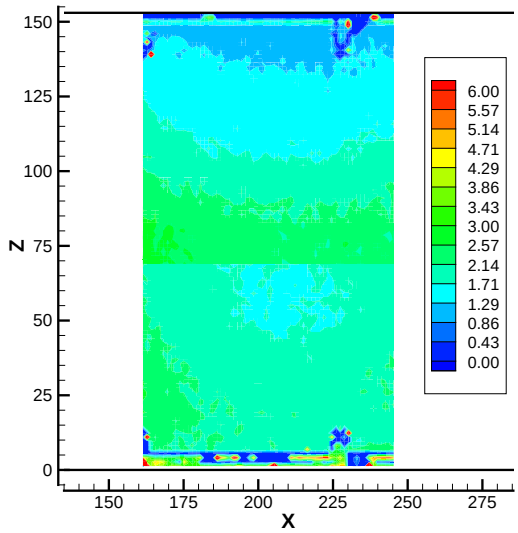

(c) 40 m/s

Figure 5.19: Turbulent kinetic energy levels in the test section (horizontal plane) given in m^2/s^2 (a) 10 m/s (b) 25 m/s (c) 40 m/s Note: All axis dimensions in mm

In summary, the measurements made in the vertical $(X - Z)$ plane, and the horizontal $(X - Y)$ plane revealed the flow characteristics in the test section of the wind tunnel used in this study. Longitudinal and transverse velocities were measured at mean air speeds of approximately 10, 25, and 40 m/s. The longitudinal (X-direction) velocities were found to vary by an average of 1.8% along any given velocity profile from one wall to the other. The flow was well aligned with the test section walls, deviating by no more than $\pm 0.20^o$ (as recommended by Pope *et al.* [2]) in most cases, with a few instances of greater misalignment not exceeding 0.30^o. Turbulence levels were calculated from the fluctuating velocity components. The average level of turbulent intensity was found to be 2.0% in the longitudinal direction, and 0.5% in both transverse directions (Y and Z).

5.6 Test Section Flow Validation - Wall Boundary Layer

5.6.1 Objective

In order to further characterize the flow quality in this wind tunnel, a third experiment was conducted in the empty test section. The objective for this experiment was to measure the shape and size of the boundary layer formed along the test section walls. Due to the length of the test section ($450mm$) it was reasonable to assume that a boundary layer could grow to a significant size before reaching its exit. This would have the effect of reducing the amount of usable area in the test section.

5.6.2 Experimental Setup

To reduce the amount of data collected, PIV measurements were performed only on one of the four test section walls. The bottom wall was chosen, requiring a vertical measurement plane (X-Z plane). The experimental setup was therefore identical to that used for the vertical plane measurements in the test section (Figure 5.8(a)). Figure 5.20 shows the measurement areas used in this experiment. Four measurement windows were chosen, located along the bottom wall of the test section, spaced approximately evenly along its length. Each window measured $52.5mm$ x $53mm$, giving a resolution of 0.052 mm/pixel. This gave higher resolution than the previous

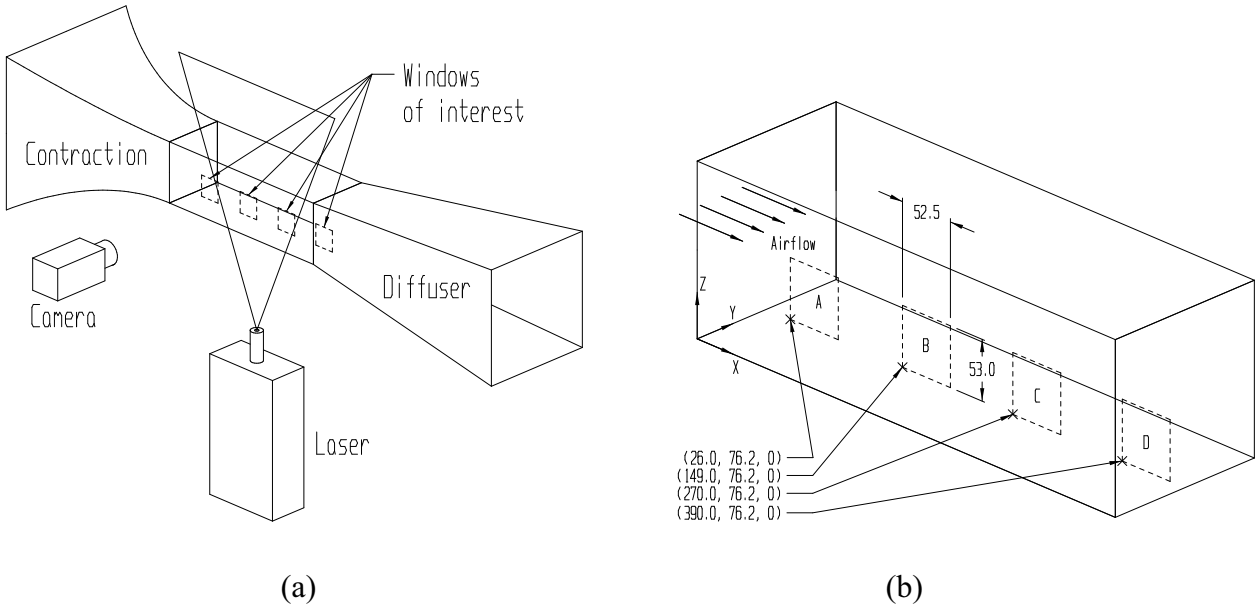

Figure 5.20: Size and location of measurement windows used for boundary layer experiments (all dimensions in mm)

vertical and horizontal plane measurements (which were approximately $82mm$ x $83mm$), in order to retrieve more velocity data close to the test section wall. To further increase the amount of data near the wall, different processing parameters were used. Interrogation areas of 32 x 32 pixels ($1.7mm$ x $1.7mm$) were used, but the overlap was increased to 75% in the vertical (Z) direction. The X-direction overlap was unchanged at 50%. By increasing the vertical overlap, the number of vectors in the vertical direction was doubled, resulting in vector maps containing 62 x 124 velocity vectors.

For each of the four windows, two test speeds were chosen; 20 m/s and 40 m/s, and 500 images were collected at each speed. At both speeds, the estimated error in the measured velocities with PIV was approximately 2.6% (Table 5.4).

Error Source	Error Estimate	Total Error [mm]	Description
Image Recording	Negligible		Amount of electrical noise not known
Contrast	Negligible		Level of contrast was high in all images (above 100 counts of contrast)
Particle Number Density	0.0175 pixels	6.26E-05	Taken as lowest error value from Figure 4.6 of Huang *et al.* [49] since all interrogation areas contained at least 50 particles
Loss of Pairs Due to Out-of-Plane Motion	Negligible		Maximum out-of-plane velocities measured were 0.3 m/s, resulting in a displacment of only 0.003mm compared to a 3mm sheet (factor of 1000)
Parallax	0.00457 pixels	1.07E-05	Calculated from the estimates of Sinha [51] using a 53mm x 53mm measurement area, 0.3 m/s maximum out-of-plane displacement, and a distance of 286mm from the camera lens to the measurement plane
Tracking Error	Negligible		Mineral oil was calculated to have a response time of 0.00000009 (*i.e.* time lag with respect to air)
Acceleration Errors	Negligible		Acceleration unknown but assumed negligible since the empty test section flow was expected to be extremely uniform and steady
Velocity Gradient Error	Negligible		Velocity gradients here may not be negligible, but this was compensated for with higher resolution and smaller interrogation areas
Particle Image Size	Negligible		Negligible since the particles were assumed to be smaller than 1 pixel, resulting in cross correlation of entire smoke particle-clusters
Sub-pixel Interpolation	0.10 pixels	5.20E-03	Based on the theoretical and simulation results of Westerweel [55]

Table 5.4: Estimation of the errors in the PIV measurements collected in the test section boundary layer

	A	B	C	D	E	F	G	H	Total Angle
20 m/s	1.50	1.67	2.00	2.45	3.22	4.00	5.20	6.14	0.64°
40 m/s	1.34	2.19	3.02	3.56	4.60	5.06	5.80	6.43	0.71°

Table 5.5: Height of the boundary layer at various locations along the test section (mm)

5.6.3 Results

Mean Velocities

Figures 5.21 and 5.22 are plots of the longitudinal (X-direction) velocities in each of the four measurement windows at 20 m/s and 40 m/s, respectively. With the air flowing from left to right, it could be seen that the boundary layer grew steadily in size further downstream along the test section. In order to better quantify the shape and size of the boundary layer, Table 5.5 shows the height of the boundary layer at the extremity of each measurement window at both speeds (points A through H in Figures 5.21 and 5.22). The reported height (given in mm) at each location was taken as the point at which the velocity fell below 97.5% of the mean flow. A slightly larger boundary layer was oberved at 40 m/s, however, this difference was quite small, in most cases $1mm$ or less. These heights gave a good indication as to the amount of useful area in the test section. For example, if a model was tested near the midpoint of the test section length, then one could assume that useful data would be obtainable as close as $4mm$ away from the wall. Assuming the boundary layer was similar in size on all four test section walls, then a $4mm$ boundary layer would leave 90% of the cross sectional area available for useful measurements. In the very worst measured case (point H in the test section at 40 m/s), 83.8% of the cross sectional area would still give flow that is within 97.5% of the mean velocity. The rightmost column in Table 5.5 shows the overall angle formed by the first and last points, indicating the slope at which the boundary layer grew. Again, there was only a small difference in angle between the two speeds, indicating that the shape and size of the boundary layer was not heavily dependent on speed.

It was interesting to note the contracting effects of the growing boundary layer in the test section. As the boundary layer grew, it left a smaller and smaller area for the main flow to pass through,

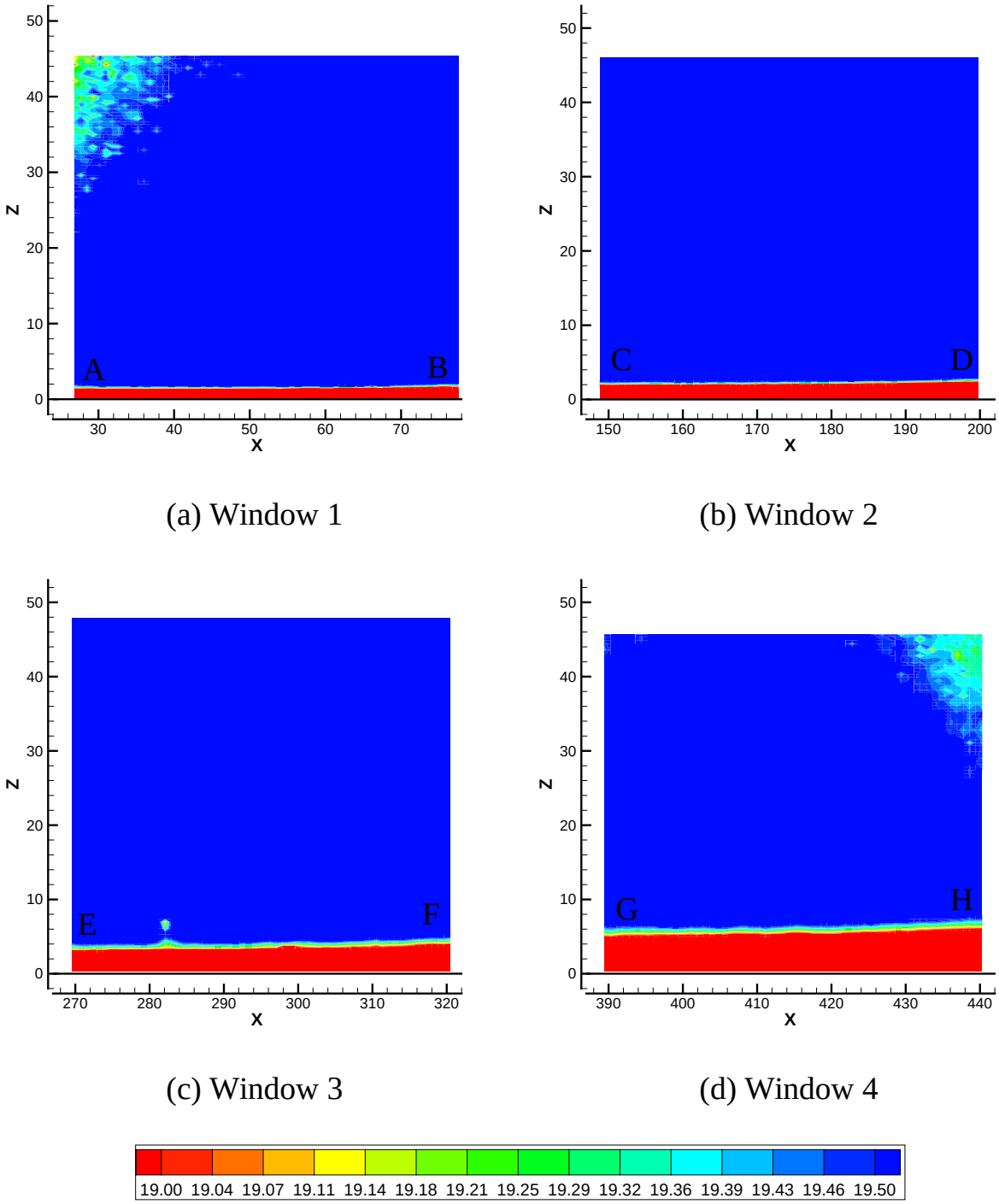

(a) Window 1

(b) Window 2

(c) Window 3

(d) Window 4

Figure 5.21: Longitudinal velocities collected along the test section wall at 20 m/s. Note: All plots in this figure follow the same contour legend shown above, all axis dimensions in mm

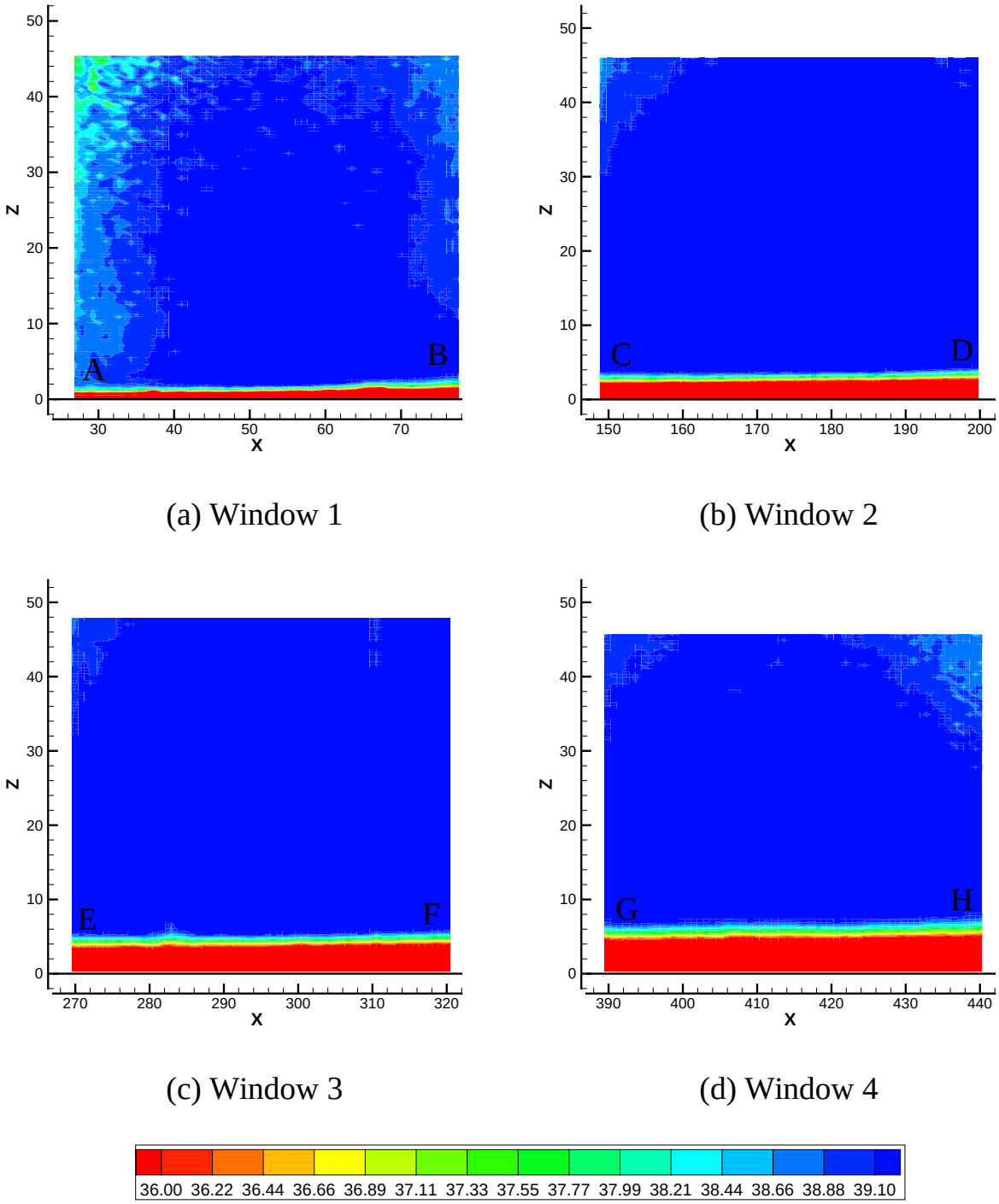

(a) Window 1

(b) Window 2

(c) Window 3

(d) Window 4

Figure 5.22: Longitudinal velocities collected along the test section wall at 40 m/s. Note: All plots in this figure follow the same contour legend shown above, all axis dimensions in mm

resulting in a slight acceleration of the flow along the length of the test section. On average, the velocity increased by 0.15 m/s from the first measurement window to the second. From the second to the third, a further 0.1 m/s increase in velocity was seen. From the third to the fourth window however, a decrease of 0.15 m/s was observed. This may be due to the decelerative effect of the diffuser propagating slightly upstream from its entrance. Due to this effect, model measurements should not be made beyond $X \approx 430mm$ (Figures 5.21 and 5.22, Window 4).

One method of correcting for the boundary layer growth in the test section is to incorporate a draft angle into the test section walls [2]. With the use of a moderate draft angle, the cross sectional area of the test section can be gradually increased, allowing for the thickening boundary layer while maintaining constant static pressure in the main flow outside of the boundary layer. Pope *et al.* [2] suggested a draft angle of 0.5^o in each test section wall, although little information was available. Based on the results of this section, this particular wind tunnel would benefit from a 0.7^o draft angle in order to accomodate the boundary layer growing at that approximate angle (Table 5.5). The use of this draft angle however, would have complicated the fabrication of the test section, and made it more difficult to distinguish transverse velocities with respect to the test section walls and it was therefore decided to utilize a conventional design with constant cross section.

5.6.4 Comparison of Boundary Layer Sizes with CFD Simulation Results

In Section 2.6 a CFD study was performed in order to determine the optimum contraction shape to be used in the wind tunnel. In the simulation, an outlet duct (representing the test section) was placed at the outlet of the contraction (Figure 2.13). With these results, it was possible to compare the boundary layer sizes as determined by CFX TASCflow to those found using PIV in the previous section.

In Figure 5.23 the general style of the plots in Figure 5.22 were reproduced, using the results of the CFD simulation. As in Section 5.6.3, the points A through H in Figure 5.23 represented the top of the boundary layer at the edge of each of the four plotted areas. Their heights (or distance from the test section wall) were determined as the point at which the X-direction velocity fell to

	A	B	C	D	E	F	G	H	Total Angle
PIV Results (40 m/s)	1.34	2.19	3.02	3.56	4.60	5.06	5.80	6.43	0.71°
CFD Results (40 m/s)	3.02	3.80	4.53	4.92	5.35	5.74	6.04	6.43	0.47°
% Difference	56%	42%	33%	28%	14%	12%	4%	0%	34%

Table 5.6: Comparison of the boundary layer size (mm) as determined by PIV measurements and CFD simulation at 40 m/s

97.5% of the free stream value, indicating the beginning of the boundary layer. In Table 5.6, these boundary layer heights (as determined with CFD) were compared to the corresponding heights determined using PIV at 40 m/s.

The boundary layer was observed to reach a maximum size of $6.43mm$ at the furthest downstream point in the test section in both cases (PIV and CFD). However, there was a significant difference in the boundary layer size at the inlet of the test section. The PIV results showed a boundary layer of $1.34mm$ while the CFD simulations predicted a larger boundary layer of $3.02mm$. Consequently, the CFD simulation predicted boundary layer growth at an angle of 0.47^o compared to 0.71^o with PIV. There are several possible reasons for this discrepancy. First, the upstream conditions in the CFD model were very different from those in the wind tunnel. In the model, the inlet flow traveled along a 12.5 m long duct to ensure a fully developed velocity profile. In the wind tunnel, the velocity profile at the inlet was not fully developed due to the presence of corners 1 and 2. Second, in order to compensate for this, a screen and honeycomb section was installed before the contraction in the wind tunnel. These would likely act to decrease or delay the development of the boundary layer. As a third reason, it was possible that the interface between the contraction and the test section was not seamless in the wind tunnel as it was in the CFD model. Even an extremely small downwards step from the contraction wall to the test section wall (in the wind tunnel) could effectively disrupt the continuity of the wall boundary layer. In conclusion however, the results of this comparison proved to be satisfactory since the real measured boundary layer was smaller than the simulated boundary layer, resulting in a larger usable test section area than would have been predicted computationally.

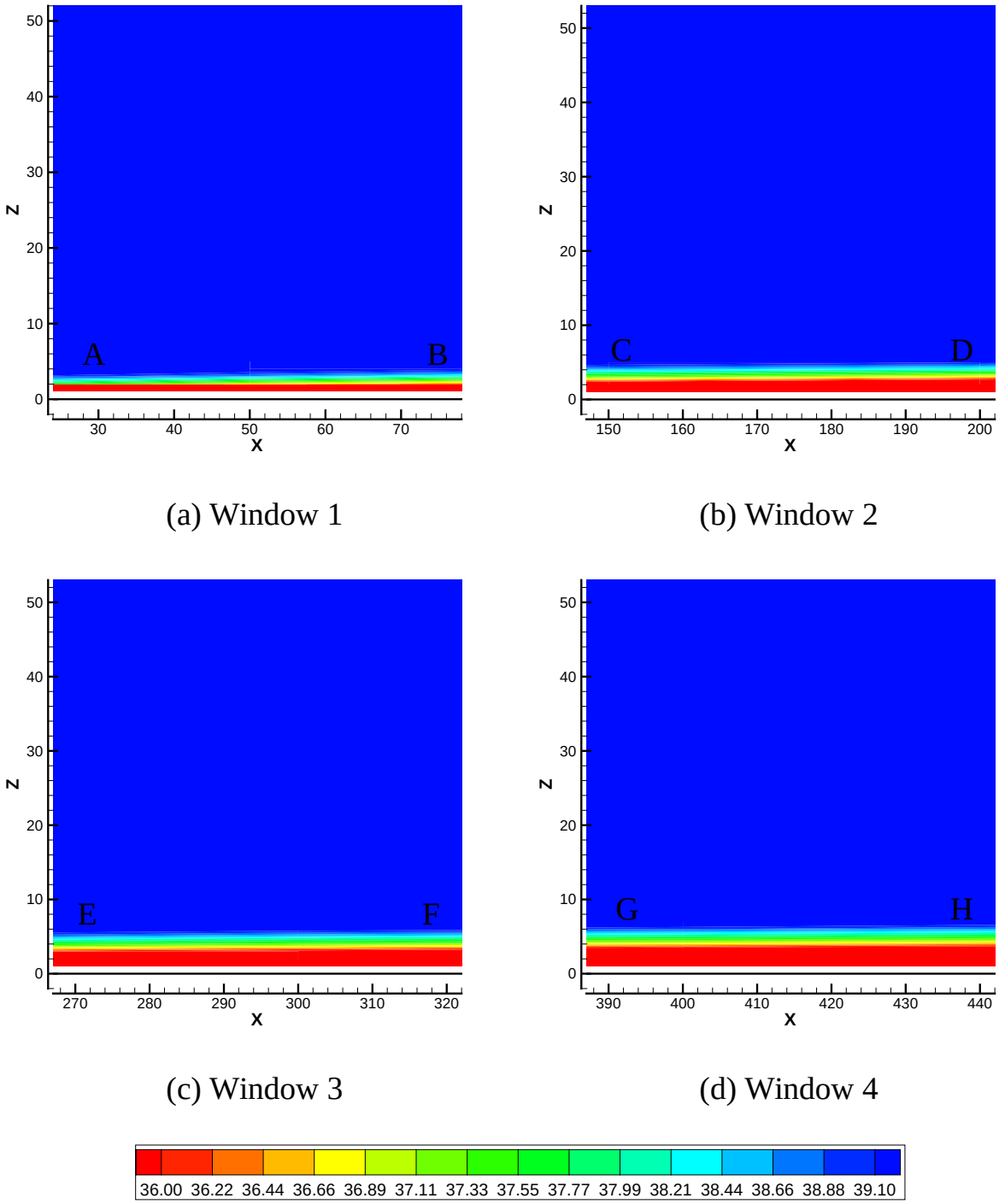

(a) Window 1

(b) Window 2

(c) Window 3

(d) Window 4

Figure 5.23: Longitudinal velocities along the test section wall at 40 m/s (CFD results). Note: All plots in this figure follow the same contour legend shown above, all axis dimensions in mm

5.7 Temperature Rise in the Wind Tunnel

5.7.1 Objective

As a final performance test for the wind tunnel in this study, it was necessary to determine the temperature behaviour within the tunnel. Without the presence of a heat exchanger to cool the flow in the wind tunnel, it was important to determine just how long the tunnel could be operated before the change in air temperature, and hence a change in fliud properties, would become a factor in the results.

5.7.2 Experimental Setup

In order to measure the air temperature within the wind tunnel, a K-type thermocouple was inserted into a hole in the wall of transition 1 (just upstream of the fan inlet). Figure 5.24 shows the setup used in this experiment. The thermocouple was connected to a Keithley 2700 Multimeter/Data Acquisition System, which allowed for the temperature data to be collected and transferred to a computer for post processing.

The experiment was comprised of three temperature trials, during which the tunnel was allowed to run at a constant speed for 45 minutes while the air temperatures were collected. Each of the three trials were run at different speeds; 10, 25, and 40 m/s, representing the full range of typical wind speeds in the test section.

5.7.3 Results

Figure 5.25 shows the results of the three temperature trials over the 45 minute span. In order to compare the three different test speeds, the relative temperatures were plotted (*i.e.* the initial temperature of each trial was subtracted from the collected data). For example, at a test section speed of 10 m/s, the temperature inside the wind tunnel rose by 1.6°C after 45 minutes. In terms of the air properties, this resulted in a 0.50% decrease in density, and a 0.086% increase in dynamic

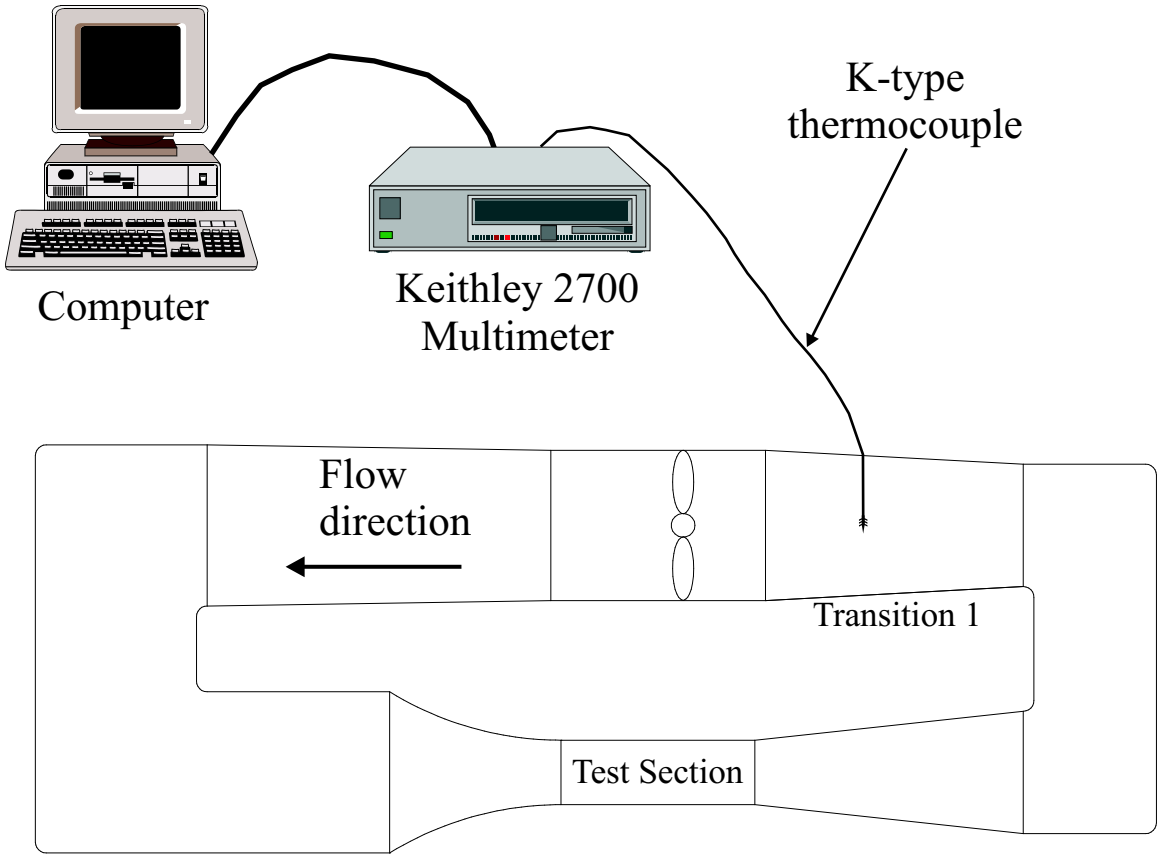

Figure 5.24: Experimental setup used for temperature measurements of the wind tunnel air flow

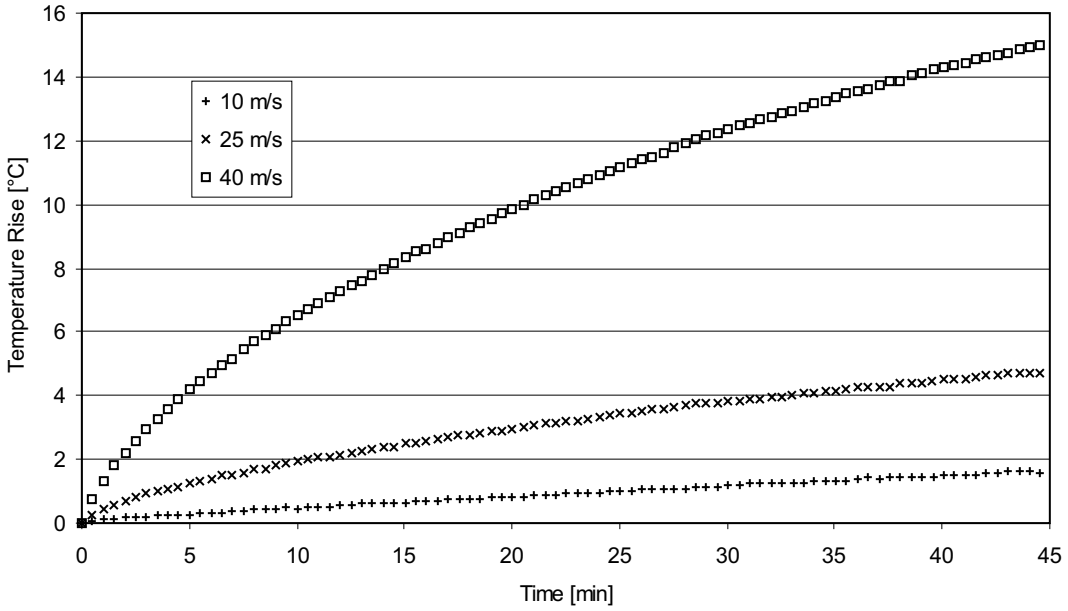

Figure 5.25: Temperature rise in the wind tunnel airflow at three constant speeds; 10, 25, and 40 m/s

viscosity [21]. At 25 m/s, the total temperature rise after 45 minutes was 4.7^{o}C, causing a 1.50% decrease in density and a 0.25% increase in dynamic viscosity [21]. At 40 m/s the temperature rose at a much higher rate than the two lower speeds, resulting in a 15.0^{o}C temperature rise in the wind tunnel. At this speed, the effect on the air properties was significant, with a 4.8% decrease in density and a 1.07% increase in dynamic viscosity [21]. Depending on the particular tolerances of the experiment, or the preferences of the operator, these results can be used as a guideline on how long each experiment should run before temperature effects would significantly affect the results. For example, if the maximum tolerable change in density was determined to be 2%, then a wind tunnel test at 40 m/s should not last more than 9 minutes.

The three temperature curves in Figure 5.25 were extrapolated using fourth-order polynomial curves in order to estimate the time at which an equilibrium temperature would be reached at each test speed. At 10 m/s, the temperature in the wind tunnel was estimated to stabilize after

202 minutes of continuous operation, at a temperature of approximately 4°C (above the initial temperature). At 25 m/s, the time to steady state was significantly reduced, with the tunnel stabilizing after only 59 minutes, reaching 5°C above the starting temperature. At 40 m/s, the estimated stabilization came after 52 minutes, rising to approximately 17°C above the initial temperature.

5.8 Summary

With the conclusion of these experiments, it was determined that the flow quality in the wind tunnel had been well characterized. The results showed a uniform, well aligned flow with low turbulence intensity. These qualities suggested that the wind tunnel in this study would be a suitable facility for obtaining useful experimental measurements on models placed in the test section.

In the following chapter, PIV measurements of the flow around a square cylinder are described, and the results are compared to previous experimental work.

Chapter 6

PIV Measurements of the Flow Over a Square Cylinder

6.1 Introduction

After validating the empty test section flow in Chapter 5, it was decided that further validation with an object placed in the test section would be necessary. For this experiment, a square cylinder was chosen. Two-dimensional measurements were performed in the wind tunnel using PIV, and the results were compared to previous experimental work. A review of the previous studies on the flow over a square cylinder is given in the next section, followed by an overview of the experimental setup along with the presentation and comparison of the results.

6.2 Literature Review - Flow Over a Square Cylinder

The flow over a square cylinder has been characterized in numerous reports, using methods such as LDV [66, 67, 68, 69], PIV [70], and DNS (direct numerical simulation) [71]. For comparison with the measurements obtained in this study, the LDV results of Lyn *et al.* [66, 67], Durao *et*

	Reynolds number	Turbulence intensity [%]	Blockage [%]	Aspect ratio	Measurement region
Lyn et. Al [66, 67]	21,400	2.0	7.0	9.75	{-0.5 < x/d < 8}, {0 < y/d < 2.5}
Durao et. al. [68]	14,000	6.0	13.0	6.00	{-0.5 < x/d < 6}, {-2 < y/d < 2}
McKillop & Durst [69]	15,000	2.0	10.0	10.50	{0 < x/d < 5}, {0 < y/d < 1.5}
Present study	21,400	2.0	8.3	12.00	{-0.8 < x/d < 6.3}, {-3.6 < y/d < 3.6}

Table 6.1: Summary of the experimental parameters used in Lyn *et al.* [66, 67], Durao *et al.* [68], McKillop and Durst [69], and the present study

al. [68], and McKillop and Durst [69] were chosen, as these reports provided the largest quantity of measurements at similar Reynolds numbers. Table 6.1 summarizes some of the experimental parameters used in these previous studies, as well as those used in the present study. The Reynolds number in Table 6.1 was calculated as,

$$Re = \frac{U_\infty d}{\nu} \tag{6.1}$$

where U_∞ is the free stream velocity in m/s, d is the side length of the cylinder in m, and ν is the kinematic viscosity of the working fluid, in m^2/s (Figure 6.1). The free stream turbulence (X-direction) value for this study was taken as the average of the turbulence intensity values determined in Chapter 5. The blockage (%) was calculated as the ratio of the cylinder frontal area to the test section cross sectional area, dL/B^2 (Figure 6.1). The aspect ratio was calculated as L/d, and the measurement regions were stated with reference to the origin shown in Figure 6.1.

6.3 Experimental Setup - Flow Over a Square Cylinder

To carry out the experiments, a square cylinder was fabricated out of acrylic, with a side length of $d = 12.7\ mm$, and a length of $L = 152.4mm$ in order to span the entire test section width. The origin of the coordinate system was located at the center of the square cylinder, as shown in Figure 6.1, to remain consistent with previous work. The average air temperature measured in the wind tunnel during the experiments was 28.9^{o}C, giving a kinematic viscosity of 1.59 $\times 10^{-5} m^2/s$

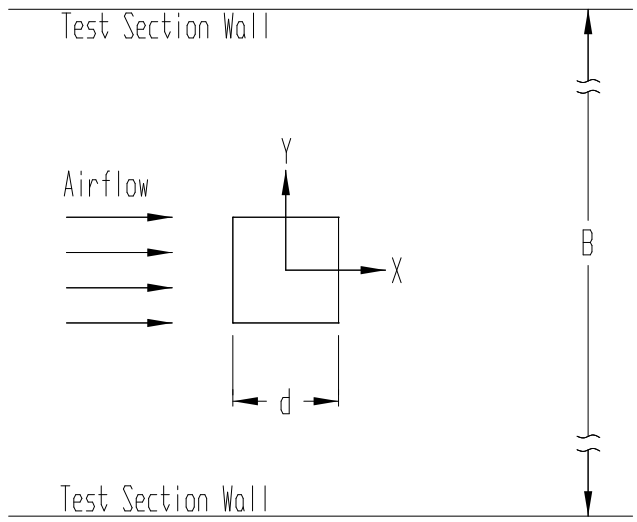

Figure 6.1: Definition sketch of the various flow parameters for a square cylinder

[21]. In order to match the Reynolds number used in the experiments of Lyn *et al.* [66, 67], a free stream velocity of $U_\infty = 26.8\ m/s$ was used, giving a Reynolds number of Re = 21,400.

The PIV system used here was the same as that used for the test section validation measurements in Chapter 5. The square cylinder was placed in the wind tunnel, spanning the test section horizontally. A vertical light sheet was used, resulting in a setup similar to that used for the vertical plane test section measurements (Figure 5.8). The window of measurement was $91.6mm$ x $92.5mm$, giving a resolution of 0.091 $mm/pixel$. A total of 1000 image pairs were collected, with a time separation of 7 μs between exposures. The cross correlation was performed using interrogation areas of 16 x 16 pixels, or $1.45mm$ x $1.45mm$ with an overlap of 50%. This resulted in a total of 15,750 (125 x 126) vectors.

Table 6.2 lists the estimation of the PIV error sources outlined in Section 4.3.4. Based on these estimated values, a total error of $0.0092mm$ (in the measured particle displacements) was calculated, resulting in a percentage error of 4.9% in the determined velocities. This error was higher than the typical error estimated for the experiments in Chapter 5 (approximately 2% to 2.5%). The main reason for this was the choice of smaller interrogation areas (16 x 16 pixels) for

Error Source	Error Estimate	Total Error [mm]	Description
Image Recording	Negligible		Amount of electrical noise not known
Contrast	Negligible		Level of contrast was high in all images (above 100 counts of contrast)
Particle Number Density	0.0175 pixels	5.03E-05	Taken as lowest error value from Figure 4.6 of Huang *et al.* [49] since all interrogation areas contained at least 50 particles
Loss of Pairs Due to Out-of-Plane Motion	Negligible		Maximum out-of-plane velocities were not known here, but assumed to be highly two-dimensional. (Out-of-plane velocities would have to be 107 m/s in order to travel 1/4 of the laser sheet thickness)
Parallax	0.00304 pixels	8.07E-06	Calculated from the estimates of Sinha [51] using a 92mm x 92mm measurement area, 0.5 m/s maximum out-of-plane displacement (this was assumed to be a worst case, as this flow was expected to be largely two-dimensional), and a distance of 570mm from the camera lens to the measurement plane
Tracking Error	Negligible		Mineral oil was calculated to have a response time of 0.00000009 (*i.e.* time lag with respect to air)
Acceleration Errors	Negligible		Acceleration unknown but assumed negligible since the empty test section flow was expected to be extremely uniform and steady
Velocity Gradient Error	Negligible		Velocity gradients here may not be negligible, but this was compensated for with higher resolution and smaller interrogation areas
Particle Image Size	Negligible		Negligible since the particles were assumed to be smaller than 1 pixel, resulting in cross correlation of entire smoke particle-clusters
Sub-pixel Interpolation	0.10 pixels	9.10E-03	Based on the theoretical and simulation results of Westerweel [55]

Table 6.2: Estimation of the PIV errors in the square cylinder measurements

the square cylinder measurements. An error value of $0.0092mm$ would have twice the effect in a 16 x 16 pixel interrogation area as compared to a 32 x 32 pixel area.

6.4 Results and Comparison

6.4.1 Mean Velocities

All of the velocity results presented in this section were normalized by the free stream velocity, U_∞, giving u^* and v^*. As well, the X and Y dimensions were normalized by the cylinder side length, d, giving x^* and y^*. Figure 6.2 (a) shows a contour plot of the resultant velocities obtained over the entire $91.6mm$ x $92.5mm$ measurement area. In all three plots (a through c) of Figure 6.2, the square cylinder (drawn in white) was located at $(x^*, y^*) = (0,0)$. In Figure 6.2 (b), a

closer view of the area surrounding the square cylinder is shown, with velocity vectors included to show direction. The overall flow picture displayed reasonable symmetry about the x^* axis. The area immediately upstream (to the left) of the cylinder between $y^* \approx \pm 0.5$ was not captured in the PIV images due to the positioning of the camera. This area therefore contained erroneous velocity data in all of the plots in this chapter.

The velocities in Figure 6.2 exceeded the free stream value immediately upon rounding the forward facing corners due to blockage. The flow also separated at the two forward corners, leaving areas of extremely low velocities near the upper and lower surfaces of the cylinder. In the near wake of the cylinder, a large velocity defect was observed, which gradually decreased further downstream, but remained present at more than 5 side lengths downstream from the cylinder (Figure 6.2 (c)).

6.4.2 Turbulent Kinetic Energy

In Figure 6.3, the non-dimensional turbulent kinetic energy is plotted around the square cylinder. These values were calculated by dividing K_t (as calculated in Eq. 5.4.3) by U^2.

As expected, a core of high turbulence was observed in the wake of the cylinder, with the highest values located in the near wake at $x^* \approx 1.6$ (just over one side length downstream of the cylinder trailing edge). In this area, the turbulent kinetic energy levels were in the range of 0.32 to 0.35 (or 230 to 250 m^2/s^2), approximately 1250 times higher than the free stream turbulence level (free stream average of 0.2 m^2/s^2 from Chapter 5 results). This area also contained high velocity gradients as observed in Figure 6.2.

After viewing the overall flow patterns around the square cylinder, it was necessary to explore the flow characteristics in greater detail. In the following section, velocity profiles over the top surface of the cylinder are shown and compared to the previous work of Lyn *et al.* [66].

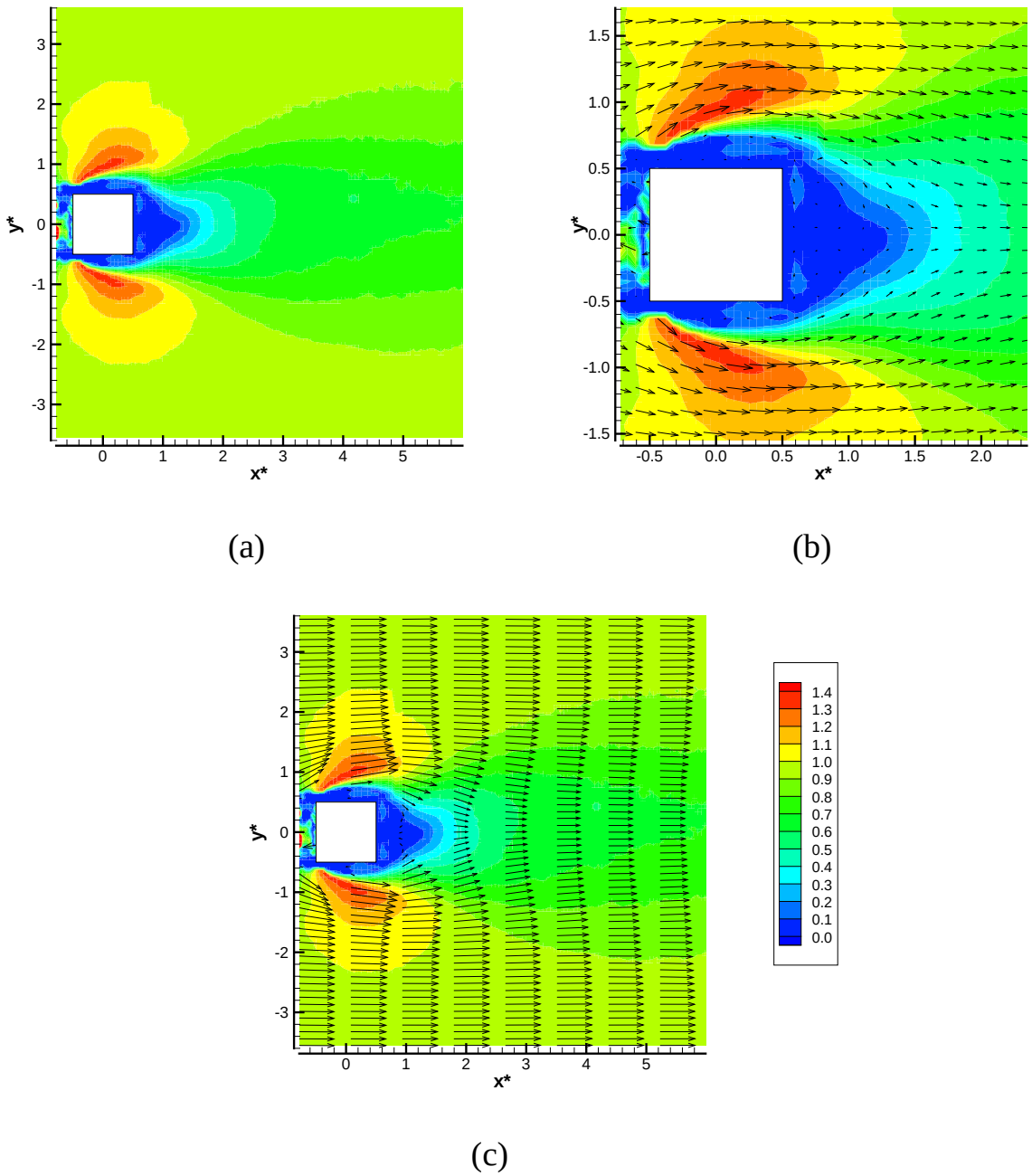

Figure 6.2: Velocities measured over the square cylinder at $Re = 21{,}400$ (a) Dimensionless resultant velocities plotted over the entire measurement window, (b) dimensionless resultant velocities and vectors near the square cylinder, (c) dimensionless velocity profiles plotted downstream of the cylinder showing the velocity defect present (square cylinder drawn in white on all plots) Note: All plots in this figure follow the same contour legend shown above.

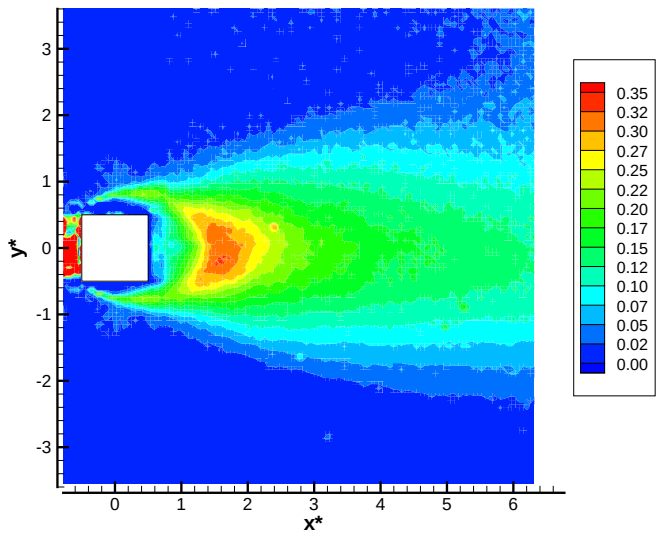

Figure 6.3: Dimensionless turbulent kinetic energy levels around the square cylinder at Re = 21,400

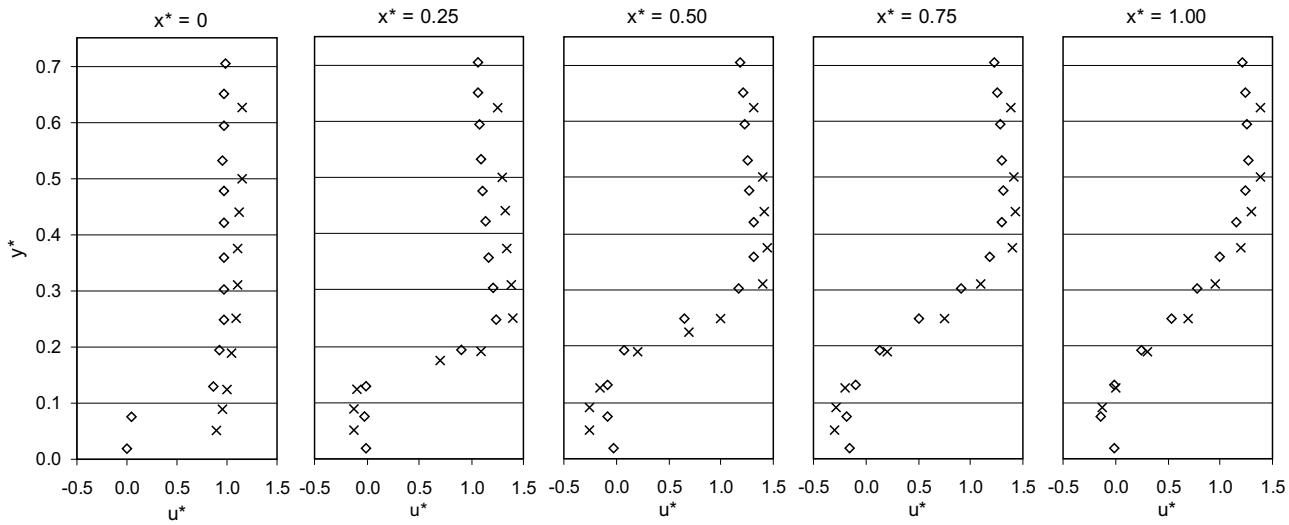

Figure 6.4: Dimensionless mean velocity profiles over the top surface of the square cylinder at $Re = 21{,}400$ at $x^* = 0$, 0.25, 0.50, 0.75, and 1.00: $\diamond$, present results; $\times$, Lyn *et al.* [66]

6.4.3 Flow Characteristics Over the Top Surface of the Square Cylinder

Figure 6.4 shows five velocity profiles along the top surface of the square cylinder. For simplicity, the origin of the coordinate system was placed at the top left corner of the cylinder (shifted from the original definition in Figure 6.1). Therefore, the first profile in Figure 6.4 at $x^* = 0$ was located at the leading edge of the top surface, while the last one ($x^* = 1.00$) was located at the trailing edge. These profiles are compared in the same figure to those measured by Lyn et. al [66]. Good agreement was found here, with the shape of each profile being very similar at each of the five locations. The only notable discrepancy found between the two data sets was a consistent shift of the measured velocities. In all five plots, the velocities obtained in this study were appoximately 10% lower than those measured by Lyn *et al.* [66].

At the leading edge of the cylinder's top surface ($x^* = 0$), the velocity profile was not retarded, and most of the velocities measured were equal to the free sream velocity ($u^* = 1$). By the second station ($x^* = 0.25$), signs of flow separation became evident, with an area of low velocity

extending from the cylinder surface ($y^* = 0$) to $y^* = 0.15$. The rapid change in velocity between $y^* = 0.15$ and $y^* = 0.2$ is indicative of the forming of a shear layer due to separation from the top left corner of the cylinder. A detailed characterization of this shear layer can be found in Lyn *et al.* [66]. After this point, the shear layer appeared to begin flapping, or oscillating in the y^* direction. This can be seen in the three plots at $x^* = 0.50$, 0.75, and 1.00, where the increase in velocity took place over an increasingly larger distance. At $x^* = 0.50$, the maximum velocity was reached at $y^* \approx 0.37$. At $x^* = 1.00$, however, the maximum velocity was not reached until $y^* \approx 0.53$. It is important to note here that the shear layer still existed at these downstream locations, but due to its oscillation, its presence was spread out by the averaging process. Furthermore, the size of the velocity transition region (0.3 y^* units at $x^* = 1.00$) gave an indication of the amplitude of oscillation of the shear layer.

Figure 6.5 plots the non-dimensionalized x^*-direction turbulence intensities (u') measured over the top surface of the cylinder at the same x^* locations as in Figure 6.4. The u' values plotted here represent the rms fluctuating velocity components, divided by the free stream velocity, U_∞. Good agreement was also seen here when compared to the results of Lyn *et al.* [66], although the turbulence intensities measured in this study were consistently higher (by an average of 0.1 normalized turbulence units) than those measured by Lyn *et al.* [66]

The most important feature of the plots in Figure 6.5 was the location of the highest turbulence intensity in each. It is reasonable to expect that the turbulence intensity should peak in the areas of highest velocity gradients, or in this particular case, in the area where the shear layer developed. This was in fact the case in Figure 6.5, where the peaks in u' occurred in the same y^* locations as the largest velocity gradients in Figure 6.4. At $x^* = 0.25$, the peak in turbulence intensity was very narrow, with values dropping off sharply above or below $y^* = 0.2$. Further downstream, these peaks became wider, with turbulence values blending gradually above and below the peak. This behaviour was again indicative of a shear layer (area of high velocity gradient) which was not fixed in location, but instead oscillated between $y^* = 0.1$ and $y^* = 0.4$ at $x^* = 1.00$.

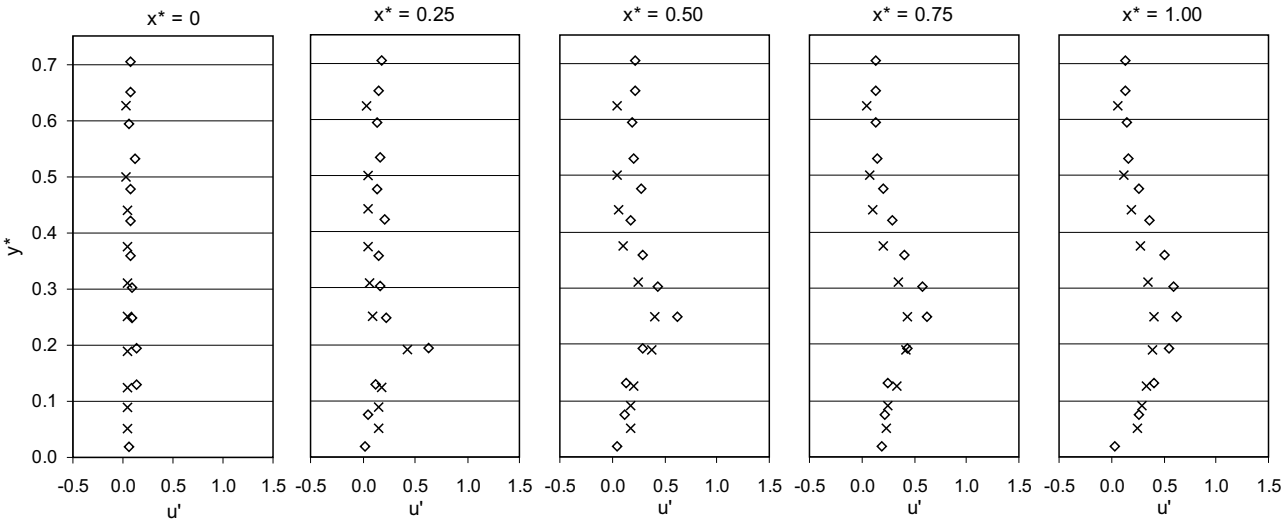

Figure 6.5: Non-dimensionalized turbulence intensities measured over the top surface of the square cylinder at $Re = 21{,}400$ at $x^* = 0$, 0.25, 0.50, 0.75, and 1.00: $\diamond$, present results; $\times$, Lyn *et al.* [66]

6.4.4 Flow Characteristics in the Wake of the Square Cylinder

In this section, the velocities measured in the wake behind the square cylinder are investigated. Specifically, the velocities and turbulence statistics measured along the centreline ($y^* = 0$ in Figure 6.1) were plotted and compared to the results of Lyn *et al.* [67], Durao *et al.* [68], and McKillop and Durst [69].

In the near wake of the cylinder, starting at $x^* = 0.5$, negative velocities were observed (flowing towards the back surface of the cylinder in Figure 6.1). This indicated a region of recirculation behind the cylinder. In the LDV results in Figure 6.6 (a), this recirculation zone appeared more pronounced than in the present results, with u^* velocities reaching -0.20 at $x^* = 1.0$ in Lyn *et al.* [67], Durao *et al.* [68], and McKillop and Durst [69] as opposed to -0.08 in the results of this study. Past $x^* = 2$ (1.5 side lengths downstream of the cylinder trailing edge), the present results agreed well with the three previous experiments [67, 68, 69]. With increasing distance downstream of the cylinder, the centreline velocity gradually approached the free stream value. However, these velocities only reached $0.7U$ at 5.5 side lengths downstream, and the asymptotic nature of the curve in Figure 6.6 (a) suggested that the centreline velocity would not be recovered for at least another $30d$ further downstream.

In Figure 6.6 (b), the x^* direction turbulence intensities (u') measured in this study showed good agreement with those of McKillop and Durst [69], but were lower than those measured by Lyn *et al.* [67] and Durao *et al.* [68]. However all datasets showed similar behaviour, with the highest turbulence intensities occurring at $x^* = 1.25$ (approximately $0.75d$ downstream of the cylinder trailing edge) and leveling off further downstream.

A similar relationship was observed in Figure 6.6 (c), where the y^* direction turbulence intensities (v') measured in this study were lower than those measured by Lyn *et al.* [67] and Durao *et al.* [68] but similar to those of McKillop and Durst [69]. Here, the results of Lyn *et al.* [67] peaked at $x^* = 1.85$ while the other three datasets suggested a peak of turbulence intensity closer to $x^* = 1.65$. The turbulence levels then decreased with increasing downstream distance, falling to 0.45 at $x^* = 6.0$.

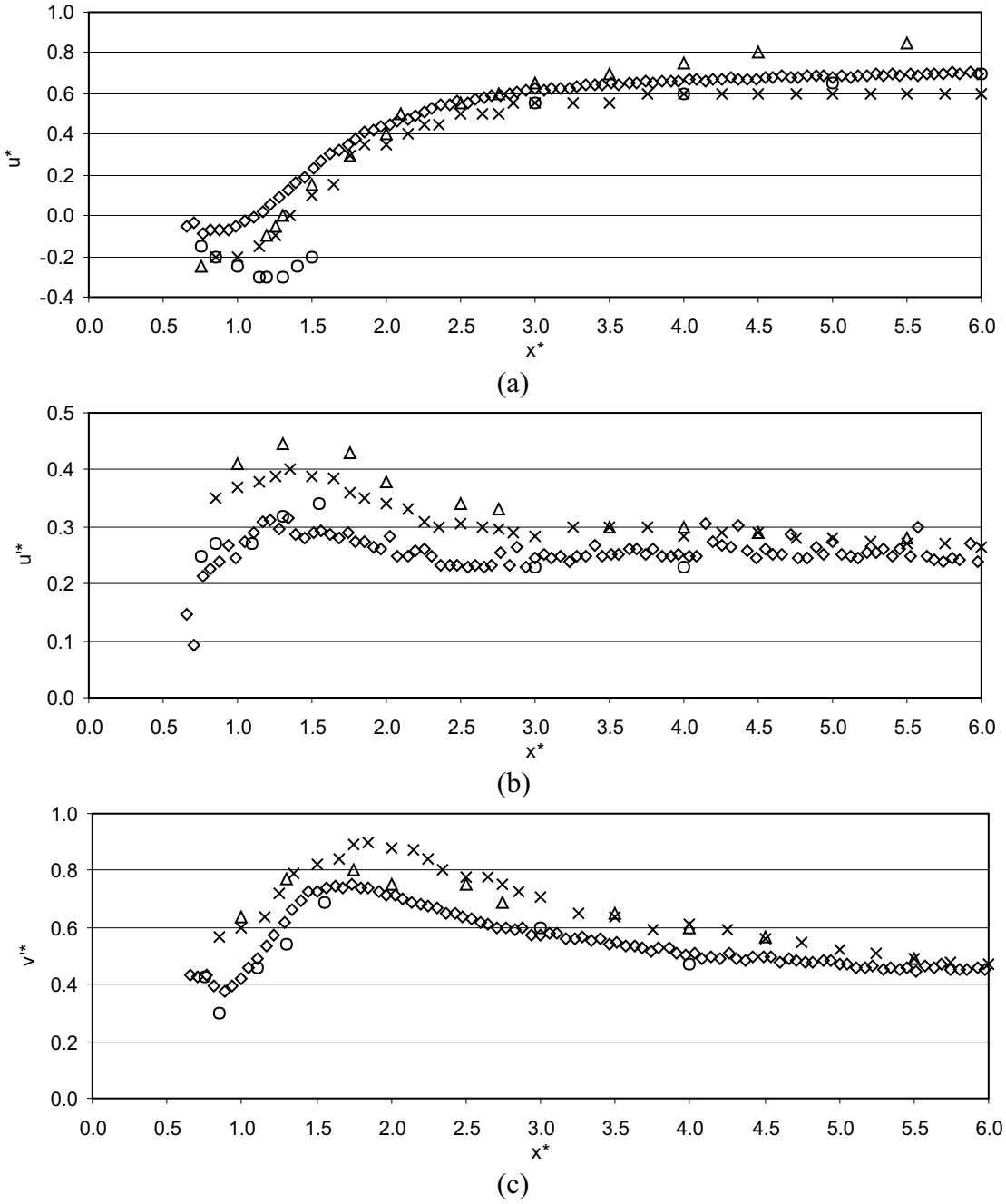

Figure 6.6: Dimensionless centreline velocities ($y^* = 0$) measured in the wake of the square cylinder at $Re = 21{,}400$. (a) dimensionless velocities, u^*; (b) dimensionless turbulence intensity in the x^* direction, u'; (c) dimensionless turbulence intensity in the y^* direction, v'. $\diamond$, present results; $\times$, Lyn *et al.* [67]; $\triangle$, Durao *et al.* [68]; $\circ$, McKillop and Durst [69]

6.4.5 Comparison of Instantaneous Flow Field Measurements

The results presented thus far have shown the time averaged flow field characteristics around the square cylinder. This flow however, has been shown by Lyn *et al.* [66] to be approximately periodic due to vortex shedding. The PIV measurement technique used in this study did not allow for temporal velocity data to be resolved. This was due to the fact that the PIV system used here only controlled the time separation between the two images of an image pair, but not the time separation between complete pairs. That is, PIV could only provide spatially resolved velocity data collected at random time intervals (approximately every 0.25s). It was, however, possible to view the data from individual image pairs, providing an instantaneous snap shot of the flow in each case. Figure 6.7 shows 3 of the 1000 image pairs used to determine the average flow field around the cylinder. Each one of these instantaneous pictures is significantly different from the next, indicating unsteadiness and/or periodicity in the flow. For example, in Figure 6.7 (a), the dominant flow behind the cylinder was directed downward in the region $1.2 < x^* < 3$. Conversely, in Figure 6.7 (b), this same area contained flow directed upwards, indicating oscillatory behaviour in the wake. In Figure 6.7 (c), vortex shedding is evident with a clockwise rotating vortex centered at $(x^*, y^*) = (1.8, -0.2)$ and a weaker, counter-clockwise vortex centered at $(x^*, y^*) = (4.1, 0.5)$. These instantaneous flow pictures show an unsteady flow behaviour which was effectively eliminated in the averaging process that gave the flow field seen in Figure 6.2. The high levels of K_t in Figure 6.3 also indicate this unsteady behaviour, since high K_t levels were the result of large standard deviations in the u^* and v^* velocities.

6.5 Conclusions

In this chapter, the flow around a square cylinder was characterized in the wind tunnel using PIV measurements. The comparison of these results with the previous results of Lyn *et al.* [66, 67], Durao *et al.* [68], and McKillop and Durst [69] indicated that the wind tunnel in this study was able to accurately reproduce velocity measurements of a known flow field.

In the following chapter, PIV measurements are reported on a less-studied flow field. Specifically, the following chapter presents the measurements of the flow around an open-wheeled racecar.

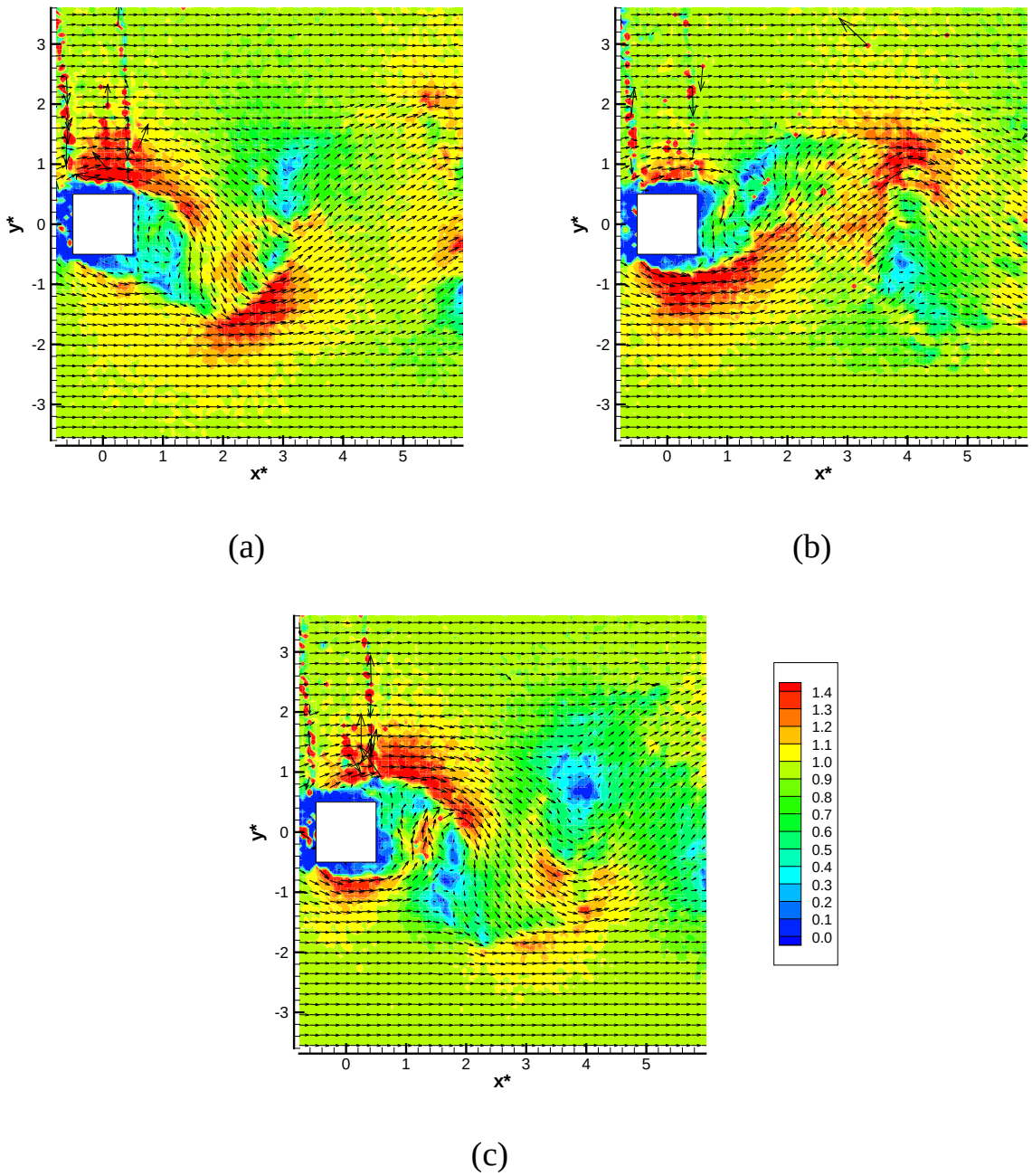

Figure 6.7: Instantaneous pictures of the flow field around the square cylinder at $Re = 21{,}400$. Dimensionless resultant velocities shown by contours and direction is shown by the vectors. Note: All plots in this figure follow the same contour legend shown above. Figures were taken at different instances in time.

Chapter 7

PIV Measurements of the Flow Over a Formula One Racecar

7.1 Introduction

In this chapter, PIV measurements are described for flow over a more complex geometry in order to further test the flexibility and robustness of the wind tunnel/PIV system. The geometry chosen was that of a Formula One racecar (1:18 scale model). The flow over the model was measured in four different planes over its entire length using PIV. Due to the absence of any specific published results on racecar aerodynamics, it was impossible to compare the present results to previous works. Therefore, the results are presented here and discussion is provided where available.

7.2 Model Setup

In order to obtain velocity measurements from a scale model, which could be applied to the full scale prototype, it was essential to have a model with accurate geometry and surface finish. A model fabricated by Mattel Inc. (United States) to a very high level of detail was found. Several

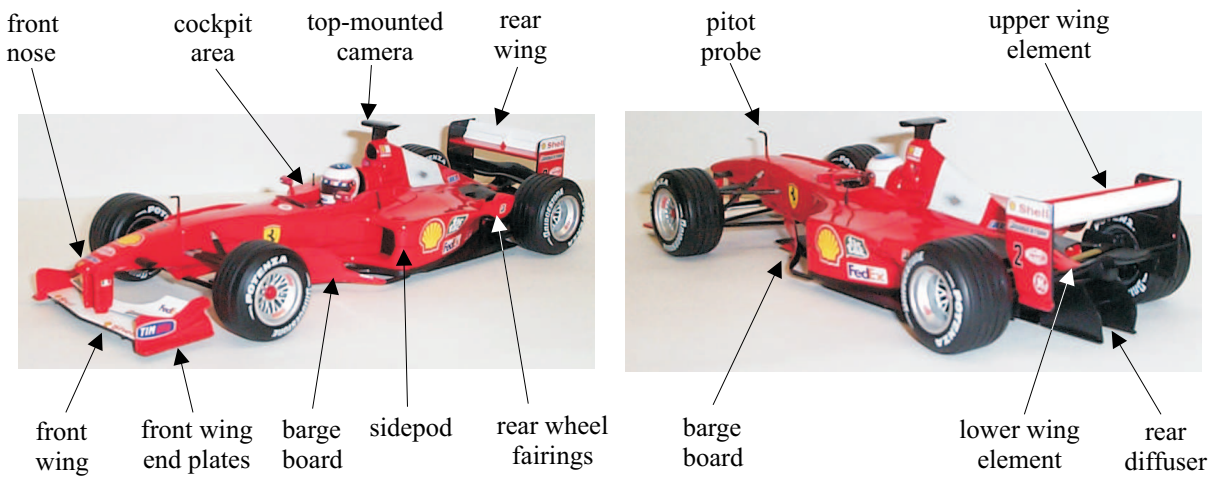

Figure 7.1: Formula One racecar model used for aerodynamic measurements (1:18 scale)

dimensions of the model were measured and verified against the full scale dimensions [72]. The overall length, width, height, and the front and rear track widths were measured and found to scale properly to the corresponding full scale dimensions. The die-cast model therefore provided accurate geometry as well as surface finish, and was considered ideal for the present study.

Figure 7.1 shows the 1:18 scale Formula One racecar used for the measurements in this study. The various elements of the racecar model are labeled for reference in later sections. In order to keep the model away from the boundary layer of the test section walls, it was mounted on a platform which elevated the model to the middle of the test section. The platform served a dual purpose in this case. Apart from elevating and mounting the model, its wedge-shaped leading edge acted as a flow splitter as well (Figure 7.2). Mounting the model only $8mm$ from the leading edge of the platform allowed very little length for a new boundary layer to develop before reaching the front of the racecar. The maximum width of the racecar model was $102mm$, leaving approximately $25mm$ between the wheels and the test section walls.

The platform and model were mounted in the test section using four lengths of threaded rod that allowed leveling adjustments of the platform at each of the four corners to be made. The model was mounted sideways in the test section in order to allow for more convenient laser and

Figure 7.2: Formula One racecar model mounted on test platform

camera locations (Figure 7.3). The model was held to the platform using two small mounting screws on its underside. The platform, measuring $300mm$ in length, spanned the entire test section width in order to avoid any end flow effects along its edges. It is important to note that these experimental conditions were simplified compared to the real world case. The absence of a moving ground plane would result in the formation of a boundary layer, however small, along the mounting plate. In addition, the wheels of the racecar model did not rotate during the tests, further simplifying the flow over the wheels.

7.3 Model Scaling Effects

Before conducting any velocity measurements on the racecar model, it was important to assess how the model testing parameters would scale to the full scale vehicle. The Reynolds number, Re, was calculated as,

$$Re = \frac{UL}{\nu} \tag{7.1}$$

where U was the free stream velocity, in m/s, ν was the kinematic viscosity of air, in m^2/s, and L was taken as the overall length of the racecar, in m. With a free stream velocity of 40 m/s in the tunnel, a kinematic viscosity of 1.612×10^{-5} m^2/s [21], and a length of $243mm$ ($0.243m$),

the Reynolds number was calculated to be 603,000. Since the Reynolds number determined here was very large, it was assumed that the inertial forces greatly overpowered the viscous forces, allowing for the viscous forces to be neglected outside the surface boundary layers [21]. This assumption made it possible to overlook Reynolds number similarity between the model and the full scale vehicle [21]. In other words, it was reasonable to assume that a flow of 40 m/s applied to the model in this study would correspond to a 40 m/s (144 km/hr) velocity applied to the full scale vehicle as well. For exact Reynolds number similarity to be maintained, the model would have to be tested at 720 m/s to simulate 40 m/s over the full scale vehicle. This is more than twice the speed of sound, and obviously an unreasonable test speed.

7.4 Vertical Plane Measurements - Formula One Racecar

7.4.1 Objective

The flow over the racecar model was first investigated using a vertical measurement plane (with respect to the model orientation). The main objective for these experiments was to observe the air flow over the model in two different $X-Z$ planes. The first plane of measurement was located at the model centreline, while the second plane was located over the wheels of the racecar model.

7.4.2 PIV Setup - Formula One Racecar - Vertical Plane

In order to obtain a vertical measurement plane with the model setup shown in Figure 7.3 (a), a horizontal light sheet was needed. Figure 7.3 shows the hardware setup used as well as the locations of the two measurement planes. The first measurement plane was located at $Y = 0$ (model centreline) and would show the flow characteristics over the aerobody and rear wing of the model. The second plane was located at Y = -37mm, showing the flow over the front and rear wheels as well as the sidepod.

Three PIV measurement areas were needed to perform measurements over the entire length of the vehicle (243mm). Sizing each of these areas at 100mm x 100mm created a measurement

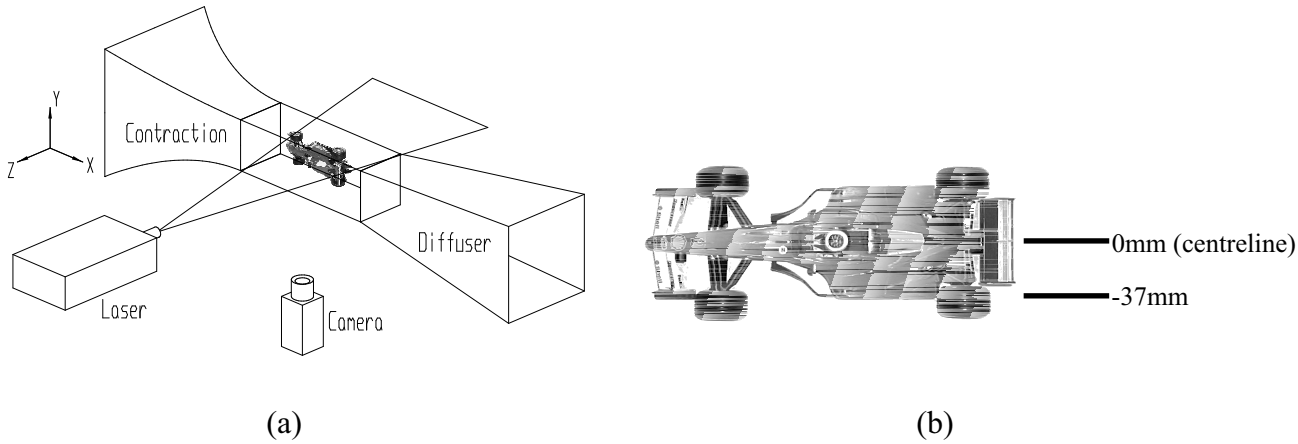

Figure 7.3: PIV setup used in the vertical plane measurements performed on the Formula One racecar model, (a) hardware setup (b) location of measurement planes

plane of $300mm$ in length, allowing for measurement of the near wake behind the racecar as well. This resulted in a resolution of $0.099mm$/pixel.

For each of the three measurement areas, a common origin/calibration method was used in order to ensure that the results could be joined together accurately to form one complete measurement plane over the model. At each location, 250 image pairs were collected, and a time separation (Δt) of 14 μs was used. All cross correlations were performed using interrogation areas of 32 x 32 pixels ($3.17mm$ x $3.17mm$) and 50% overlap, resulting in 3,844 (62 x 62) vectors in each area, or a total of 11,532 vectors over one complete plane.

Figures 7.4 (a through c) and 7.5 (a through c) show the calibration images of each of the six measurement windows used in vertical plane tests. The use of the long scale made it easy to match each of the adjacent measurement windows to each other.

Corresponding PIV images are shown in Figures 7.4 and 7.5 (d through f), below the calibration images. These figures show the unique challenges in performing PIV measurements on the racecar model. With a model fabricated primarily from die cast metal and painted to a glossy red finish, several challenges arose in obtaining clean PIV images (*i.e.* with minimal light reflection and

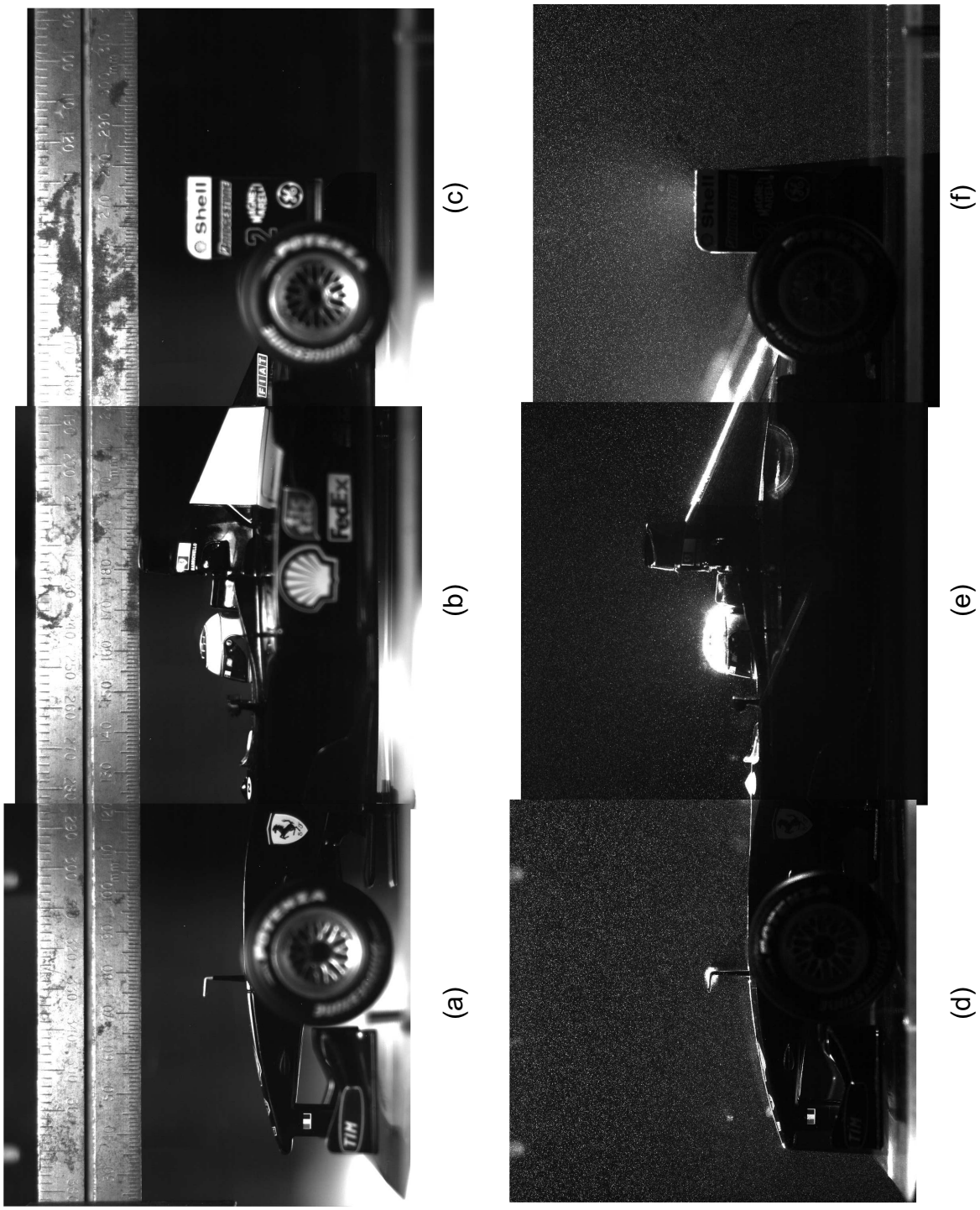

Figure 7.4: Calibration (a to c) and sample PIV images (d to f) obtained in the vertical plane measurements over the racecar model (centreline)

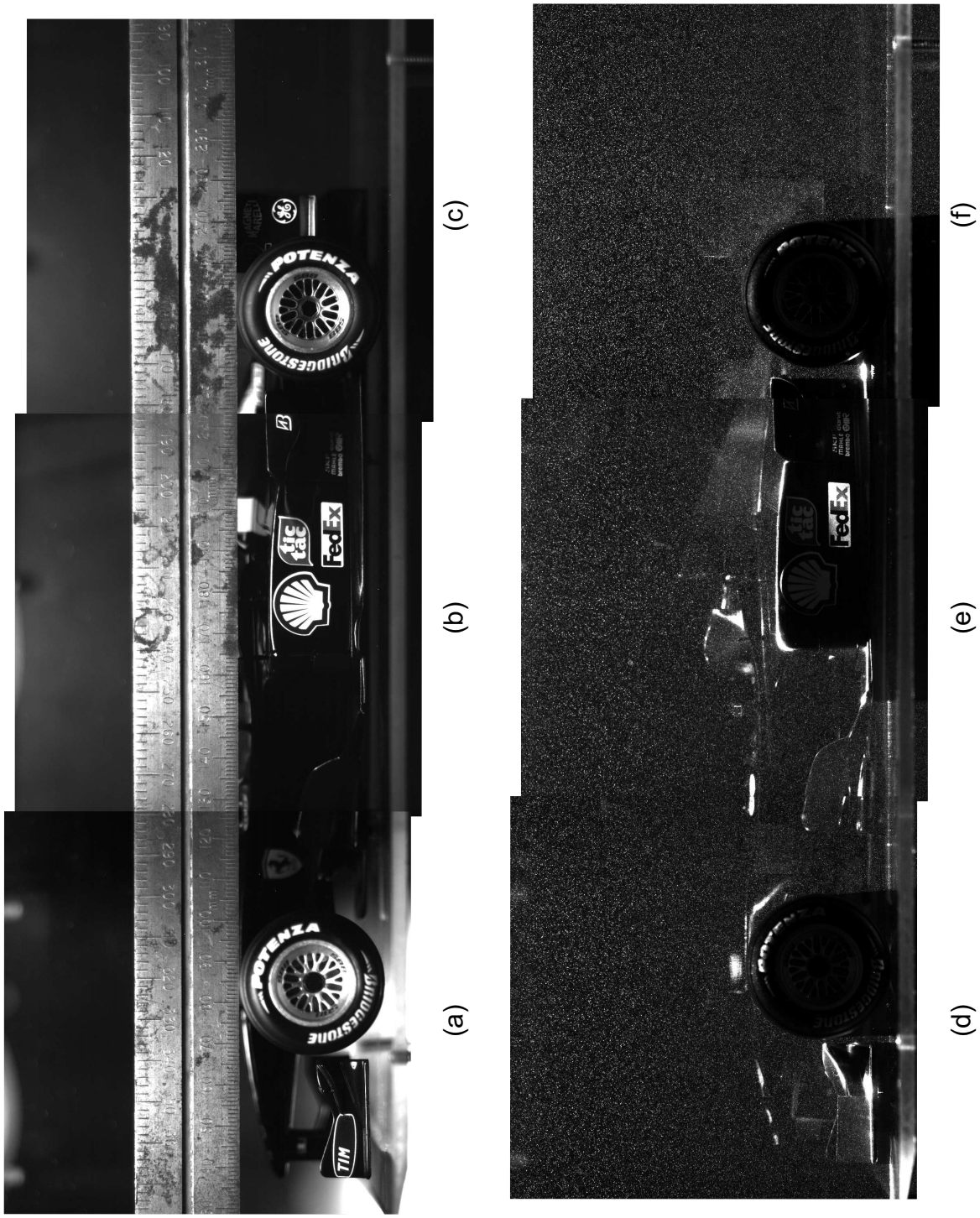

Figure 7.5: Calibration (a to c) and sample PIV images (d to f) obtained in the vertical plane measurements over the racecar model (in the plane of the wheels)

adequate contrast level). For example, in performing the measurements along the centreline plane, problem areas included the pitot tube (mounted on the nose just above the front wheels), the driver's helmet, and the bodywork extending at a downwards slope towards the rear wheels. All of these areas caused bright spots in the PIV images as a result of laser light reflection. These areas needed to be kept to a minimum in order to obtain as much useful velocity data as possible. The main areas of reflection could be covered with small pieces of black electrical tape, while flat black paint could be applied to other small areas on the model. In the plane of the wheels (Figure 7.5), the major problem areas were actually behind the plane of measurement, such as the driver's helmet and bodywork near the centreline of the model. Each successive measurement window required different solutions to cover and reduce the reflective areas. The main objective, however, remained the same for all measurement windows; ensuring that as many seeding particles as possible could be seen and distinguished in the PIV images.

In Table 7.1 the amount of expected error in the PIV measurements was estimated according to the PIV error sources outlined in Section 4.3.4. A total error of $0.0113mm$ (in the measured particle displacements) was calculated, resulting in a percentage error of 2.0% in the determined velocities.

7.4.3 Results - Formula One Racecar - Vertical Plane

Centreline Plane

The following results were obtained from the average of 250 image pairs, with a free stream velocity of $U = 40\ m/s$. Figure 7.6 shows the average velocities obtained along the centreline over the racecar model in m/s (see Figure 7.4 for corresponding PIV images). The origin of the $X - Z$ axis was placed at the tip of the racecar's front nose, level with the ground (platform). A picture of the racecar model was superimposed on the results in order to provide a visual reference and to cover the unusable data inside the boundaries of the model.

From the centreline measurements in Figure 7.6, the aerodynamic effects of the various elements of the model could be seen. The first notable flow disturbance arose from the pitot tube (wind speed

Error Source	Error Estimate	Total Error [mm]	Description
Image Recording	Negligible		Amount of electrical noise not known
Contrast	Negligible		Level of contrast was high in all images (above 100 counts of contrast)
Particle Number Density	0.0175 pixels	1.10E-04	Taken as lowest error value from Figure 4.6 of Huang *et al.* [49] since all interrogation areas contained at least 50 particles
Loss of Pairs Due to Out-of-Plane Motion	Negligible		Maximum out-of-plane velocities were not known here, but assumed to be of an acceptable magnitude. (Out-of-plane velocities would have to be 107 m/s in order to travel 1/4 of the laser sheet thickness)
Parallax	0.288 pixels	1.28E-03	Calculated from the estimates of Sinha [51] using a 100mm x 100mm measurement area, and 25 m/s maximum out-of-plane displacement (this was assumed to be the worst case), and a distance of 620mm from the camera lens to the measurement plane
Tracking Error	Negligible		Mineral oil was calculated to have a response time of 0.00000009 (*i.e.* time lag with respect to air)
Acceleration Errors	Negligible		Acceleration unknown but assumed negligible since the empty test section flow was expected to be extremely uniform and steady
Velocity Gradient Error	Negligible		Velocity gradients were not known here, but were assumed to be small within each interrogation area (3.17mm x 3.17mm in size)
Particle Image Size	Negligible		Negligible since the particles were assumed to be smaller than 1 pixel, resulting in cross correlation of entire smoke particle-clusters
Sub-pixel Interpolation	0.10 pixels	9.90E-03	Based on the theoretical and simulation results of Westerweel [55]

Table 7.1: Estimation of the PIV errors in the Formula One racecar model measurements

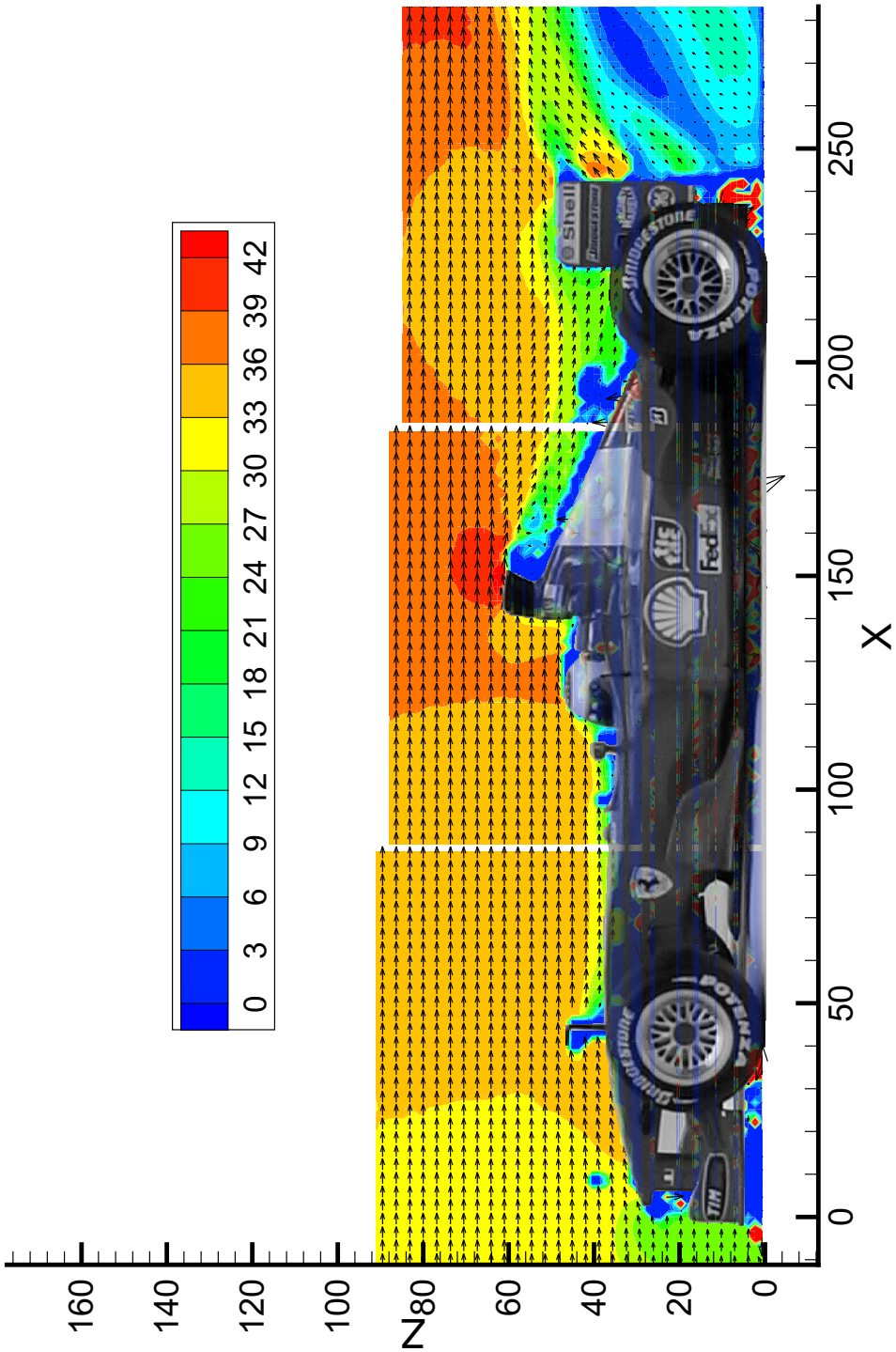

Figure 7.6: Average velocities measured in the vertical plane along the centreline of the racecar model (in m/s) Note: All axis dimensions in mm, some vectors removed for clarity

measurement device), located downstream of the front nose of the racecar, at $X, Z \approx 44{,}40$. The stem of the pitot tube caused a 3 to 6 m/s reduction in the downstream velocities, propagating along the remainder of the nose all the way to the driver's helmet. It was important to note here that this flow effect could only have been captured at the centreline of the model, and would likely not have been seen at all had the measurement plane been 2 or $3mm$ to either side of the centreline. Upon reaching the driver's helmet, the air flow was observed to increase by 3 m/s as it accelerated around the helmet contour. The highest wind speeds were seen just above the top-mounted camera (at $X, Z \approx 150{,}50$). This area represented the largest amount of flow redirection, as the average resultant velocity reached 46.5 m/s over the top of the camera. Downstream of the top-mounted camera, the flow attempted to re-attach itself along the downwards sloping bodywork (towards the rear wheels). This was only partly achieved, as the flow did re-attach (as evidenced by the downward sloping vectors), but did so at a reduced speed (approximately 25 m/s). The final, and largest disturbance to the flow was caused by the rear wing of the racecar model. The uppermost wing element did not redirect a significant amount of flow, but accelerated the flow at its trailing edge ($X, Z \approx 238{,}50$). The lower wing element was observed to significantly redirect the flow in this region ($X, Z \approx 245{,}38$), where the air flow exiting the wing area was directed upwards at 40° from the horizontal. This produced a substantial change in flow momentum, as the flow incident on the lower wing element was directed downwards by as much as 35° from the horizontal ($X, Z \approx 220{,}38$). A third downforce-producing device was located in the rear diffuser, where a plate diverted a portion of the underbody flow upwards (in the region exiting at $X, Z \approx 246{,}20$). In this area, the direction of flow ranged from 40° to 50° upwards from the horizontal.

The flow in the near wake of the racecar model provided some insight on the topic of vehicle draughting. Vehicle draughting is a tactic used by racecar drivers to perform passing maneuvers on competing racecars, and is used in many forms of racing to conserve fuel or energy. By following very closely behind another competitor's vehicle, drivers have reported feeling as if they were being *pulled along* by the vehicle in front, and in fact had to reduce the throttle level to avoid hitting the competitor. The reason for this phenomenon became clear upon observing the flow characteristics in the wake of the racecar model in Figure 7.6.

Figure 7.7 shows a detailed view of the wake region behind the model, with all of the vectors

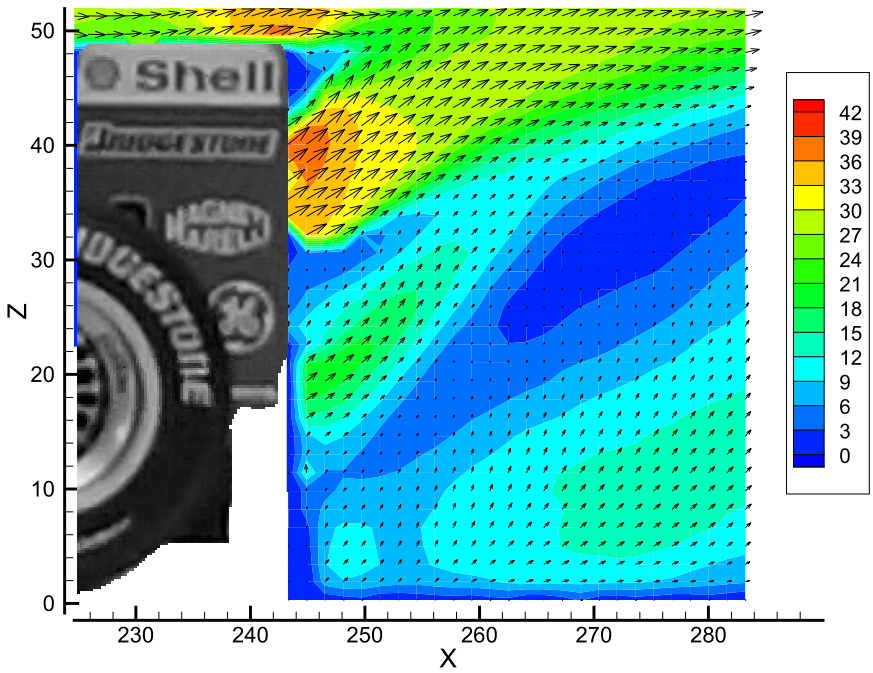

Figure 7.7: Detailed view of the average velocities measured in the wake of the racecar model (vertical plane along the centreline, in m/s) Note: All axis dimensions in mm

included. In the region where the nose of a following racecar would be (below $Z \approx 35$), the average resultant velocity was 10 m/s, pointed upwards at 45° from the horizontal. Considering only the horizontal (X-direction) component of that velocity, the incident air speed on the nose of a following racecar would only be 7 m/s. Therefore, while the racecar in the lead must overcome the drag force associated with a 40 m/s air flow, the following racecar needs only to overcome a drag force due to a 7 m/s air flow (at least over the first third of its length). This is clearly a large advantage, considering that the drag forces increase with the square of velocity. It is important to note here that ground plane was stationary in all experiments performed here, and that the addition of a moving ground plane could result in higher X-direction velocities.

Another common phenomenon felt by the driver of a draughting racecar, is the sensation of very

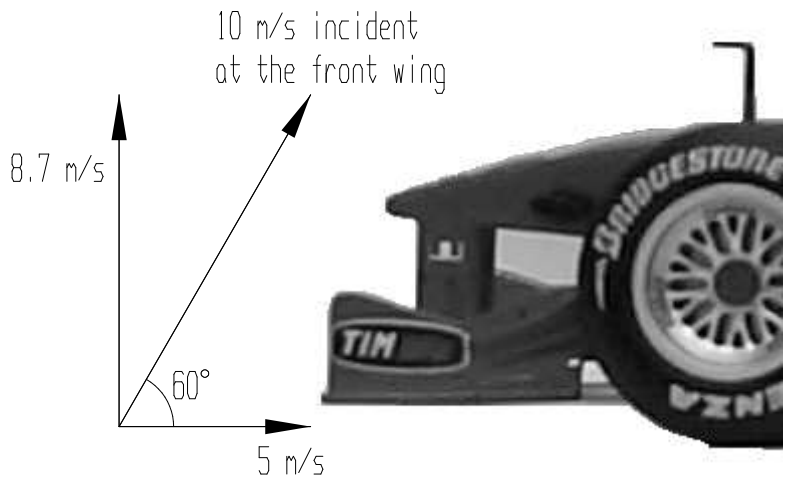

Figure 7.8: Velocities incident on the front wing of a following racecar

little grip at the front (steering) wheels, or impeded ability to turn the racecar. This can again be explained by observing the velocities in the wake region of Figure 7.7. In the region where the front wing of a following racecar would lie (below $Z \approx 15$), the average resultant velocity was 10 m/s, pointed upwards at an angle of 60° above the horizontal. This means that the front wing could only produce downforce with an incident (X-direction) velocity of 5 m/s. As well, the vertical component of the incident velocity was 8.7 m/s (Figure 7.8). This is a significant amount of upwards flow which could result in small amounts of lift being generated at the front wing of the following racecar, decreasing even further the net amount of downforce generated.

Plane of the Wheels

Figure 7.9 shows the average resultant velocities obtained in the plane over the wheels of the racecar model (at Y = -37mm in Figure 7.3 (b)). A picture of the model was again superimposed on the velocity data (note that the only areas shown were those in front of the light sheet).

As expected, the main effects in this plane were caused by the front and rear wheels of the racecar model. As the flow reached the front wheel, it was forced to accelerate around its upper surface,

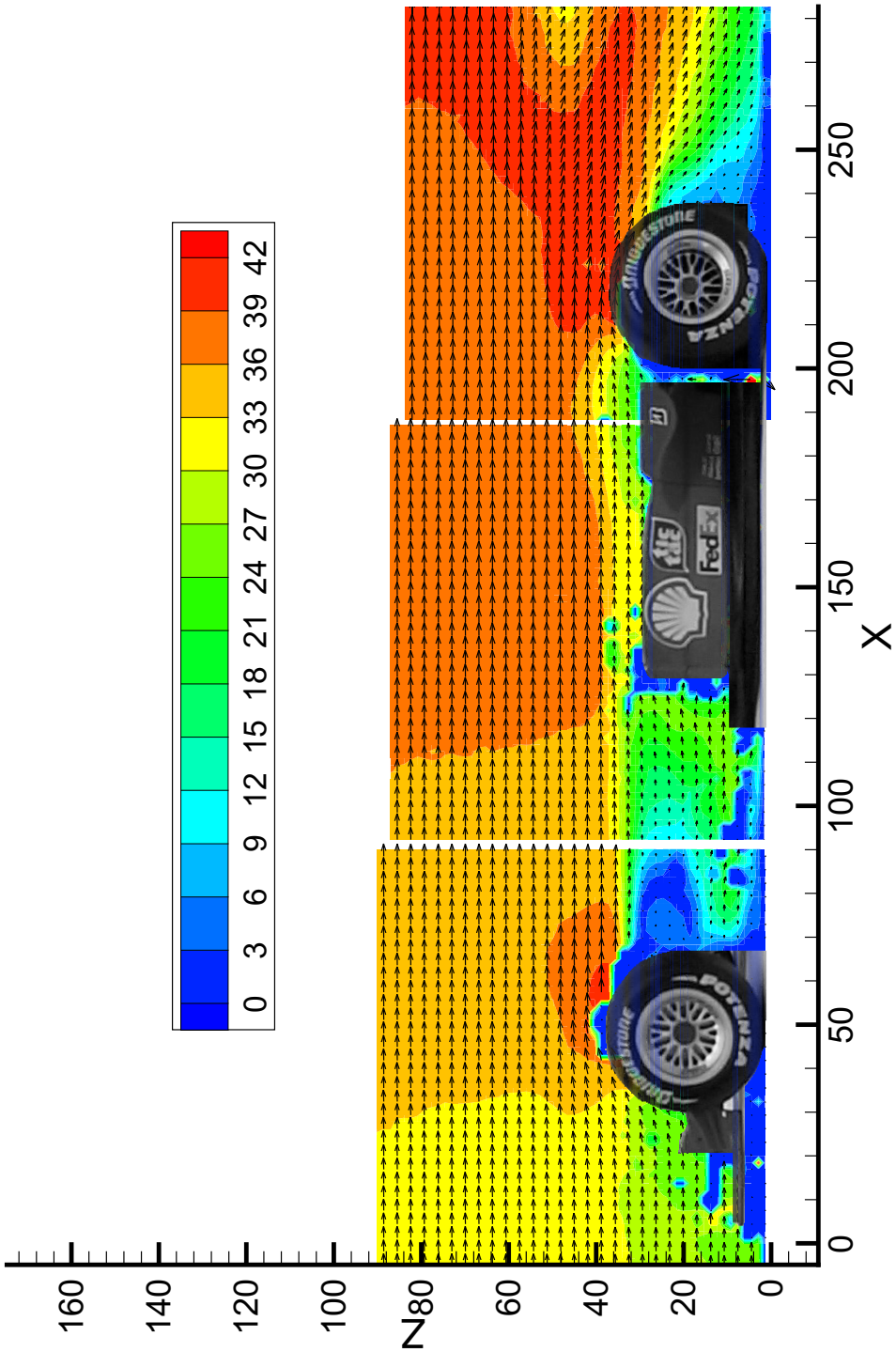

Figure 7.9: Average velocities measured in the vertical plane along the wheels of the racecar model (in m/s) Note: All axis dimensions in mm, some vectors removed for clarity

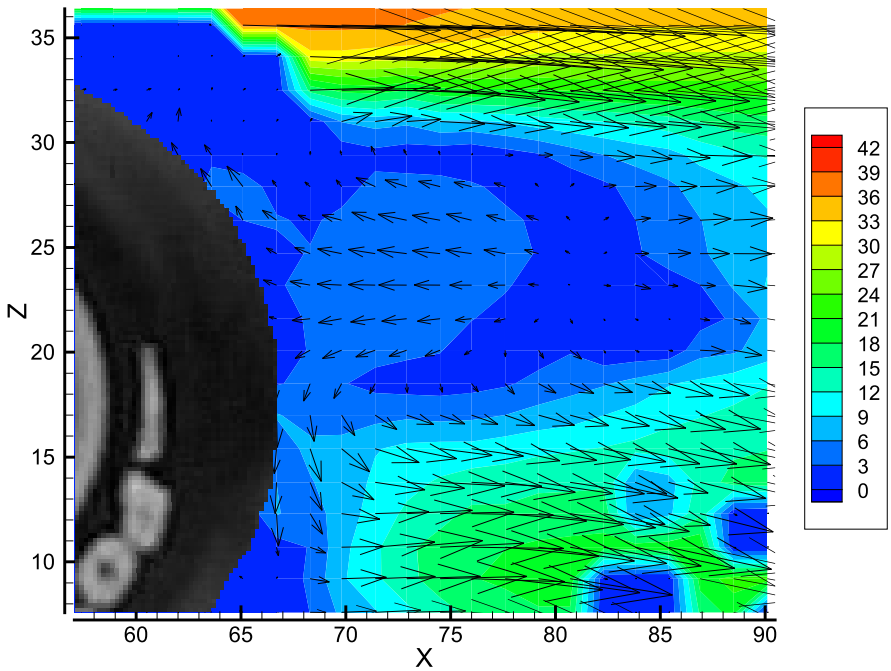

Figure 7.10: Detailed view of the average velocities measured in the wake of the front wheel of the racecar model (vertical plane along the wheels, in m/s) Note: All axis dimensions in mm

resulting in high velocities in the region of $X, Z \approx 58{,}40$. Behind the front wheel, a unique flow pattern was observed. Figure 7.10 shows a detailed view of the region directly behind the front wheel with the vector lengths increased for visibility. At the top of the wake region in Figure 7.10, severe flow reversal was observed between $Z = 20$ and $Z = 28$, with velocities reaching -5.5 m/s (flowing to the left). This area of reverse flow appeared to originate in the area of $81 < X < 83$, however there was no distinct origin in this area. This indicated that the flow in this area was highly three dimensional, and that the flow reversal was most likely due to out-of-plane velocities. This area will be revisited in the following section, where the velocities were measured in the horizontal plane.

It was important to note that for the results presented above, the wheels of the model were

not spinning, resulting in a somewhat idealized condition. With the wheels spinning counter clockwise, the upper surface of the wheel would have experienced earlier flow separation [73]. This reduced flow attachment (over the rotating wheels) could ultimately result in increased drag due to the four wheels.

7.5 Horizontal Plane Measurements - Formula One Racecar

7.5.1 Objective

The main objective of the experiments presented in this section was to extend the PIV measurements to the horizontal plane, further characterizing the flow over the racecar model. Two complete horizontal ($X - Y$) planes were measured, with the first located at the wheel (or axle) centreline, and the second located along the driver's helmet and the rear view mirrors.

7.5.2 PIV Setup - Formula One Racecar - Horizontal Plane

Figure 7.11 (a) shows the PIV setup utilized to obtain a horizontal measurement plane (with respect to the racecar model). In Figure 7.11 (b) the locations of the two measurement planes are shown, with the first located at $Z = 17.5mm$, and the second located at $Z = 35.5mm$. The first plane would show the behaviour of the air flow around the wheels and sidepods of the model, while the second plane would show the flow patterns around the cockpit and over the nose and rear bodywork of the model.

As with the vertical plane measurements, three PIV measurement windows $100mm$ x $100mm$ in size were used to view one plane over the entire length of the racecar model. A common origin and calibration technique was used in order to easily join the three measurement areas after processing. These calibration images were shown in Figures 7.12 (a to c) and 7.13 (a to c).

In each of the six measurement windows (forming the two complete $X - Y$ planes), 250 image pairs were collected at a time separation (Δt) of 14 μs between images. As for the vertical

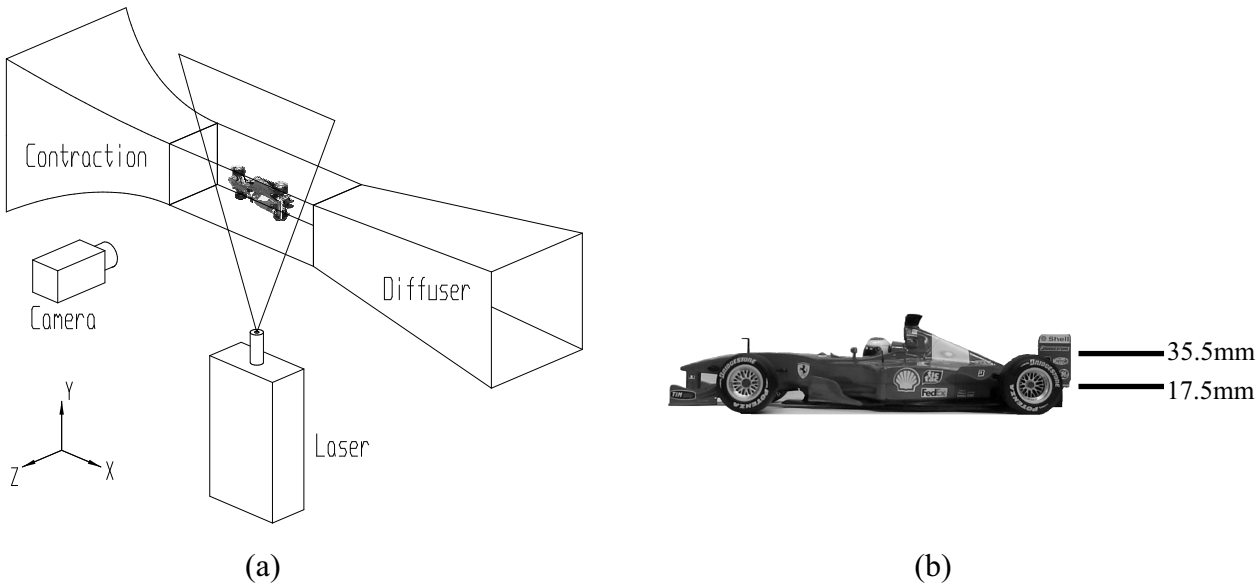

Figure 7.11: PIV setup used in the horizontal plane measurements performed on the Formula One racecar model, (a) hardware setup (b) location of measurements planes

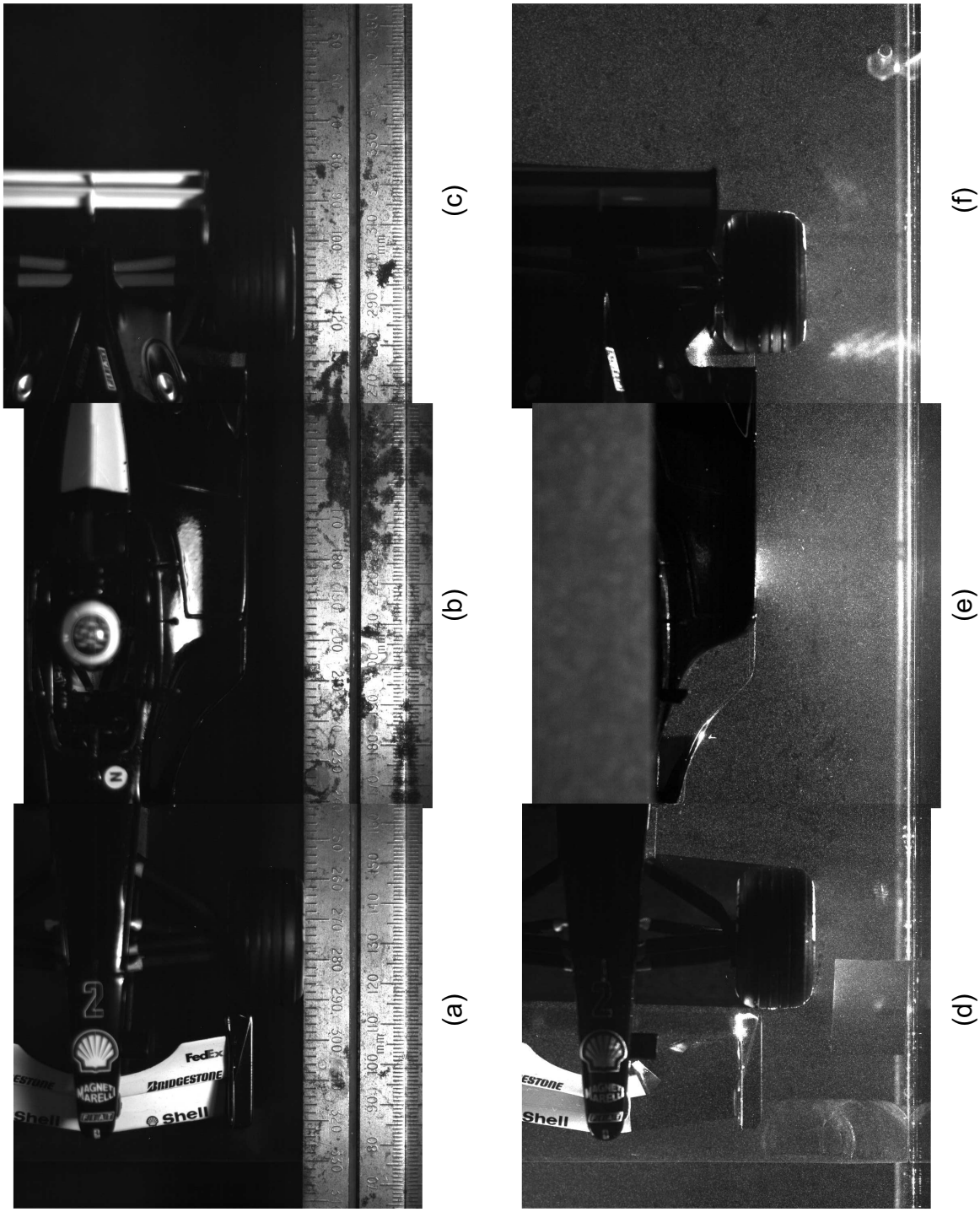

Figure 7.12: Calibration (a to c) and sample PIV images (d to f) obtained in the horizontal plane measurements over the racecar model (wheel centreline)

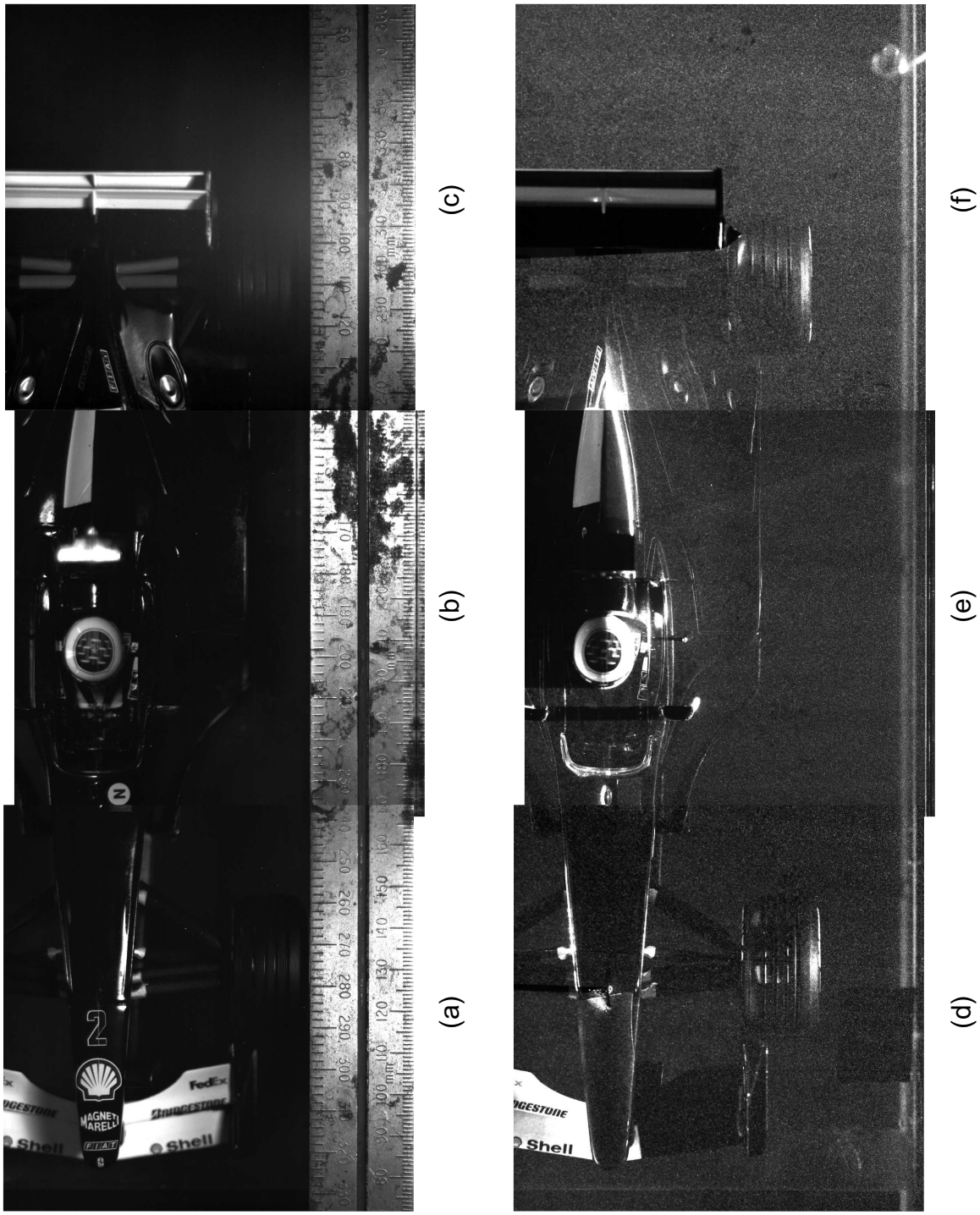

Figure 7.13: Calibration (a to c) and sample PIV images (d to f) obtained in the horizontal plane measurements over the racecar model (in the plane of the driver's helmet)

plane measurements, cross correlation was performed using 32 x 32 pixel ($3.17mm$ x $3.17mm$) interrogation areas with 50% overlap. This resulted in 3,844 (62 x 62) vectors in each area (or 11,532 vectors over one complete measurement plane).

In Figures 7.12 (d through f) and 7.13 (d through f), sample PIV images are shown, each one corresonding to the calibration image above it. As was the case with the vertical plane measurements, several challenges arose here when performing the PIV measurements. For example, in the first measurement window (Figure 7.12 (d)), the entire top surface of the front wing had to be covered in black electrical tape in order to allow for the distinction of seeding particles passing over the white surface of the wing. The front wheel of the racecar model also created a large shadow behind it (in the area of the racecar suspension), resulting in the loss of all velocity data in this area. In this case, the laser was positioned such that the shadowed area would be minimized.

In Figure 7.12 (e), the entire area of the cockpit (driver's helmet, rear view mirrors *etc.*) was found to be extremely reflective. Even though there were no measurements to be made in that location, the area was blocked from view of the camera by placing a piece of masking tape on the test section window. This was to prevent the overexposure of those pixels in the CCD array of the camera due to the high laser light intensity.

In Figure 7.13 (d through f), most of the measurement area was above the racecar model. Even though most of the model could be seen underneath the measurement plane, useful velocity data was still retrieved in the majority of these areas. For example, in Figure 7.13 (d), the nose, front wheel, and suspension arms of the racecar could all be seen in the PIV images. However, the seeding particles could still be distinguished. This was a clear indication of the robustness of the PIV cross correlation technique. The main observation made here was that it is not always necessary to have a flat black background in a PIV image to ensure strong cross correlation. Instead, it is essential to obtain a PIV image where the seeding particles can be distinguished, regardless of what is behind the measurement plane. If the seeding particles can be seen clearly to move from one image to the next with the naked eye, it is highly likely that this motion will be captured during cross correlation.

7.5.3 Results - Formula One Racecar - Horizontal Plane

Wheel Centreline

Figure 7.14 shows the average resultant velocities measured at the centreline of the wheels in the horizontal plane. The origin of the $X - Y$ coordinate system in all of the following plots was placed at the tip of the racecar's nose. The three measurement windows were joined together to show a complete picture of the flow field over the model. As with the vertical plane results, the model was superimposed on the contour plots to provide a visual reference of the boundaries of the flow field.

At the front of the model in Figure 7.14, some velocity data was captured over the front wing (which was therefore removed from view). The front wing was responsible for directing the incoming flow upwards (in the Z-direction) as was demonstrated by the lower velocities near the front of the wheel (*i.e.* a significant amount of flow coming out of the page was expected in this region). In the region surrounding $X, Y = 51$,-59, the flow accelerated around the outside of the front wheel. It was important to recognize here that much of this acceleration was caused by the test section wall, and would not have been as pronounced over the full scale model.

Behind the front wheel, a wake region was formed by air flow around both the inside and outside of the wheel due to the streamlined design of the suspension. This wake area is viewed in more detail in Figure 7.15 to reveal the third velocity component from Figure 7.10. Based on the flow patterns seen in these two figures, it was reasonable to assume that the reverse flow seen in Figure 7.10 was caused by the flow around the inside of the wheel in Figure 7.15 ($Y > -34mm$). The flow around the inside of the wheel had a higher tendency to reverse itself and fill the wake region as it exited the suspension area at a lower velocity than the flow around the outside of the wheel (approximately 23 m/s versus 37 m/s around the outside of the wheel).

The flow upstream of the sidepods was largely affected by the barge boards of the racecar model (Figure 7.14). Their main purpose was to limit the amount of stagnation at the sidepod entrance by splitting the upstream flow, allowing one portion to enter the sidepods (and heat exchangers) while diverting the rest of the flow to the outside of the sidepod, reducing the overall drag in this

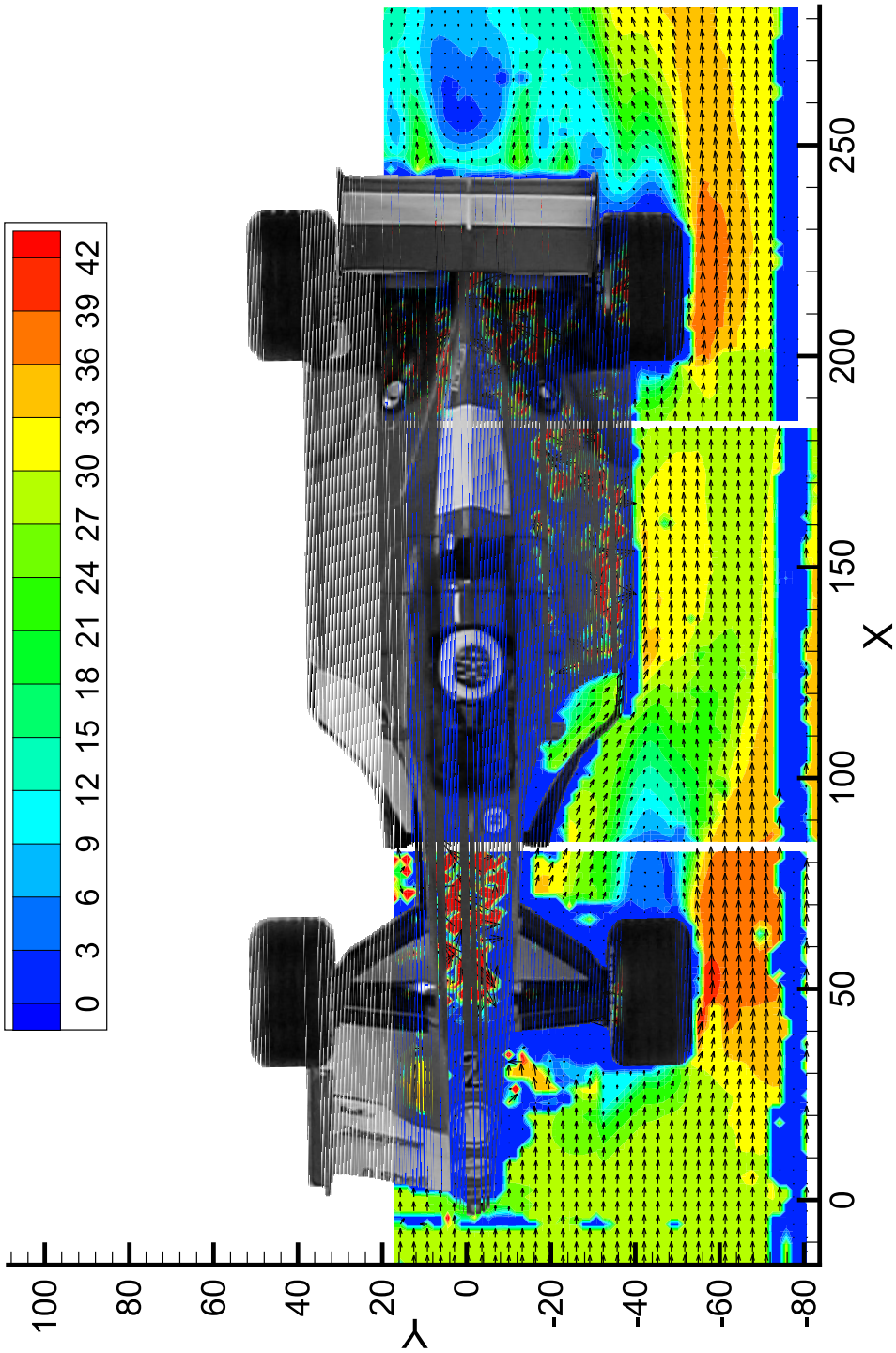

Figure 7.14: Average velocities measured in the horizontal plane along the wheel centreline of the racecar model (in m/s) Note: All axis dimensions in mm, some vectors removed for clarity

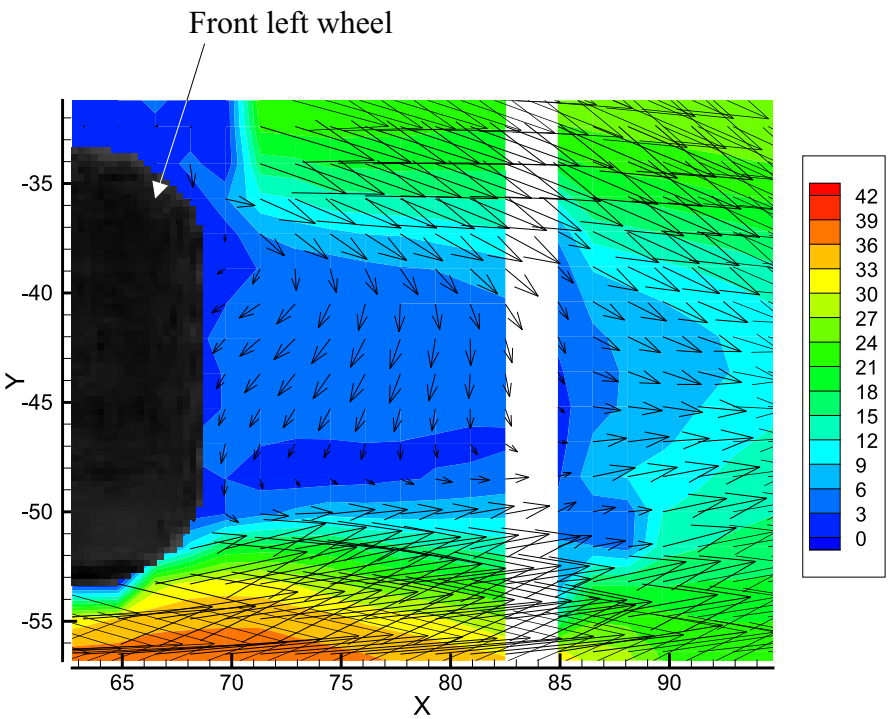

Figure 7.15: Detailed view of the average velocities measured in the wake of the front wheel of the racecar model (horizontal plane at the wheel centreline, in m/s) Note: All axis dimensions in mm

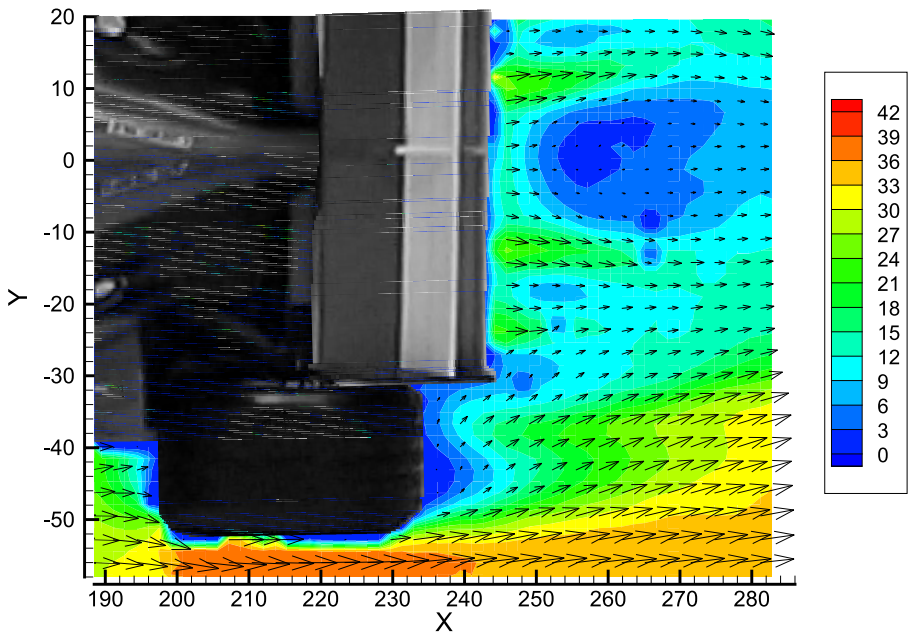

Figure 7.16: Detailed view of the average velocities measured in the wake of the racecar model (horizontal plane along the wheel centreline, in m/s) Note: All axis dimensions in mm

area. This was evident in the upstream flow, which was directed outward by the barge board (in the $-Y$ direction) resulting in a smoother transition to the outside of the sidepod.

A similar level of flow acceleration (as was observed around the front wheel) was seen around the outside of the rear wheel, which was again amplified by the test section wall in the near vicinity. The wake region behind the rear wing of the racecar model is shown in more detail in Figure 7.16. Behind the rear wheel, the flow began to be redirected towards the centreline of the racecar ($Y = 0$) to fill the low pressure area in the wake region. Investigation of these transverse (Y-direction) velocities suggested a stabilizing condition for a racecar following closely behind. When perfectly aligned with the racecar in front (*i.e.* both vehicles in the same Y position), there would be a balance of transverse (Y-direction) forces pushing on the end plates of the front wing. However, if

the following racecar became misaligned with the leading racecar, these forces would no longer be in balance, and there would be a net force acting to realign the following racecar. For example, at a model misalignment of $12mm$, 80% of the total transverse forces would be directed towards the centreline of the wake, attempting to realign the following racecar, leading to a reduced amount of control in the real situation.

A core of low velocities was found in the area surrounding X, Y = 258,0 in Figure 7.16, and this was found to correspond to the same core found in Figure 7.7 in the area of X, Z = 270,30. This area made up the majority of the wake area which was not affected by any of the rear wing elements.

Plane of the Driver's Helmet

The second horizontal plane of measurement was located in the vicinity of the driver's helmet, at $Z = 35.5mm$ (see Figure 7.11 (b)). The average resultant velocities were obtained from 250 image pairs in each of the three measurement windows, and are plotted in Figure 7.17.

Along the nose of the racecar model, the velocity data was only partly retrieved, as parts of the nose protruded into the laser sheet (*i.e.* the pitot probe and fins along the top edges of the nose). With the laser sheet less than $1mm$ above the front wheels, the flow could be seen to accelerate along the top surface of the wheel (in the vicinity surrounding X, Y = 50,-42). The small area of low velocity at X, Y = 60,-42 was caused by the redirection of the flow over the end plates of the front wing. In this area, the flow was pointed upwards (in the Z-direction) to promote smoother flow over the top of the wheel. This area therefore contained a significant out-of-plane velocity component which was not captured in Figure 7.17.

The air flow over the sidepods remained uniform until the rear wheel fairings were reached (X, Y = 190,-35). As with the front wing end plates, these fairings were designed to blend the incoming flow with the top surface of the wheel. Therefore, lower velocities were seen in this region of Figure 7.17 due to the presence of out-of-plane velocities. The remainder of the flow over the rear wheel remained significantly three dimensional, with a negative velocity component in the Z-direction (Figure 7.9).

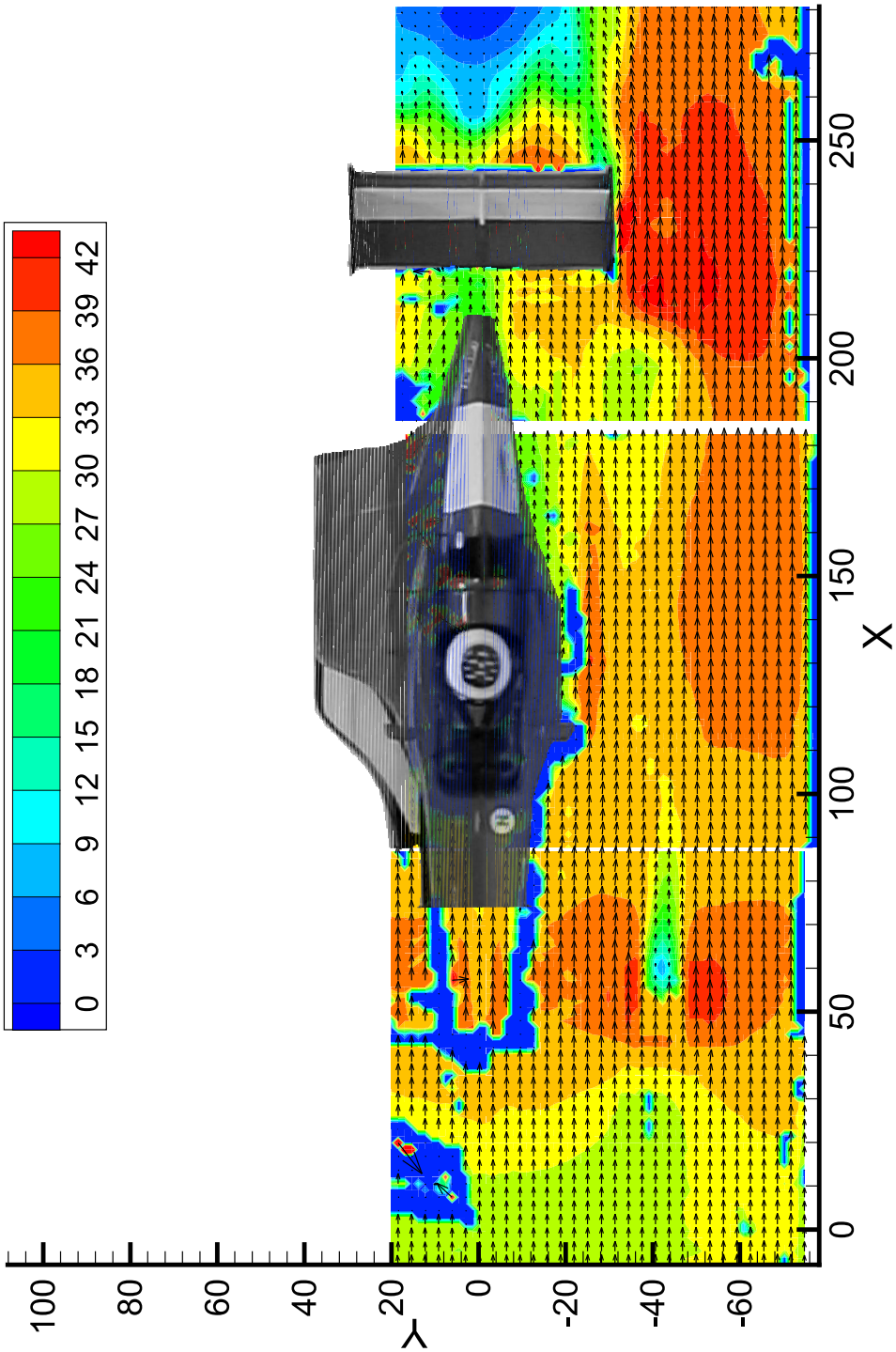

Figure 7.17: Average velocities measured in the horizontal plane around the racecar model in the plane of the driver's helmet (in m/s) Note: All axis dimensions in mm, some vectors removed for clarity

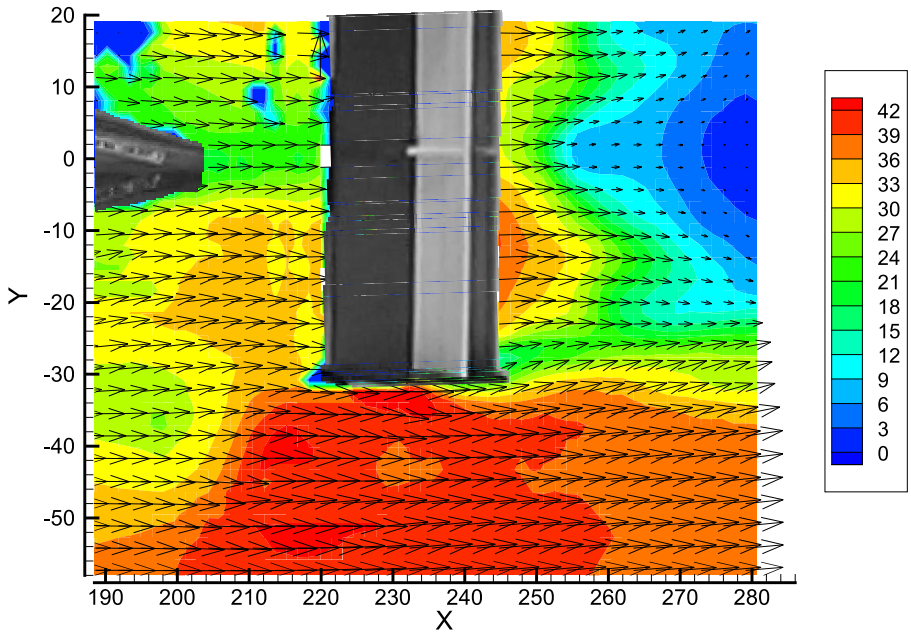

Figure 7.18: Detailed view of the average velocities measured in the wake of the racecar model (horizontal plane along the driver's helmet, in m/s) Note: All axis dimensions in mm

The flow downstream of the rear wing was re-plotted in higher detail in Figure 7.18 to show the flow behaviour in the wake region. In this plane, the flow towards the centreline of the model (around the edges of the rear wing) was not as prominent due to the absence of the rear wheels in this plane. The unique curvature of the lower rear wing element produced a stream of high exit velocities to either side of the model centreline (at $Y = \pm 14$). The core of low velocities observed in the vertical plane (Figure 7.7) is also seen in Figure 7.18 in the area surrounding $X, Y = 278{,}0$. As expected, this area was shifted further downstream (compared to Figure 7.16) since the measurement plane was $18mm$ higher than the previous horizontal plane located at the wheel centreline.

7.6 Summary and Conclusions

The flow over a 1:18 scale model of a Formula One racecar at an air speed of 40 m/s was measured using PIV. Four complete measurement planes were utilized, each one spanning the entire length of the $243mm$ model, as well as a further $40mm$ in the wake region behind the racecar.

In conducting the PIV measurements on the racecar model, an important conclusion was formulated with regards to the robustness of the PIV measurement technique. It was found that the degree of cross correlation was not as dependent on the image background as originally thought. More specifically, the absence of a uniform, flat black background in a PIV image did not necessarily result in erroneous, uncorrelated data (after cross correlation). Being able to visibly distinguish seeding particles over any sort of stationary background seemed to be the essential requirement for successful cross correlation.

In examining the flow over and around the Formula One racecar model, several conclusions were drawn with regards to its aerodynamic shape.

1. The racecar model carries numerous aerodynamic devices aimed at producing negative lift (downforce) including the front wing, front wing end plates, the upper and lower elements of the rear wing, and the rear diffuser. It was clear from the abundance of these devices that producing downforce was a major objective in the design of the racecar body.

2. The *dirtiest*, or most aerodynamically deficient components of the racecar were the four wheels and the rear wing. The wheels, which acted essentially as rotating, short circular cylinders, induced very low and in some cases, reverse velocities in their wake. Although the rear wing produced a significant percentage of the racecar's downforce, the large amounts of flow redirection resulted in a highly complex and unstable wake behind the racecar.

3. The wake behind the racecar model is an ideal area for a following racecar to gain an aerodynamic advantage. The horizontal velocities incident on the nose of a following racecar are reduced by over 80% due to the wake of the leading racecar. However, these incident velocities also carry a large vertical component which could potentially induce lift forces

at the front of the following vehicle, resulting in reduced mechanical grip and cornering abilities.

Chapter 8

Conclusions and Recommendations

8.1 Conclusions

In this study, a small scale, recirculating wind tunnel was designed to be used with the optical measurement technique of Particle Image Velocimetry (PIV). Following its custom fabrication, the wind tunnel was characterized using PIV in order to determine the quality of the flow in the test section. At this point, a square cylinder was inserted into the test section, and PIV measurements were performed on the flow over the cylinder and compared to previously published work. Following this experiment, PIV was again used to measure the flow over a 1:18 scale Formula One racecar in the wind tunnel test section. From these combined projects, four major conclusions were formed regarding the application of PIV in a small scale wind tunnel and are presented below.

8.1.1 Wind Tunnel Contraction Design

The topic of wind tunnel contractions was explored in Chapter 2, and a novel contraction geometry was designed to be used in the wind tunnel in this study. Based on CFD simulations performed

in Chapter 2, this novel geometry provided improved velocity, pressure, and turbulence characteristics over six conventional contraction shapes. Once fabricated, the flow validation results of Chapter 5 verified the performance of the contraction (and the rest of the wind tunnel). The measured test section flow had 1.8% variation in longitudinal velocity, 2.0% turbulence intensity, less than 0.3^o of misalignment, and a boundary layer not exceeding $6.5mm$.

8.1.2 Compatibility/Usability of the Wind Tunnel/PIV Combination

The experiments performed in Chapters 5, 6, and 7 illustrated the ease of use of the wind tunnel/PIV system in this study. In these three chapters, a total of 48 different PIV tests were conducted, all without any major impediments. The table-top configuration of the wind tunnel allowed for convenient set up of the PIV laser and camera, while the adjustability of the fan speed allowed for very quick changes in Reynolds number. It was concluded as a general guideline that a $1m$ space around the wind tunnel would provide sufficient room for the PIV hardware, and access to the seeding particle generator, speed control unit, and test section for model setup and calibration.

8.1.3 Performance of the Wind Tunnel/PIV Combination

In order to gauge the performance of the wind tunnel/PIV system used in this study, the air flow over a known geometry was measured and compared to previous results. This was the aim of Chapter 6, where a square cylinder was placed in the test section, and the flow was measured at a Reynolds number of 21,400. The results of these experiments compared favourably to the LDV results of Durao [68], McKillop and Durst [69], and Lyn *et al.* [66, 67], whose results differed by an average of 10% from the new mean velocity measurements and turbulence statistics. These results gave confidence in the accuracy of the wind tunnel and PIV system in reproducing a flow field of known characteristics.

8.1.4 Versatility of the Wind Tunnel/PIV Combination

In Chapter 7, a 1:18 scale Formula One racecar model was used to produce a highly complex flow field and diverse measuring conditions in order to push the limits of measurement with the PIV system. The elaborate geometry and reflective surfaces of the racecar model tested the versatility of the PIV measurement system in retrieving velocity information from less than optimal backgrounds and contrast levels. At the time of writing, there appears to be no other measurement technique capable of collecting this type of velocity information. Based on the abundance of data gathered in the results of Chapter 7, the wind tunnel/PIV system showed a high level of versatility and provided further confidence in its usefulness for testing even more complex flows.

In summary, it is the opinion of the author that particle image velocimetry is a measurement technique that is extremely compatible for use in wind tunnels, provided the wind tunnel is small enough, and that its non-intrusive nature indeed makes it one of the best choices for wind tunnel velocity measurements. PIV can also be confidently used in calibrating a newly fabricated wind tunnel, as was shown in Chapter 5. As the levels of technology in this field increase, digital cameras which contain larger CCD pixel arrays, will allow for larger measurement areas, making PIV a more feasible measurement technique in large wind tunnels as well.

8.2 Recommendations

Throughout the design, fabrication, and use of the wind tunnel in this study, several opportunities for improvement were identified, and are given below as recommendations for future work.

8.2.1 Operational Improvements to the Present Wind Tunnel

The recommendations made in this section are aimed at improving the operation of the wind tunnel used in this study.

1. Test Section Modification - Modifications to the test section could make it more easily removable and accessible. For example, mounting one of the four test section walls on hinges would allow for quick access to models inside the wind tunnel, reducing calibration times. The main challenge in doing this is ensuring proper sealing of the test section (in the absence of fasteners), and doing so without compromising the interface between the contraction and diffuser sections.

2. Hinged Panel for Smoke Venting - By adding a hinged panel to the wind tunnel (in a location other than the test section), the smoke used for seeding particles in PIV can be easily vented from the wind tunnel at the completion of an experiment. Any remaining smoke will eventually condense back into mineral oil and deposit itself inside the wind tunnel. It is therefore important to remove as much of this smoke as possible to prevent excessive amounts of oil from collecting in vulnerable areas such as the fan motor internals. For the measurements in this study, one of the acrylic panels on the settling chamber was removed for this purpose. This same panel could be modified to open on hinges, simplifying the process.

3. Implementation of a Data Acquisition System - The operation of the wind tunnel can be further improved by utilizing a data acquisition system to monitor such parameters as air temperature, fan rotational speed, and fan load. The variable frequency drive (used to control the fan speed, as discussed in Section 3.6) is capable of generating analog outputs proportional to speed and electrical load. Details on the analog and digital outputs available from the variable frequency drive unit can be found in [74]. These and other parameters can be fed to a central data acquisition system such as the Keithley 2700 Multimeter/Data Acquisition System used in the temperature measurements of Section 5.7.

8.2.2 Further Design Projects

The recommendations in this section provide ideas for design projects intended to either improve or expand the use of the current wind tunnel in this study.

1. Testing of Contraction Designs - The one major recommendation regarding the design of the wind tunnel contraction was to verify the CFD simulation results from Chapter 2 with experimental data. This could be done by fabricating one or more of the contraction designs considered in Chapter 2, and installing them on the wind tunnel. Since all contractions were designed with the same length, each test would require a simple exchange of the contraction, followed by the characterization and comparison of the exiting flow.

2. Design of a Force Balance - When performing wind tunnel tests, it is often desirable to directly measure the drag force exerted on the test model. This can be achieved with the design of a force balance mechanism to be used in the test section. With a typical force balance system, the model is mounted to an aerodynamically streamlined post which passes through a test section wall to a fixed base. The drag and lift forces exerted on the model can then be measured at the base of the post with scales, load cells, or spring systems, *etc.* It would then be possible to directly compare the measured drag force with the drag force calculated from the integration of velocity profiles determined with PIV.

3. Design of Alternate Test Section and Diffuser Combinations - In the wind tunnel designed for this study, a relatively long test section and short diffuser was used to allow for the potential testing of long models. For most tests however, it is sufficient to have a shorter test section. The design and fabrication of a shorter test section (with a correspondingly lengthened diffuser section) would reduce the flow losses in the tunnel, possibly resulting in higher achievable wind speeds.

8.2.3 Further Experimental Projects

In this section, various projects are proposed to experimentally improve the wind tunnel operation without the redesigning of any components.

1. Turning Vane Adjustment - PIV measurements in the settling chamber (as in Chapter 5), could be used to guide the adjustment of individual turning vanes in corner 2 to improve the flow characteristics entering the contraction section. From the results of Section 5.3.3,

there was a considerable amount of variation in the velocity profile due to the fan, as well as $\pm 3^o$ of misalignment in some areas. Adjustment of the corner 2 turning vanes could provide a more uniform, well aligned flow which would improve the test section flow quality.

2. Screen and Honeycomb Sections - Further improvements to the wind tunnel performance could be achieved with the experimentation in the use and location of various screens and honeycomb sections. For example, screens with varying porosity (cell size) could be tested to maximize the turbulence reduction while minimizing the amount of consequent pressure drop. The same can be done with honeycomb sections of varying cell size. As well, the location and number of screens and honeycomb sections can be explored to gain further turbulence reduction without excessive pressure losses.

3. Fan Blade Adjustment - The wind tunnel fan used in this study allows for adjustment of the angle of attack of the blades. For the fan requirements outlined in Chapter 2, the angle of attack of each blade was set at 27°. A possible experimental project would involve the adjustment of the angle of attack of the fan blades to increase either the available flowrate or static pressure rise. It is highly recommended that if the blade angles are modified, the fan should be properly balanced by the manufacturer or suitable axial fan establishment. Fan performance curves from Enviro-Tech HVAC Products (Ancaster, Ontario) have been included in Appendix A.

8.2.4 Improvement of the PIV System

Throughout all the experiments performed in this study, there were no major deficiencies encountered in the PIV measurement system. The one recommendation made here involves a possible improvement to the system by reducing the required setup and calibration time.

1. PIV Traversing System - A traversing system is commonly used with LDV systems, as the measurement area is extremely small (on the order of a few millimetres). Such a system would also be beneficial to the efficiency of PIV measurements. Figure 8.1 shows a concept sketch where the laser and camera are held rigidly with respect to each other. Once the

camera has been focused properly on the laser light sheet, the entire assembly can be moved by a known distance in any direction and immediately begin collecting focused PIV images. This type of system would be ideal for the wind tunnel in this study since the test section volume is quite large compared to the average size PIV measurement window (one entire plane in the test section could require as many as 10 PIV measurement windows). With a traversing assembly, the PIV system would only require calibration of the first measurement window, and the entire test section could be covered with that one setup. A second setup, where the laser and camera positions were exchanged, would then capture the third velocity component, fully characterizing the test section flow in only two setups. The method of traversing could be as simple as a system of graduated acme screws to move the assembly of Figure 8.1 over a solid base.

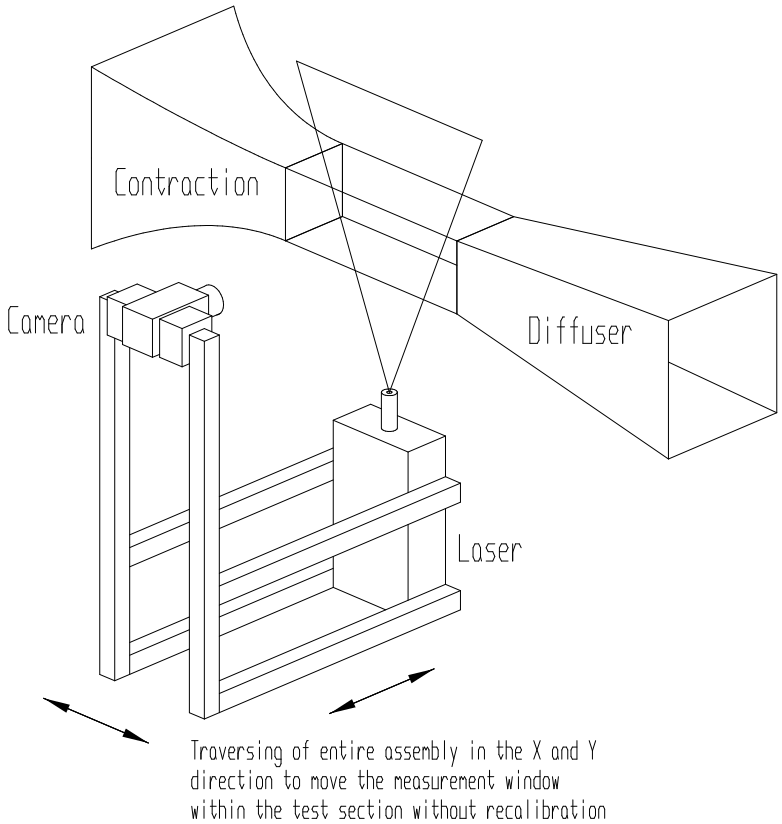

Figure 8.1: A traversing system to reduce the amount of required setup time for PIV measurements

References

[1] A. Pope and W. H. Rae, *Low-Speed Wind Tunnel Testing.* New York: John Wiley & Sons, 1984.

[2] A. Pope, W. H. Rae, and J. Barlow, *Low-Speed Wind Tunnel Testing.* New York: John Wiley & Sons, 1999.

[3] R. Pankhurst and D. Holder, *Wind-Tunnel Technique.* London: Sir Isaac Pitman & Sons, 1952.

[4] B. Sperandei, R. Gilbert, and D. A. Johnson, "Analysis of the flow through a vented automotive brake rotor." To be published in ASME Journal of Fluid Mechanics, March 2003.

[5] B. Sahin, A. J. Ward-Smith, and D. Lane, "The pressure drop and flow characteristics of wide-angle screened diffusers of large area ratio," *Journal of Wind Engineering and Industrial Aerodynamics*, vol. 58, pp. 33–50, 1995.

[6] M. M. Seltsam, "Experimental and theoretical study of wide-angle diffuser flow with screens," *AIAA Journal*, vol. 33, pp. 2092–2100, 1995.

[7] G. Gan and S. B. Riffat, "Measurement and computational fluid dynamics prediction of diffuser pressure-loss coefficient," *Applied Energy*, vol. 54, pp. 181–195, 1996.

[8] C. Farell and L. Xia, "A note on the design of screen-filled wide-angle diffusers," *Journal of Wind Engineering and Industrial Aerodynamics*, vol. 33, pp. 479–486, 1990.

[9] R. D. Mehta, "The aerodynamic design of blower tunnels with wide-angle diffusers," *Progress in Aerospace Science*, vol. 18, pp. 59–120, 1984.

[10] G. J. Klein, K. F. Tupper, and J. J. Green, "The design of corners in fluid channels," *Canadian Journal of Research*, vol. 3, pp. 272–285, 1930.

[11] B. Lindgren, J. Osterlund, and A. Johansson, "Measurement and calculation of guide vane performance in expanding bends for wind-tunnels," *Experiments in Fluids*, vol. 24, pp. 265–272, 1998.

[12] T. Morel, "Design of two-dimensional wind tunnel contractions," *Journal of Fluids Engineering, ASME Transactions, Series I*, vol. 99, pp. 371–378, 1977.

[13] M. Mikhail, "Optimum design of wind tunnel contractions," *AIAA Journal*, vol. 17, pp. 471–477, 1979.

[14] J. H. Downie, R. Jordinson, and F. H. Barnes, "On the design of three-dimensional wind tunnel contractions," *Aeronautical Journal*, vol. 88, pp. 287–295, 1984.

[15] E. G. Tulapurkara and V. V. K. Bhalla, "Experimental investigation of Morel's method for wind tunnel contractions," *Journal of Fluids Engineering*, vol. 110, pp. 45–47, 1988.

[16] Y. X. Su, "Flow analysis and design of three-dimensional wind tunnel contractions," *AIAA Journal*, vol. 29, pp. 1912–1920, 1991.

[17] F. M. Fang, "A design method for contractions with square end sections," *Journal of Fluids Engineering*, vol. 119, pp. 454–458, 1997.

[18] J. Callan and I. Marusic, "Effects of changing aspect ratio through a wind-tunnel contraction," *AIAA Journal*, vol. 39, pp. 1800–1803, 2001.

[19] G. E. Chemielewski, "Boundary-layer considerations in the design of aerodynamic contractions," *Journal of Aircraft*, vol. 11, pp. 435–438, 1974.

[20] S. M. Batill and J. J. Hoffman, "Aerodynamic design of three-dimensional subsonic wind tunnel inlets," *AIAA Journal*, vol. 24, pp. 268–269, 1984.

[21] B. Munson, D. Young, and T. Okiishi, *Fundamentals of Fluid Mechanics.* New York: John Wiley & Sons, 2002.

[22] G. D. Stubley, *ME 566: Spring 2001 Computational Fluid Dynamics for Fluids Engineering Design.* University of Waterloo, Waterloo, Ontario, 2001. Course notes.

[23] AEA Technology Engineering Software Limited, Waterloo, Canada, *CFX-TASCflow Theory Documentation Version 2.11.1*, 2001.

[24] A. B. Strong, *Notes for ME 664 Turbulence.* University of Waterloo, Waterloo, Ontario, 1996.

[25] D. DeVahl, *The Flow of Air Through Wire Screens, Hydraulics and Fluid Mechanics.* New York: Pergamon, 1964.

[26] L. Prandtl, "Attaining a steady air stream in wind tunnels," *NACA TM 726*, vol. October, 1933.

[27] H. Dryden and G. Schubauer, "The use of damping screens for the reduction of wind tunnel turbulence," *JAS*, vol. 14, pp. 221–228, 1947.

[28] I. Shames, *Mechanics of Fluids.* New York: McGraw-Hill, 1992.

[29] W. Eckert, K. Mort, and J. Jope, "Aerodynamic design guidelines and computer program for estimation of subsonic wind tunnel performance," *NASA TN D-8243*, vol. October, 1976.

[30] F. Wattendorf, "Factors influencing the energy ratio of return flow wind tunnels," in *The Fifth International Congress for Applied Mechanics*, (Cambrige, U.K.), September 12-16 1938.

[31] I. Idel'chik, *Handbook of Hydraulic Resistance.* Moscow: Begell House, Inc., 1966.

[32] R. P. Benedict, *Fundamentals of Temperature, Pressure, and Flow Measurements, 3rd ed.* New York: Wiley & Sons, 1984.

[33] R. I. Soloukhin, C. W. Curtis, and R. J. Emrich, "Measurement of pressure," *Methods of Experimental Physics*, vol. 18, 1981.

[34] A. J. Smits and T. T. Lim, *Flow Visualization: Techniques and Examples*. London: Imperial College Press, 2000.

[35] Dantec Measurement Technology, *FlowMap Particle Image Velocimetry Instrumentation, Installation and User's Guide*, 1999.

[36] A. Basset, *Treatise on Hydrodynamics vol II*. London: Deighton, Bell & Co, 1888.

[37] J. O. Hinze, *Turbulence*. New York, USA: McGraw-Hill, 2nd ed., 1975.

[38] A. Melling, "Tracer particles and seeding for particle image velocimetry," *Meas. Sci. Technol.*, vol. 8, pp. 1406–1416, 1997.

[39] I. Grant, "Particle image velocimetry: a review," *Proc. Instn. Mech. Engrs.*, vol. 211, pp. 55–76, 1997.

[40] R. A. D. Gilbert, "Evaluation of FFT based cross-correlation algorithms for particle image velocimetry," Master's thesis, University of Waterloo, Waterloo, Canada, 2001.

[41] C. E. Willert and M. Gharib, "Digital particle image velocimetry," *Experiments in Fluids*, vol. 10, pp. 181–193, 1991.

[42] R. D. Keane and R. J. Adrian, "Theory of cross-correlation analysis of PIV images," *Applied Scientific Research*, vol. 49, pp. 191–215, 1992.

[43] R. J. Adrian, "Particle-imaging techniques for experimental fluid mechanics," *Annu. Rev. Fluid Mech.*, vol. 23, pp. 261–304, 1991.

[44] M. Raffel, C. Willert, and J. Kompenhans, *Particle Image Velocimetry – A Practical Guide*. Berlin, Germany: Springer, 1998.

[45] M. Muste, Z. Xiong, A. Kruger, and I. Fujita, "Error estimation in PIV applied to large-scale flows," in *The 3rd International Workshop on PIV'99*, (Santa Barbara, USA), September 1999.

[46] C. J. D. Pickering and N. A. Halliwell, "Laser speckle photography and particle image velocimetry: photographic film noise," *Applied Optics*, vol. 23, pp. 2961–2969, 1984.

[47] A. K. Prasad, R. J. Adrian, C. C. Landreth, and P. W. Offutt, "Effect of resolution on the speed and accuracy of particle image velocimetry interrogation," *Experiments in Fluids*, vol. 13, pp. 105–116, 1992.

[48] R. J. Adrian, "Dynamic ranges of velocity and spatial resolution of particle image velocimetry," *Meas. Sci. Technol.*, vol. 8, pp. 1393–1398, 1997.

[49] H. Huang, D. Dabiri, and M. Gharib, "On errors of digital particle image velocimetry," *Meas. Sci. Technol.*, vol. 8, pp. 1427–1440, 1997.

[50] Y. G. Guezennec and N. Kiritsis, "Statistical investigation or errors in particle image velocimetry," *Experiments in Fluids*, vol. 10, pp. 138–146, 1990.

[51] S. K. Sinha, "Improving the accuracy and resolution of particle image or laser speckle velocimetry," *Experiments in Fluids*, vol. 6, pp. 67–68, 1988.

[52] M. L. Jakobsen, T. P. Dewhirst, and C. A. Greated, "Particle image velocimetry for predictions of acceleration fields and force within fluid flows," *Meas. Sci. Technol.*, vol. 8, pp. 1502–1516, 1997.

[53] A. Boillot and A. K. Prasad, "Optimization procedure for pulse separation in cross-correlation PIV," *Experiments in Fluids*, vol. 21, pp. 87–93, 1996.

[54] H. T. Huang and H. E. Fiedler, "Deformed particle image pattern matching in particle image velocimetry," *Applied Scientific Research*, vol. 51, pp. 179–183, 1993.

[55] J. Westerweel, "Fundamentals of digital particle image velocimetry," *Meas. Sci. Technol.*, vol. 8, pp. 1379–1392, 1997.

[56] R. Hocker and J. Kompenhans, "Some technical improvements of particle image velocimetry with regard to its application in wind tunnels," in *International Congress on Instrumentation in Aerospace Simulation Facilities*, (New Jersey, USA), September 1989.

[57] C. Willert, M. Raffel, and J. Kompenhans, "Recent applications of particle image velocimetry in large-scale industrial wind tunnels," in *Proceedings of the 1997 17th IEEE International*

Congress on Instrumentation in Aerospace Simulation Facilities, (Pacific Grove, USA), October 1997.

[58] C. Willert, "Stereoscopic digital particle image velocimetry for application in wind tunnel flows," *Meas. Sci. Technol.*, vol. 8, pp. 1465–1479, 1997.

[59] K. D. Hinsch, "Three-dimensional particle velocimetry," *Meas. Sci. Technol.*, vol. 6, pp. 742–753, 1995.

[60] J. Westerweel and F. T. M. Nieuwstadt, "Performance tests on 3-dimensional velocity measurements with a two-camera digital particle-image velocimeter; Laser Anemometry Advances and Applications vol 1, ed A. Dybbs and B. Ghorashi," 1991.

[61] M. P. Arroyo and C. A. Greated, "Stereoscopic particle velocimetry," *Meas. Sci. Technol.*, vol. 2, pp. 1181–1186, 1991.

[62] A. K. Prasad and A. J. Adrian, "Stereoscopic particle image velocimetry applied to liquid flows," *Exp. Fluids*, vol. 15, pp. 49–60, 1993.

[63] M. Gaydon, M. Raffel, C. Willert, M. Rosengarten, and J. Kompenhans, "Hybrid stereoscopic particle image velocimetry," *Exp. Fluids*, vol. 23, pp. 331–334, 1997.

[64] E. B. Arik and J. Carr, "Digital particle image velocimetry system for real-time wind tunnel measurements," in *Proceedings of the 1997 17th IEEE International Congress on Instrumentation in Aerospace Simulation Facilities*, (Pacific Grove, USA), October 1997.

[65] A. Cogotti and F. D. Gregorio, "Presentation of flow field investigation by PIV on a full-scale car in the Pininfarina wind tunnel," *SAE Technical Paper Series*, no. 2000-01-0870, 2001.

[66] D. A. Lyn and W. Rodi, "The flapping shear layer formed by flow separation from the forward corner of a square cylinder," *Journal of Fluid Mechanics*, vol. 267, pp. 353–376, 1994.

[67] D. A. Lyn, S. Einav, W. Rodi, and J. H. Park, "A laser-Doppler velocimetry study of the ensemble-averaged characteristics of the turbulent near wake of a square cylinder," *Journal of Fluid Mechanics*, vol. 304, pp. 285–319, 1995.

[68] D. F. G. Durao, M. V. Heitor, and J. C. F. Pereira, "A laser anemometry study of separated flow around a squared obstacle," in *Laser Anemometry in Fluids III (ed. R. J. Adrian, et. al.) LADOAN-IST*, (Lisbon, Portugal), 1986.

[69] A. A. McKillop and F. Durst, "A laser anemometry study of separated flow around a squared cylinder," in *Laser Anemometry in Fluids II (ed. R. J. Adrian, et. al.) LADOAN-IST*, (Lisbon, Portugal), 1986.

[70] H. Oshima and B. R. Ramaprian, "The use of particle image velocimetry to study vortex shedding behind a square cylinder," *Transaction of the ASME: Journal of Fluids Engineering*, vol. 108, pp. 15–20, 1991.

[71] J. Wissink, "Dns of 2d turbulent flow around a square cylinder," *International Journal for Numerical Methods in Fluids*, vol. 25, pp. 51–62, 1997.

[72] www.Ferrari.it, "Ferrari website." Internet.

[73] Y. Chew, S. Luo, and M. Cheng, "Numerical study of a linear shear flow past a rotating cylinder," *Journal of Wind Engineering and Industrial Aerodynamics*, vol. 66, pp. 107–125, 1997.

[74] Teco American Inc., Texas, USA, *7210M Series VFD Installation and Operation Manual.*

Appendix A

Wind Tunnel Fan Performance Curves

This Appendix contains two static pressure and impeller power curves for the AID-143, Tube Axial fan used for the wind tunnel in this study (Enviro-Tech HVAC Products, Ancaster, Ontario). These parameters have been plotted against the volume flowrate, and at various fan blade angles. The final figure shows some overall dimensions of the fan and casing. All performance curves and drawings are included as received from Enviro-Tech HVAC Products (Ancaster, Ontario).

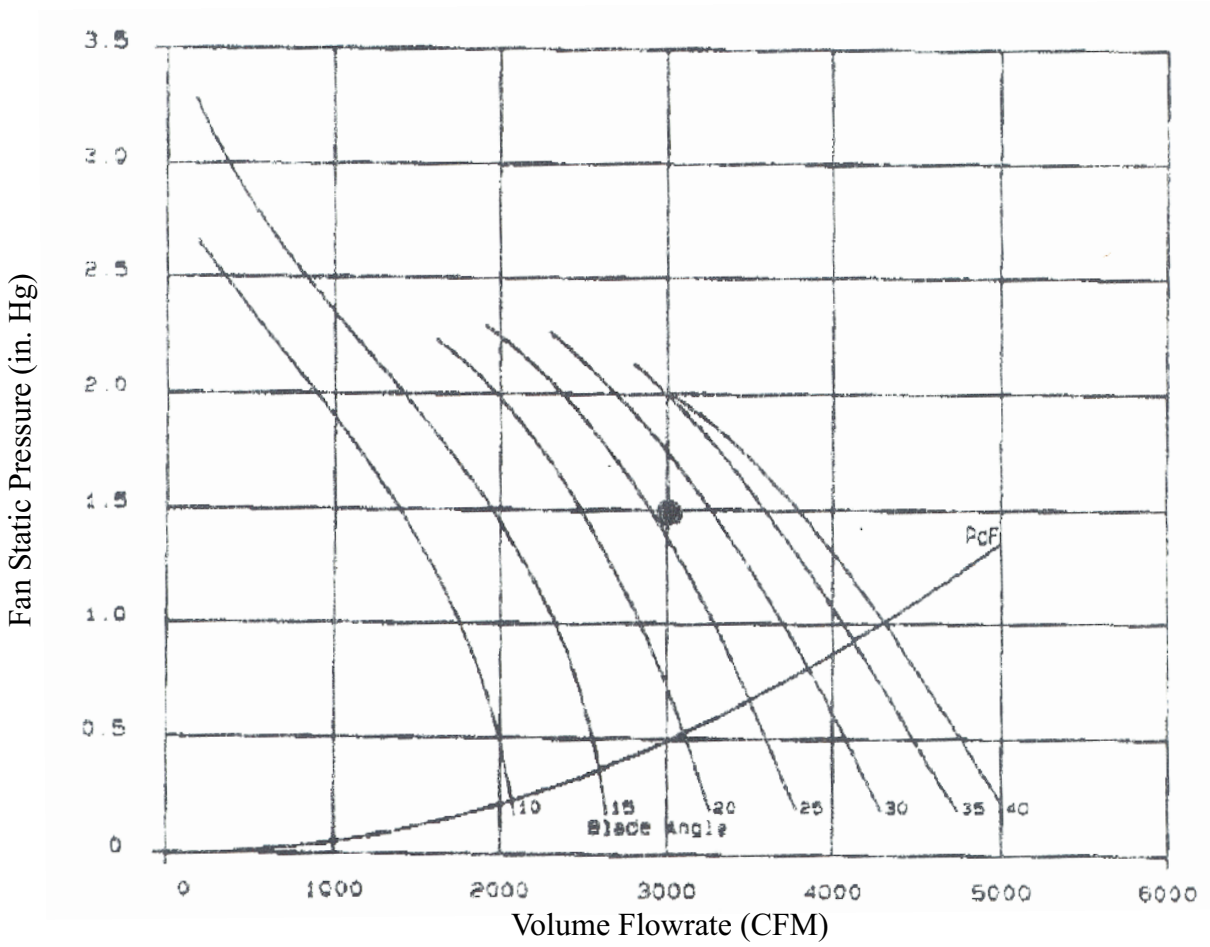

Figure A.1: Fan static pressure curve (at 3450 rpm) for the AID-143, Tube Axial fan as purchased from Enviro-Tech HVAC Products (Ancaster, Ontario): fan static pressure (in inches of mercury) plotted versus the volume flowrate (in cubic feet per minute) Note: fan blade angles given in degrees Celsius

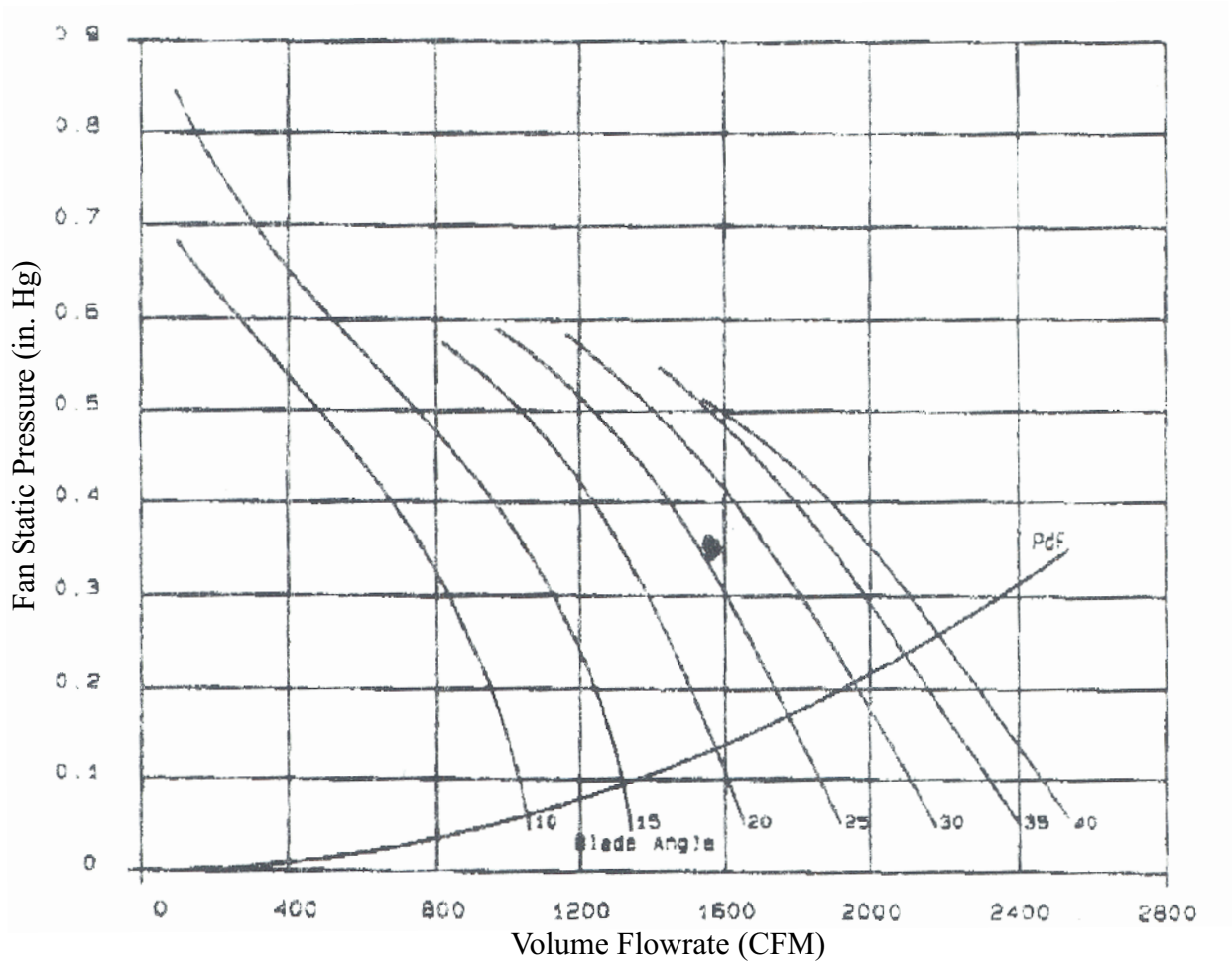

Figure A.2: Fan static pressure curve (at 1750 rpm) for the AID-143, Tube Axial fan as purchased from Enviro-Tech HVAC Products (Ancaster, Ontario): fan static pressure (in inches of mercury) plotted versus the volume flowrate (in cubic feet per minute) Note: fan blade angles given in degrees Celsius

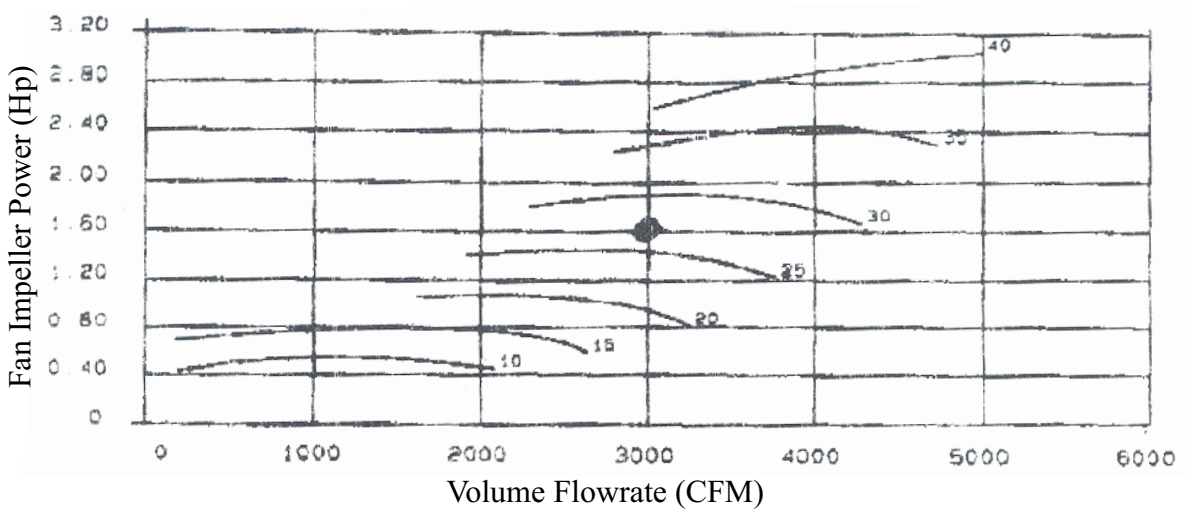

(a)

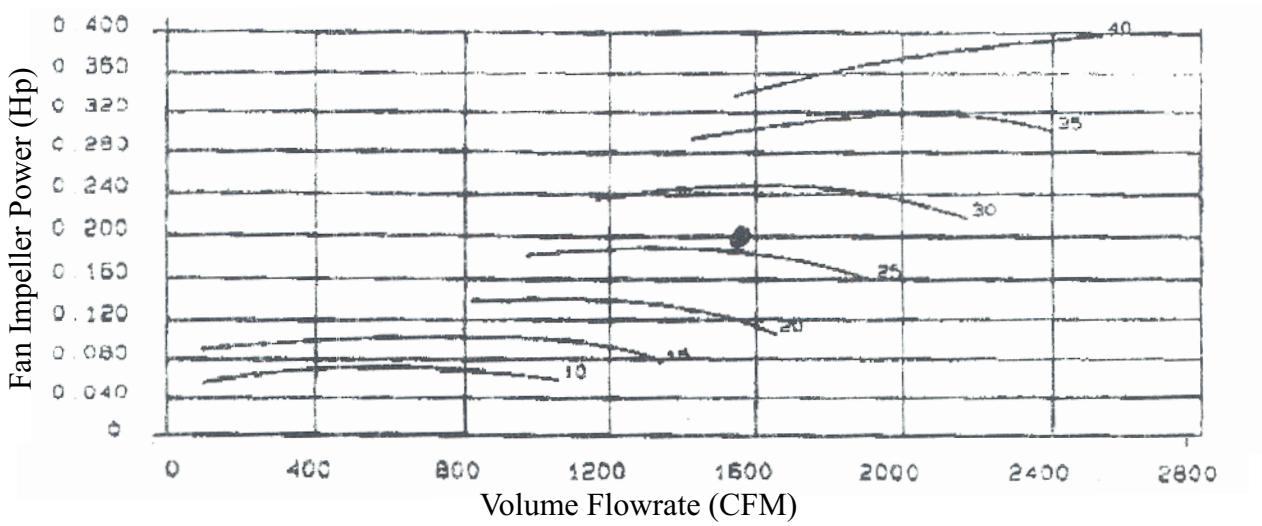

(b)

Figure A.3: Fan power curve for the AID-143, Tube Axial fan as purchased from Enviro-Tech HVAC Products (Ancaster, Ontario): fan impeller power (in Hp) plotted versus the volume flowrate (in cubic feet per minute) Note: fan blade angles given in degrees Celsius, (a) 3450 rpm, (b) 1750 rpm